X-Ray Measurements of Shock-Induced Mixing at an Air/Xenon Interface

Thesis by
Riccardo Bonazza

In Partial Fulfillment for the Degree of
Doctor of Philosophy

California Institute of Technology
Pasadena, California

1992
(Defended March 6 1992)

A Riccardo e Vincenzo
che m'hanno insegnato le cose più belle

Acknowledgments

It is my pleasure to thank my advisor, Prof. Sturtevant, for a strong, demanding guidance throughout the course of this work. What I have learned from him goes far beyond the field of shock-interface interactions. I hope that some of his ability of always seeing and asking the fundamental, critical questions stays with me from now on.

I also thank Dr. Vivien Rupert and Dr. Alan Spero of Lawrence Livermore National Laboratory for sponsoring this research and providing me with many, crucial ideas.

My gratitude also goes to the GALCIT community for the countless times I received help from some of its members, may it be a professor, a student a technician or a secretary. No student here could be successful in his efforts if it weren't for the friendly atmosphere and the habit of sharing one's skills with one another. Among the professors, in particular, my thanks to Paul Dimotakis for many, most enjoyable conversations during which the most difficult things always ended up looking more approachable, for showing me his passion for rigorous science, and most of all, his enthusiasm for teaching. Among the friends, my special gratitude to Jacques Bélanger, Balu Nadiga and Grégoire Winckelmans for being very close in the last, difficult period of my work.

A special mention is for Dr. Martin Brouillette, with whom this project was started many years ago: Thanks for all the help during the many years, but, most importantly, thanks for a beautiful friendship.

My gratitude to uncle Walter and aunt Frances, for years of hospitality, support and laughter.

Finally, I thank my family in Italy for years of encouragement and for never failing to ask me, in any letter or phone call, when would I be done and go back home.

This research was supported by the U.S. Department of Energy, Lawrence Livermore National Laboratory, under project agreement DOE W-7405-ENG-48.

ABSTRACT

A new experimental technique to measure the density of a high atomic number gas at an interface has been developed and demonstrated. It is based on the absorption of X-rays by the high atomic number gas, and it was implemented in a vertical square shock tube for the study of shock-accelerated air/xenon interfaces. These were prepared by retracting a metal plate initially separating the two gases, prior to the release of the shock wave. Thus the interfaces were all of initial finite thickness. Interfaces of two types, quasi-sinusoidal and nominally flat, were examined. Object of study were the amplitude of large wavelength (25 - 100 mm) perturbations on the interface, and the thickness of the interface. An integral definition for the interface mean line (proposed in a previous numerical work at GALCIT) was adopted; a new integral definition for the interface thickness was proposed, making it feasible to study for the first time the thickness of quasi sinusoidal interfaces. Experiments were performed to image interfaces having interacted with the incident shock, the incident and the reflected shock, or a series of weak waves reverberating between the interface and the shock tube end wall. The results for the growth rates of the amplitudes were compared against a model based on the linear theory: The measured values are larger than the predicted ones in the case when the interface only interacts with the incident and the first reflected shocks. They are smaller than the theoretical ones in the case of multiple reverberations. The interface thickness exhibits essentially no growth upon interaction with the incident shock. The interaction of the reflected shock with the turbulent boundary layer behind the incident one generates random acoustical disturbances which reach the interface and cause the subsequent thickness growth. The thickness growth rates of nominally flat interfaces are larger than those previously found at GALCIT in a schlieren visualization experiment, in the case of two shock interactions. They are smaller in the case of multiple interactions. In the case of two shock interactions, wall vortices generated by the interaction of the reflected shock with the boundary layer behind the incident one severely affected the measurements. A correction was proposed to account for this effect in the measurements of the interface thickness. The need remains for a different experimental technique, capable of eliminating these adverse effects altogether.

Table of Contents

LIST OF SYMBOLS

a	Speed of sound
A	Atwood number
b_1, b_2	Coefficients in the linear fit of CCD output voltage *vs.* light intensity
c	Proportionality constant in the expression for the turbulent energy dissipation
d	Optical depth
D	Optical density
E	Exposure of X-ray negative
F	Diffusion coefficient
g	Acceleration
G_{turb}	Turbulent kinetic energy per unit volume
h	Interface thickness
I	X-ray or light intensity
k	Wavenumber
K	Eddy diffusivity
l	Thickness of material traversed by X-rays
L	Width of test section
m	Molecular mass
M	Mach number
n	Growth rate of perturbations
p_0, p_1, p_2	Coefficients in the non linear fit of optical density *vs.* aluminum thickness
P_E	Photon energy
Q	Turbulent kinetic energy per unit area
t	Time
u	Horizontal component of the velocity
v	Vertical component of the velocity
V	CCD camera output voltage
x	Space coordinate along shock tube width
y	Space coordinate along shock tube length
Y	Height of test section window

z	Space coordinate along shock tube side
Z	Atomic number
α	Proportionality constant between eddy size and layer thickness
β	Proportionality constant in the expression for interface thickness growth rate
γ	Ratio of specific heats
Γ	Ratio of modal growth rates for air/SF_6 and air/Xe interfaces
δ	Interface thickness
δ_D	Dirac delta-function
ϵ	Turbulent energy dissipation
ζ	Exponent in modeling of interface thickness in time
η	Perturbation amplitude
λ	Perturbation wavelength
μ	Dynamic viscosity
ν	Kinematic viscosity
ρ	Density
σ	X-ray absorption coefficient
τ	Time elapsed between end of plate retraction and shock arrival at interface
Φ	Velocity potential
χ	Proportionality constant in modeling of interface thickness in time
ψ	Growth reduction factor for interfaces of finite thickness

CHAPTER 1

INTRODUCTION

Instabilities can arise at the interface between different fluids, under a variety of conditions. Examples are: The Rayleigh-Taylor instability, which amplifies the perturbations on an interface between fluids of different densities, accelerated in the direction from the lighter to the heavier; the Richtmyer-Meshkov instability, driven by the interaction of a shock wave with a similar interface, regardless of the direction of propagation of the shock; and the Landau-Darrieus instability, in which a mass flux across an interface destabilizes the interface (Landau & Lifshitz, 1959). Common to these instabilities is the driving mechanism, *viz.* the baroclinic generation of vorticity at the interface. The Kelvin-Helmoltz instability also arises between stratified fluids, as a consequence of relative tangential, rather than normal, motion between the layers. In the case of the Rayleigh-Taylor and the Richtmyer-Meshkov instabilities, viscosity and surface tension reduce the growth of the perturbations, and so do finite density gradients (continuous rather than discontinuous interfaces).

The Rayleigh-Taylor and Richtmyer-Meshkov instabilities occur in nature (the typically cited example is that of supernova explosions, see Arnett *et al.*, 1990) as well as in technological settings. In some applications, the Richtmyer-Meshkov instability can be used advantageously, *e.g.*, in air breathing combustion systems for hypersonic vehicles, where combustion takes place at supersonic velocities and fast mixing is mandatory (see Marble *et al.*, 1987); in other instances its manifestation is deleterious, as in the laser driven implosion of nuclear fuel microtargets in inertial confinement fusion experiments (see Takabe *et al.*, 1988).

The events that take place upon interaction of a shock wave with the interface between two gases of different physical properties can be summarized into two categories: The effects generated on the wave by the interface, *viz.* the refraction and distortion of the shock wave, and the effects induced by the shock on the interface, *viz.* the setting in motion of the interface and the baroclinic generation of vorticity wherever the $\nabla\rho \times \nabla p$ cross product is non zero.

The wave phenomena have been extensively investigated in the past, both theoretically and numerically (see, *e.g.*, Abd-El-Fatah & Henderson 1978a, 1978b, Catherasoo & Sturtevant 1983, Schwendeman 1988). Upon interaction of the incident shock with the interface (Fig. 1.1, t_1), one wave is reflected (of the same sign if the wave travels from the 'soft' into the 'hard' gas, and of the opposite sign in the other case), and one wave of the same sign as the incident one is transmitted through the interface (Fig. 1.1, t_2). In a shock tube experiment, the transmitted wave reaches the end wall, reflects (Fig. 1.1, t_3), and interacts with the moving interface, in the same manner as described for the incident shock (Fig. 1.1, t_4).

In general (unless the interface and the shock wave are perfectly flat and parallel), both the reflected and the refracted waves are distorted. The reflected wave always takes on the same shape of the interface. If the incident wave is traveling from the light into the heavy gas (Fig. 1.2, t_1), the transmitted shock takes on a shape with the same phase of that of the interface (Fig. 1.2, t_2): The distorted shock focuses in the regions where it is concave in the direction of propagation, and defocuses where the concavity is in the opposite direction. Since the shock wave is stable to perturbations on its surface, the distortions induced on the shock tend to flatten out. In a shock tube experiment the transmitted wave reaches the end wall, reflects, and interacts with the interface, this time moving from the heavy into the light gas (Fig. 1.2, t_3, the shock being depicted as flat for simplicity). In this case the transmitted shock has a phase opposite to that of the interface (Fig. 1.2, t_4).

In the present work, the focus is on the fluid mechanics of the motion which develops at the interface. The various phases of the evolution of the interface are sketched in Fig. 1.3. The vorticity deposited on the interface at the time of the interaction with the shock persists there after shock refraction, leading to the distortion of the interface. The evolution of the interface can be described at the early times by linearized equations of motion. At this stage, the perturbations grow in amplitude without changing shape. The growth rate of the perturbations is proportional to their wave number. At late times (*viz.* when the perturbation amplitude is no longer small compared to the wavelength), non-linearities become important causing the shape of the perturbations to distort from the original one, and the growth rates to become smaller than those predicted by the linear theory. The perturbations with large wavenumber are the first ones to grow out of the linear regime.

Small-scale turbulence is generated by the evolution of small-scale, random disturbances: These are in part generated on the interface at the time when it is constructed in the shock tube, and, more importantly, are induced on the interface by the acoustic waves generated by the interaction of the reflected shock wave with the turbulent boundary layer behind the transmitted shock. The macroscopic consequence of the turbulent motions at the interface is the entrainement of the fluids from both sides, and the thickening of the interface. If the interface is initially nominally flat (as sketched in Fig. 1.4), and no large-wavelength perturbations can be observed, this mixing process is actually the only measurable consequence of the original shock-interface interaction. If the interface exhibits both large and small wavelength perturbations (as sketched in Fig. 1.5) both amplitude growth and interface thickening are observed.

This time evolution applies to interfaces with both zero and finite thickness. Since the motions at the interface are due to the cross product of the pressure and density gradients, the perturbations of an interface of finite thickness grow more slowly than those on a discontinuous one.

The wave phenomena are essentially uncoupled from the fluid mechanics as long as the incident shock wave is weak ($M_i \leq 1.5$). For strong shocks, the wave motion influences the fluid motion (through acoustic energy radiation), and compressibility effects become important.

1.1 Previous Contributions

The first, linear theory for the instability of the discontinuous interface between two incompressible fluids under gravitational acceleration was proposed by Lord Rayleigh (1900) for an exponential density profile: He proved that the interface is unstable only if the light fluid accelerates into the heavy one. Taylor (1950) repeated the analysis for a discontinuous interface; the first experiments to verify the theory were performed by Lewis (1950). Richtmyer (1960) studied the linear, inviscid theory for incompressible fluids applied to a shock-accelerated interface, and showed good agreement between predictions made on the basis of that model and the results of a numerical simulation. The first experiments in which a shock wave accelerated a discontinuous interface were carried out by Meshkov (1969); more recent work is *e.g.*, that of Benjamin & Fritz (1987), and Remington *et al.* (1991).

The baroclinic generation of vorticity on the interface also causes the development of turbulence, which leads, in turn, to the mixing between the two fluids and the thickening of the interface. Experiments to study the growth rate of the thickness of initially discontinuous interfaces have been reported by Read (1984) and Andronov *et al.* (1976); Mikaelian has modeled a continuous density profile across the interface as a superposition of uniform density slabs, and obtained growth rates for the thickness of both continuously and impulsively accelerated interfaces. The turbulent energy created at the interface was obtained by Saffman & Meiron (1989), and Mikaelian (1991a).

Shock tube experiments have been carried out at GALCIT (Brouillette, 1989) to focus the attention on some of the issues involved: Growth rate dependence on Atwood and Mach numbers; effects of the initial interface shape and thickness; role played by the microfilm membranes used to prepare discontinuous interfaces; importance of the wall effects.

1.2 Goals of the Present Investigation

The present work is a continuation of the previous experimental effort, carried out in the GALCIT vertical, square shock tube; the investigation is initiated with the idea of using an unusual flow-visualization technique, based on X-ray absorption by the heavy gas at the interface (xenon), upon which to implement a quantitative densitometry procedure. The objective is to reconstruct the density field across the interface, and from it deduce the interface properties most normally studied: Its distortion and thickness.

The project has been successful in that quantitative densitometry is accomplished and useful data is extracted from the X-ray negatives: This is achieved by digitization of the X-ray negatives with a CCD camera and a frame grabber, and by a specially developed calibration procedure that links the grey levels on each negative to the density of the xenon. In particular an integral definition of mean interface shape (first proposed by Pham, 1990) is employed and an integral definition of interface thickness (modification of a model proposed by the same author) is introduced. The interface shape is decomposed into its Fourier components, and their time evolution studied individually.

Some schlieren visualization experiments are performed both on air/xenon and air/SF_6 interfaces, to allow for a comparison between the two different imaging techniques. All experiments are performed using interfaces of initial finite thickness, with pseudo-single

scale and multiscale perturbations imposed on them; the Mach number of the accelerating waves is either $M_i = 1.32$ or $M_i = 1.52$. The interface is studied upon interaction with the incident shock, the reflected shock, and a series of wave reverberations.

1.3 Outline

Some of the linear theory for the Rayleigh-Taylor and Richtmyer-Meshkov instability is reviewed in Chapter 2, together with more recent attempts at modeling the effects of weak non-linearities. The results of previous theoretical and experimental work investigating the time evolution of the interface thickness are also presented.

Chapter 3 describes the experimental apparatus; Chapter 4 discusses the image analysis procedures that leads from the X-ray negatives to the xenon density fields, and the data reduction developed to obtain the desired interface properties.

Chapter 5 presents the results for single scale and multiscale interfaces accelerated by one or two shock waves. For these experiments, the initial interface position is out of the test section. The modal growth rates are smaller than what Brouillette (1989) had found for the whole interface (without modal decomposition). The interface thickness is measured for both types of interface, and the growth rate for the single scale is larger than for the multiscale interface. Wall effects are more evident than in Brouillette's photographs, and an explanation of their effect on X-ray absorption is given, possibly laying the ground for a correction of the present results.

In Chapter 6 the results of the observations of interfaces upon interaction with several reverberations are presented. For these experiments, the interface is initially located inside the test section. Single and multiscale interfaces are accelerated with shock waves of two different Mach numbers. It is found that modal growth rates change substantially with the Mach number, whereas thickness growth rates do not. The thickness growth rate is again larger for the single scale than for the multiscale interfaces. The wall effects are much smaller than those observed in Chapter 5, because the interface travels a smaller distance before being imaged.

Concluding remarks are made in Chapter 7.

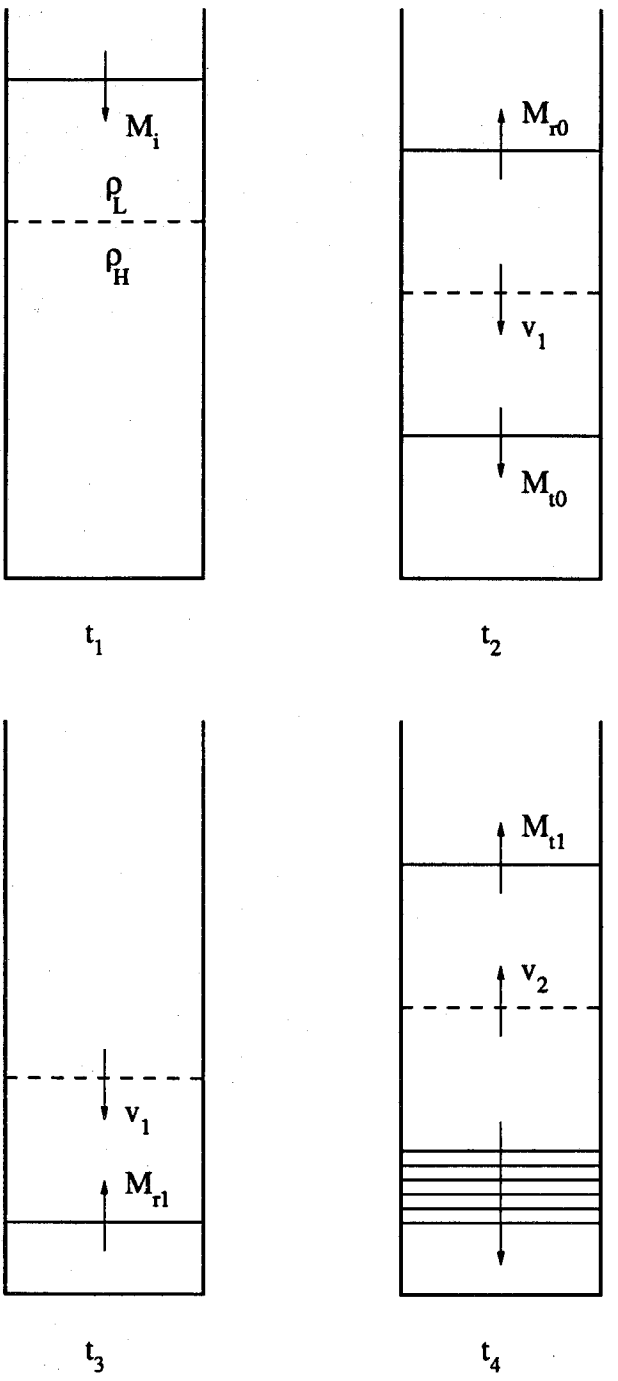

Fig.1.1 Shock Refraction at a Density Interface. System of Transmitted and Reflected Waves.

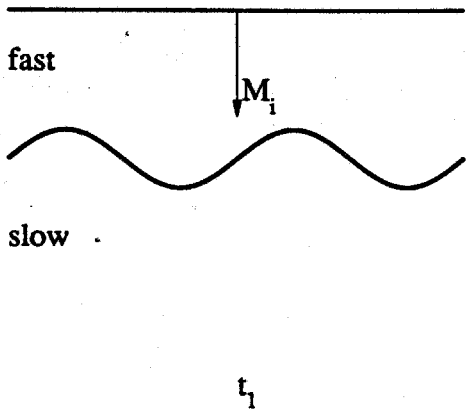

t_1

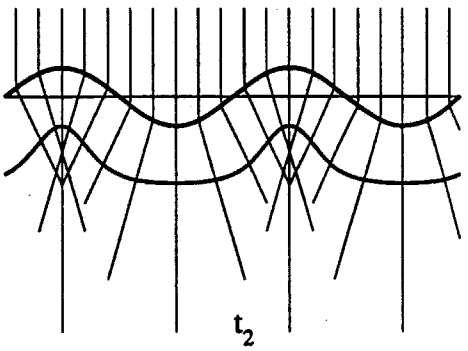

t_2

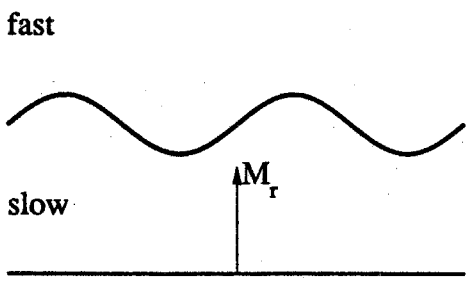

t_3

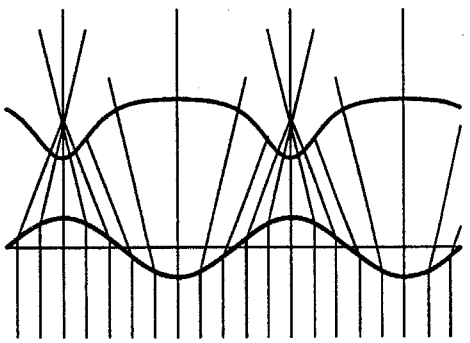

t_4

Fig.1.2 Shock Refraction at a Density Interface. Wave Distortion.

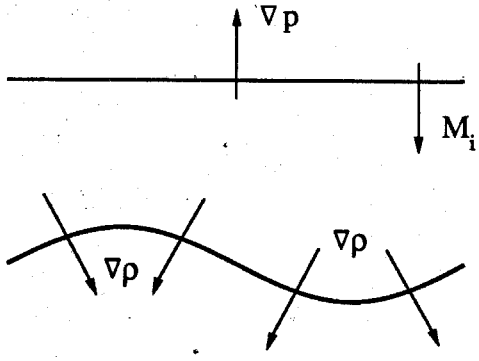

Incident Shock

Vorticity Generation

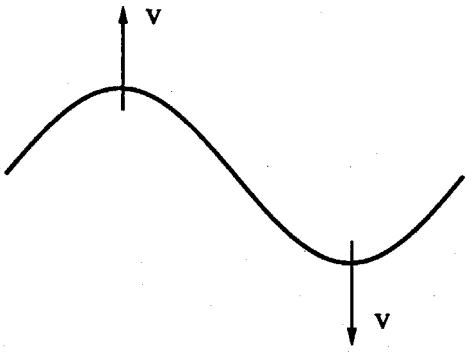

Linear Growth

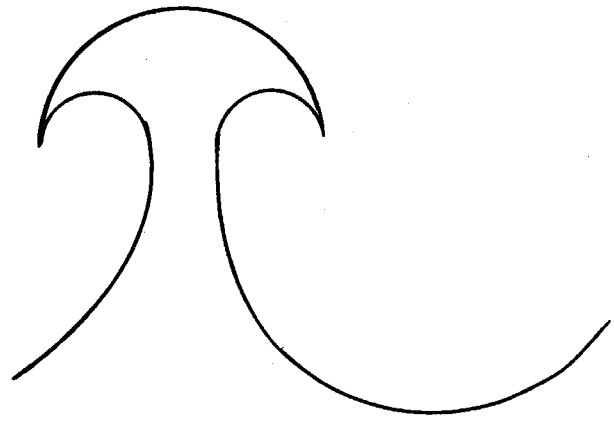

Nonlinear Effects

Fig.1.3 Various Stages of the Interface Evolution.

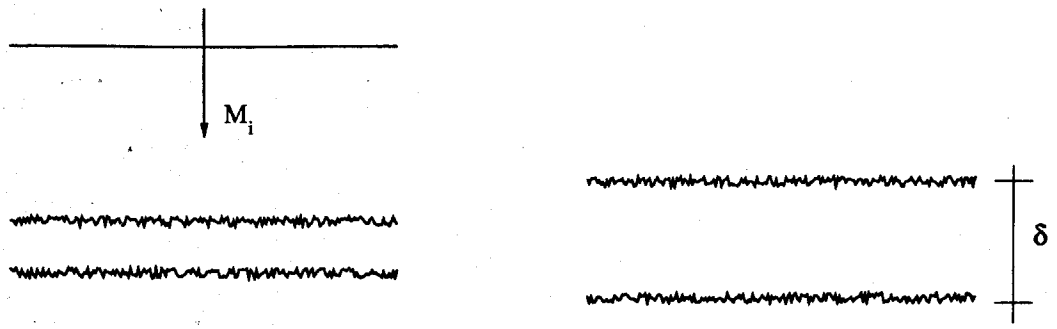

Fig.1.4 Nominally Flat Interface with Small Wavelength Perturbations.

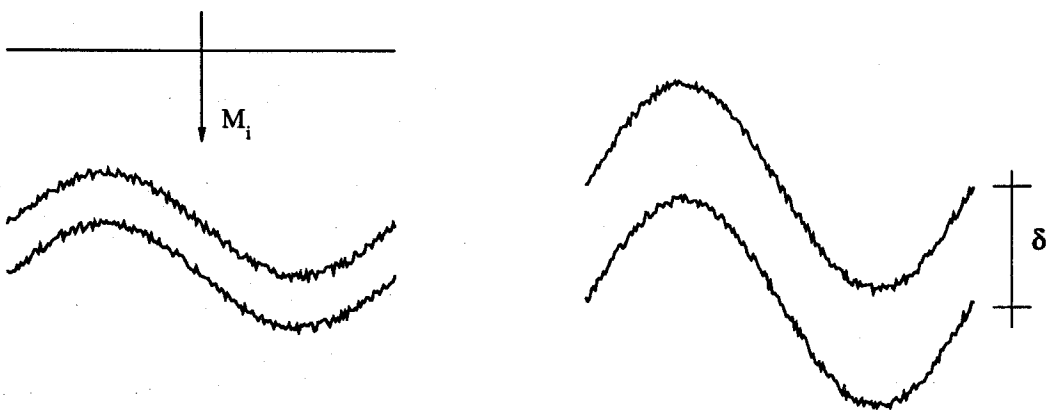

Fig.1.5 Interface with both Large and Small Wavelength Perturbations.

CHAPTER 2

PREVIOUS THEORETICAL AND EXPERIMENTAL WORK

2.1 Introduction

This chapter presents the theory for the case of a discontinuous interface under constant acceleration, the theory for the shock-accelerated discontinuous interface (developed as an extension of the previous one), the corrections for the case of an interface of finite thickness, and a model proposed by Brouillette (1989) for the evolution of an interface under multiple reverberations. An attempt will be made in Ch. 5 and Ch. 6 to compare the results generated from the present experiments with the existing theory.

2.2 Rayleigh-Taylor Instability

The time-evolution of the interface between two fluids of different densities, featuring two-dimensional perturbations and subjected to a constant acceleration g in a direction perpendicular to itself (see Fig. 2.2.1), was first studied by Lord Rayleigh (1900) and Taylor (1950). The two fluids have density ρ_1 and ρ_2 respectively; the thickness of the interface is taken to be zero, and the perturbations to be of a single spatial frequency of wavenumber k and wavelength λ, so that, at any time t, the interface can be described by

$$y = \eta(t) \cos kx \ . \tag{2.2.1}$$

where η is the amplitude of the perturbations. The analysis is based on the assumption of small perturbations,

$$\eta << \lambda \ : \tag{2.2.2}$$

Under this condition the equations of motion can be linearized. Furthermore, the flow is taken to be incompressible and the fluids inviscid. The problem can then be described in terms of two velocity potentials, one in each fluid, Φ_1 and Φ_2 subject to the boundary conditions that velocities be bounded at large $|y|$, and that velocity and pressure be continuous at the interface. The potentials take on the form

$$\Phi_1 = \frac{n\eta_0}{k} e^{-ky} \sinh nt \ \cos kx \tag{2.2.3}$$

and

$$\Phi_2 = -\frac{n\eta_0}{k} e^{ky} \sinh nt \cos kx \tag{2.2.4}$$

where

$$n = \sqrt{kgA}, \tag{2.2.5}$$

is the growth rate of the perturbation, and A is the Atwood number for the fluid combination, defined as

$$A = \frac{(\rho_2 - \rho_1)}{(\rho_2 + \rho_1)} . \tag{2.2.6}$$

The amplitude of the perturbations is governed in time by the differential equation

$$\frac{\partial^2 \eta}{\partial t^2} = kgA\eta . \tag{2.2.7}$$

If $A < 0$ the solution to the differential equation is an exponential function with imaginary exponent

$$\eta(t) = \eta_0 e^{i\sqrt{kgA}t} : \tag{2.2.8}$$

the amplitude of the perturbations oscillates between two finite limits, and the interface is termed 'stable'. When $A > 0$ the solution is a real exponential

$$\eta(t) = \eta_0 e^{\sqrt{kgA}t} \tag{2.2.9}$$

and the amplitude grows unboundedly. Thus the interface is 'unstable' and the process is called the Rayleigh-Taylor instability. The first experiments to check the validity of Taylor's theory were performed by Lewis (1950) with air-liquid interfaces. Jacobs and Catton (1988) developed a third order theory that predicted the generation of higher harmonics once the instability had entered its nonlinear stage. Haan (1989, 1990) has recently developed a second order, inviscid analysis including surface tension. Because of surface tension (T), there exists a most unstable mode, of wavelength k_p (see Chandrasekhar, 1961), given by

$$k_p = \sqrt{\frac{1}{3}\frac{g(\rho_2 - \rho_1)}{T}} .$$

Haan shows that, for an interface with a superposition of perturbations of different wavelengths, there exists a weakly nonlinear phase (starting when the modes near k_p reach an amplitude of about $1/Lk_p^2$) during which constructive mode coupling drives the amplitude of long wavelength perturbations ($k < k_p$) to larger growths than would result from the linear theory. Here L is the size of the system (*e.g.* the side of the test section). The initial

amplitudes of these large wavelength modes are irrelevant to the amplitudes they reach during the weakly nonlinear phase, since these are entirely determined by the mode coupling with the modes near k_p. The process becomes fully nonlinear when the peak amplitude approaches the value $1/Lk^2$. But Haan also points out that, in the limit of the acceleration going to 0 (which is the Richtmyer-Meshkov case, after the impulsive acceleration has acted), the equations do not suggest that mode coupling will dominate the initial modes in the same way it does for the Rayleigh-Taylor case.

The case of interfaces of finite thickness, here indicated with δ, was first examined by LeLevier *et al.* (1955) and Duff *et al.* (1962). Figure 2.2.2 shows the geometry studied by these authors. The interface has a sinusoidal distortion of wavenumber k coupled with a finite density gradient across it: $\rho = \rho(y)$ is not a step function but an arbitrary, continuous one. Following Chandrasekhar (1961, p. 433), the perturbations on a thick interface can be shown to follow the same time dependence of Eq. 2.2.9 with the eigenvalue equation for the growth rate, which we call n_t, given by

$$\frac{\mathrm{d}}{\mathrm{d}y}\left(\rho\frac{\mathrm{d}v}{\mathrm{d}y}\right) = vk^2\left(\rho - \frac{g}{{n_t}^2}\frac{\mathrm{d}\rho}{\mathrm{d}y}\right) \tag{2.2.10}$$

Since the growth rate of an interface of finite thickness is smaller than that for a discontinuous interface (because the density gradient is finite rather than infinite) Duff proposed for n_t the expression

$$n_t = \sqrt{\frac{kgA}{\psi}}\,, \tag{2.2.11}$$

with ψ being a growth reduction factor ($\psi > 1$). By using this expression in Eq. 2.2.10 one gets

$$\frac{\mathrm{d}}{\mathrm{d}y}\left(\rho\frac{\mathrm{d}v}{\mathrm{d}y}\right) = vk^2\left(\rho - \frac{\psi}{Ak}\frac{\mathrm{d}\rho}{\mathrm{d}y}\right)\,. \tag{2.2.12}$$

This is an eigenvalue equation for ψ. It can be integrated analytically for an exponential density profile (Mikaelian, 1989a), or numerically for an arbitrary one. From Eq. 2.2.11 it is clear that ψ is a growth reduction factor: For the discontinuous interface

$$\psi \to 1\,, \quad n_t \to n\,, \tag{2.2.13}$$

so the growth rate is the same as in Eq. 2.2.5. For a finite density gradient

$$\psi = \psi(A, \delta/\lambda)\,. \tag{2.2.14}$$

Duff *et al.* computed the eigenvalue of Eq. 2.2.10 for a diffusive density profile (following a complimentary error function law). Figure 2.2.3 shows the behavior of ψ *vs.* δ/λ, parametrized by the Atwood number. It was obtained numerically by Brouillette (1989) for a density profile following the same law of that investigated by Duff *et al.* ψ increases with δ/λ and decreases with the Atwood ratio. Mikaelian (1982) modeled density profiles of arbitrary shape as superpositions of N layers of fluid of constant density, obtaining the growth rates from the eigenvalues of an $(N-1) \times (N-1)$ matrix. The growth rates he obtained were smaller than those given by the classical theory for a discontinuous interface with the same overall Atwood number of the stratification. He also found that, in general, the growth rate of one interface is influenced by the presence of the others, but if the wavelength of the perturbations is much smaller than the thicknesses of two adjacent layers ($\lambda << \delta_i, \delta_{i+1}$, at the ith interface) then that interface decouples from the others and its growth rate reduces to the classical one. On the other hand for $\lambda >> \delta_i$ for all i, an interface of N layers behaves very closely to a discontinuous interface with an equivalent Atwood number given by

$$A_s = \frac{\rho_N - \rho_1}{\rho_N + \rho_1 + 2\sum_{i=2}^{N-1} \rho_i \tanh(\pi\delta_i/\lambda)} . \qquad (2.2.15)$$

In the case of a 3-slab stratification, for a fixed overall density jump, the largest reduction of the growth rate of the most unstable mode is achieved by making the density of the middle layer equal to the geometric mean of the other two. A comparison with the exact analytical results for an exponential density profile showed that the number of layers necessary to get the desired agreement depended on the wavelength of the perturbation being simulated. Since the matrix inversion becomes computationally intensive for large N (≈ 200), Mikaelian also proposed (1986) a set of moment equations to obtain approximate analytical solutions for different density profiles. The agreement with the results of a calculation for a 52-layer interface degraded as the wavenumber increased.

2.3 Richtmyer-Meshkov Instability

Markstein (1957) was the first to investigate the interaction of a shock wave with a density interface (represented by a flame front). His result was the same as Taylor's result for an interface under constant acceleration. Richtmyer (1960) studied the case of

a discontinuous interface with single-wavelength perturbations, impulsively accelerated by a shock wave (see Fig. 2.2.1). Richtmyer's assumption was that the shock be weak enough so that the flow behind it could be considered incompressible. The acceleration term g in Eq. 2.2.7 is replaced by an impulsive one

$$g \rightarrow [v]\delta_D(t), \tag{2.3.1}$$

where $\delta_D(t)$ is the Dirac delta function and $[v]$ is the velocity jump induced on the interface by the shock wave. Eq. 2.2.7 can thus be integrated once with respect to time to yield

$$\frac{\partial \eta}{\partial t} = k[v]A\eta_0 \tag{2.3.2}$$

where η_0 is the initial amplitude of the perturbations. (Actually, Richtmyer pointed out that, for this equation to hold, enough time must have elapsed for the pressure signals to have traveled, at a finite speed of sound, from the shock fronts to the interface; after these signals have reached the interface, the effects of the focusing and defocusing of the shocks begin to be felt, and Eq. 2.3.2 becomes valid.) The solution of this equation is always linear in t, irrespective of the sign of A. This means that all interfaces are algebraically unstable under impulsive acceleration. The amplitude of the perturbations on interfaces with $A < 0$ initially decreases in time, leading to a flattening of the interface, a reversal of the sign of the perturbations, and a subsequent unbounded growth. For $A > 0$ the amplitude of the perturbations starts to grow immediately after the passage of the shock wave. In both cases the growth is called the Richtmyer-Meshkov instability. Richtmyer showed that use of the post shock values, A' and η_0', in Eq. 2.3.2 gives growth rates within 5% of his numerical calculations. The first experiments to study a discontinuous interface (prepared using a microfilm membrane to separate two gases) under shock-acceleration were performed by Meshkov (1969), and Andronov *et al.* (1976).

Mikaelian (1985, 1990b) studied the interface of finite thickness under shock acceleration with the same two approaches he used for the constant acceleration case. Another approach (as *e.g.* in Brouillette, 1989) is to combine Duff's and Richtmyer's proposals. A growth reduction factor, ψ, is introduced and the constant acceleration is replaced by the impulsive one, $g \rightarrow [v]\delta_D(t)$, so that the differential equation for the amplitude of the perturbations becomes

$$\frac{\mathrm{d}^2\eta(t)}{\mathrm{d}t^2} = \frac{k[v]A}{\psi}\delta_D(t)\eta(t)\,. \tag{2.3.3}$$

Again, the equation can be integrated once yielding, to first order,

$$\frac{\mathrm{d}\eta}{\mathrm{d}t} = \frac{k[v]A'}{\psi}\eta_0' , \tag{2.3.4}$$

whose solution is of the same type as that of Eq. 2.3.2. Brouillette (1989) proposed that

$$\psi = \psi(A', \frac{\delta + \delta'}{2}\frac{k}{2\pi}) , \tag{2.3.5}$$

where the primes indicate post-shock values, to take into account the reduction of the interface thickness due to the incident shock. The growth reduction factor can still be evaluated as the eigenvalue of Eq. 2.2.12. The results of the calculations of ψ used in the present work are shown in Fig. 2.2.3. It is important to observe that, because of the Dirac delta function in the expression for the acceleration, the value of ψ in the expression for the growth rate of the perturbations (Eq. 2.3.4) is fixed at its initial post-shock value. The fact that the interface thickness may be increasing in time, making $\psi = \psi(t)$, does not affect the value one expects for $\mathrm{d}\eta/\mathrm{d}t$.

For an interface of finite thickness interacting with a series of incident and reflected shocks and expansions, Brouillette (1989) proposed to linearly superpose the effects of each shock wave, taking for the initial condition of one shock the Atwood number, amplitude and thickness generated by all previous interactions, so that, after $N + 1$ interactions, the amplitude is governed in time by

$$\left(\frac{\mathrm{d}\eta}{\mathrm{d}t}\right)_N = k \sum_{i=0}^{N} \frac{[v]_i A_i' \eta_i'}{\psi_i} \tag{2.3.6}$$

where $[v]_i$ is the velocity jump induced on the interface by the ith wave ($i = 0$ corresponding to the incident wave, $i = 1$ to the first reflected wave and so on), A_i' and η_i' are the Atwood ratio and the amplitude of the perturbations after the passage of the ith wave, and ψ_i is the growth reduction factor evaluated from A_i' and δ_i'.

2.4 Interface Thickness

Besides the amplitude of the perturbations (whose growth is the manifestation of either the Rayleigh-Taylor or the Richtmyer-Meshkov instability) the other important interface property is its thickness δ; its importance comes from the fact that it is determined by the turbulent mixing processes induced by the Rayleigh-Taylor or Richtmyer-Meshkov instability. Most of the analytical and numerical work developed so far has concerned nominally

flat interfaces, of both zero and finite initial thickness, since these are the ones of interest in practical technological application (*e.g.* inertial fusion confinement experiments). Perturbations on these interfaces are of the random, small-scale type, and grow very rapidly out of the linear regime. It is thought that merging of these small-scale fluctuations results in the formation of large-scale ones (*e.g.*, see Mikaelian, 1988). The interface evolves into a turbulent mixing layer, whose evolution in time is strongly dependent on the available turbulent kinetic energy, which is a fraction of the total kinetic energy of the interface. In the Rayleigh-Taylor case, energy is continuously supplied at the interface by the acceleration; in the Richtmyer-Meshkov case energy is deposited at the interface only by the interaction with the shock wave. In both cases, viscosity tends to dissipate the turbulent kinetic energy into heat.

2.4.1 Rayleigh-Taylor Induced Mixing

Youngs (1984, 1989) has modeled the turbulent mixing at an interface between incompressible, immiscible fluids subjected to an acceleration g, and tuned the model constants to fit the experimental data of Read (1984) and Read & Youngs (1983). The model is based on a system of two-phase flow equations which represent the effects of differential acceleration induced by the pressure gradient on fluid fragments of different densities; drag between fluid filaments, proportional to the square of the velocity difference; transport of mass and momentum by turbulent diffusion. No molecular diffusion is taken into account. The main result is that, after the perturbations have grown out of the linear regime, memory of the initial conditions is lost, and the only length scale of importance is gt^2, and the interface thickness grows like

$$\delta = \beta A g t^2 . \tag{2.4.1}$$

The value of β as measured in the experiments is in the range $0.126 - 0.154$, while that extracted from direct numerical simulations (Youngs, 1984 and 1989) falls between 0.08 and 0.10. Mikaelian (1989b) has applied the Canuto-Goldman (Canuto *et al.*, 1987) analytical model to the turbulence generated by instabilities having a growth rate proportional to a power of the wavenumber of the disturbances. The method allows for the evaluation of the turbulent kinetic energy and its spectrum. For $n = 1/2$ (Rayleigh-Taylor case), assuming a linear density profile across the interface, and using the experimental results of Read (see Eq. 2.4.1), he concluded that the size of the largest eddy in the layer is at any time 40% of

the layer thickness. He also showed that the size of the largest eddy is about 10 times that of the smallest and interpreted this fact as evidence of 'chunk mixing', presumably referring to mixing of large scale, organized structures.

2.4.2 Richtmyer-Meshkov Induced Mixing

Neglecting turbulence, and assuming independence of initial conditions, dimensional analysis shows that a relation of the type

$$\delta = f(A')[v]t \tag{2.4.2}$$

must be satisfied. This result is similar to that of Eq. 2.4.1 with the length scale gt^2 replaced by $[v]t$, due to the impulsive acceleration. To take turbulence into account, Barenblatt (1983) has modeled an infinitely thin instantaneous source of vorticity at the interface between two fluids of the same density. The model relies on the Kolmogorov similarity hypothesis which takes the eddy diffusivity, K, and turbulent energy dissipation, ϵ, coefficients to be dependent only on the eddy size and the mean eddy energy G_{turb}; the eddy size in turn is proportional to the external turbulent length scale, a fraction α of the layer thickness, δ in the present case. Then, by dimensional analysis,

$$K = \delta\sqrt{G_{turb}} \quad \text{and} \quad \epsilon = \frac{cG_{turb}^{3/2}}{\delta} \tag{2.4.3}$$

c being a constant. These expressions can be used in a diffusion equation for the balance of the turbulent energy:

$$\frac{\partial G_{turb}}{\partial t} = \frac{\partial}{\partial y}\left(\alpha\delta(t)\sqrt{G_{turb}}\frac{\partial G_{turb}}{\partial y}\right) - \frac{cG_{turb}^{3/2}}{\alpha\delta(t)}\,. \tag{2.4.4}$$

In the case of no dissipation ($\epsilon = 0$) the quantity

$$Q = \int_0^{\delta(t)} G_{turb}dy$$

is constant in time and the thickness of the turbulent layer follows a

$$\delta \propto t^{2/3} \tag{2.4.5}$$

behavior. If dissipation is non-zero, the behavior is similar

$$\delta \propto t^{\zeta} \tag{2.4.6}$$

with $\zeta < 2/3$. Although the exponents of both of these two laws depend on the model chosen for the terms in the energy equation, the result is important because it provides a scaling formulation of the problem.

Zaitsev *et al.* (1985), Aleshin *et al.* (1988) and Gamalii *et al.* (1989) performed experiments on initially discontinuous and continuous interfaces and measured linear growth rates of the thickness of singly shocked interfaces. Mikaelian (1989b) proposed to use Youngs' results (Eq. 2.4.1) as a departure point to write an expression for the growth rate of the thickness of a shock-accelerated interface: By differentiating Eq. 2.4.1 twice with respect to time, replacing g by $[v]\delta_D(t)$, and integrating twice in time, he obtains

$$\delta = 0.28[v]A't\,. \tag{2.4.7}$$

In the same study he shows that it is not possible to get a scale for the eddy size, and that the largest eddy is at most 1.6 times the smallest. This last observation suggested that the Richtmyer-Meshkov instability induces 'atomic mixing', presumably referring to the absence of large coherent structures in the flow. Brouillette (1989) performed extensive experiments on both discontinuous and continuous interfaces, subject to one, two or multiple wave interactions. The growth rates he obtained showed that Eq. 2.4.7 is largely inadequate, as the measured values are much smaller than the predicted ones.

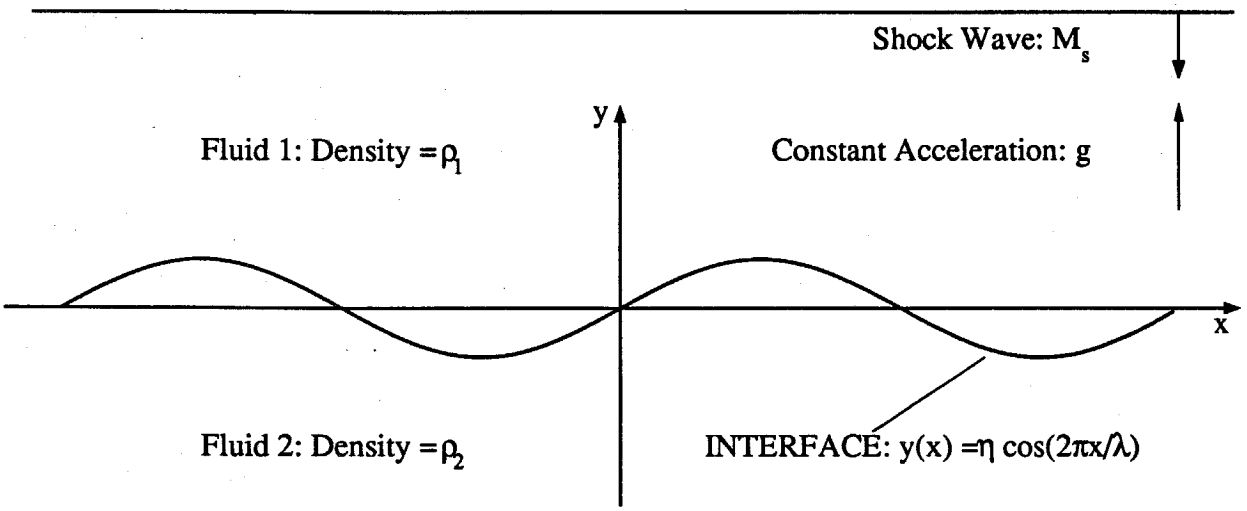

Fig.2.2.1 Discontinuous Interface. Constant Acceleration: Rayleigh-Taylor Instability. Impulsive Acceleration: Richtmyer-Meshkov Instability.

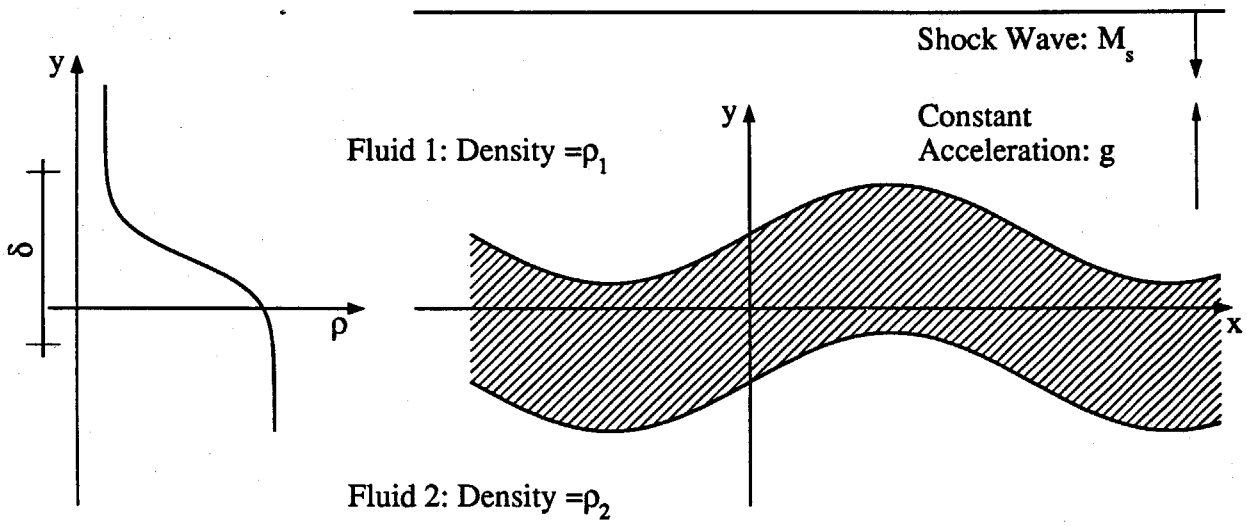

Fig.2.2.2 Continuous Interface.

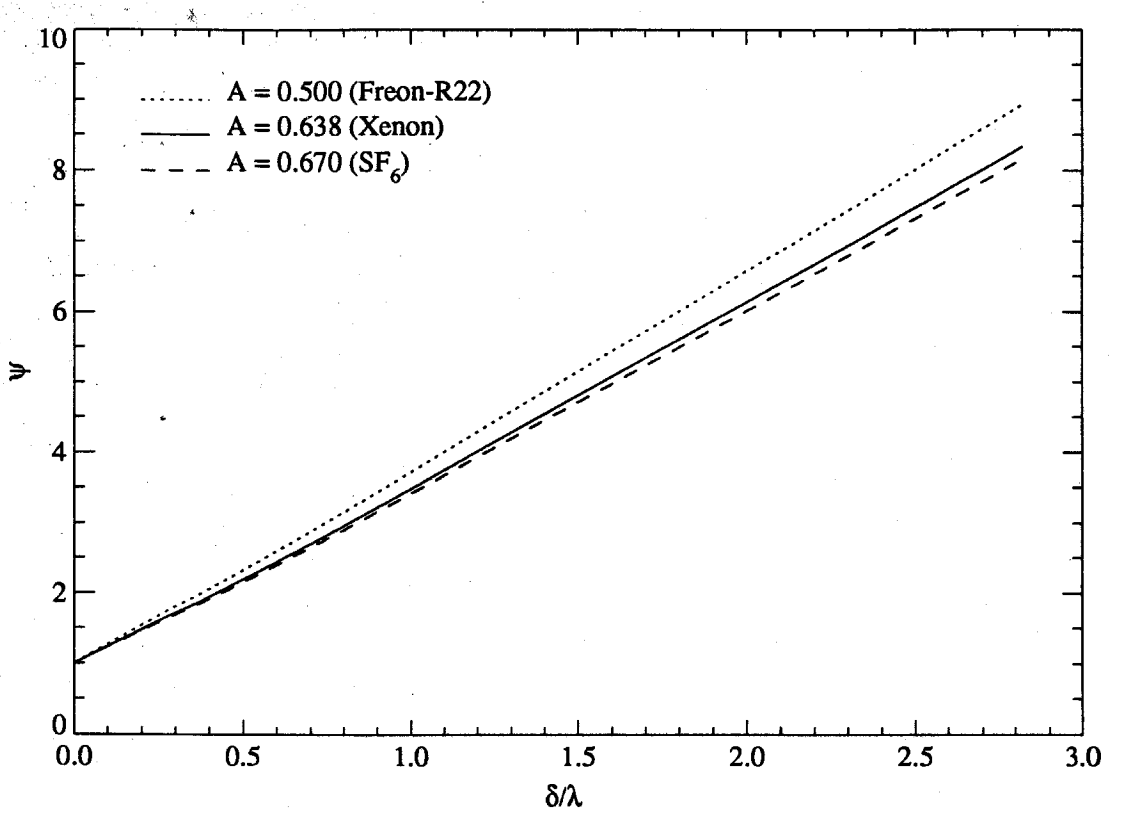

Fig.2.2.3 Growth Reduction Factor, ψ, for Complimentary Error Function Density Profile. Numerical results after Brouillette (1989).

CHAPTER 3

EXPERIMENTAL APPARATUS

3.1 Introduction

The experiments are performed in a vertical, square shock tube designed and fabricated especially for the study of the Richtmyer-Meshkov instability. The tube is vertical to make use of gravity to separate two fluids of different density, at the bottom of the tube, in preparing a continuous interface. The cross section is square to provide the parallel walls necessary for any imaging technique to be used in the study of the flow: in conventional, round shock tubes this necessity is met by the use of 'cookie-cutters' which are usually structurally weaker than the rest of the tube and therefore limit the maximum Mach number at which the facilities can be operated. The present experiments consist of launching a shock wave from the top of the shock tube toward the bottom where a gas interface has been prepared, and imaging the interface either with X-rays or with the schlieren method. In both cases one image of the interface is captured during each run. The tube is operated in two different configurations; a close end wall configuration, for which the interface is located 11 cm from the bottom of the tube, and a far end wall configuration, for which the interface is 71 cm above the end wall. In the rest of this work the two configurations will be referred to as FEW and CEW, respectively. A schematic of the shock tube is presented in Fig. 3.1.1.

3.2 Shock Tube

3.2.1 Driver Section

The shock tube is described by Brouillette (1989). For convenience we include a similar description here.

The driver section is round, with an inside diameter of 16.5 cm. It is 1.83 m long and the wall is 1.27 cm thick. It consists of stainless steel, seamless tubing. Its upper end is closed by an end plate to which the inlet lines, vacuum lines and gauge lines are connected by flexible hoses. The upper half of an assembly into which the diaphragm is clamped, called the diaphragm section (described below), is connected to the lower end of the driver section. The driver and upper diaphragm section (of about 280 kg in total weight) can be lifted vertically by a single person (to access the diaphragm) by a system of pulleys and counterweights. A boost tank (2.3 l in volume), which can be pressurized to up to 81 atm, is connected to the driver section through a high-flow-rate solenoid valve (Skinner #R2HLB21252; with flow rate capability of 0.76 gal/min of 60°F water under a pressure difference of 1 psi) to control the time of the shock release (as described in Sec. 3.7 below).

3.2.2 Diaphragm Section

The diaphragm section connects the driver to the driven section, holds the diaphragm in place, provides the seal necessary to pressurize the driver section, and ensures that the diaphragm ruptures in a repeatable way. The upper half of the diaphragm section has a round cross section. The lower half has a square cross section and connects to the driven section. The concept of the diaphragm section is the same as for that of the 6" GALCIT shock tube, described in Smith *et al.* (1967), and it is illustrated in Fig. 3.2.1. A hydraulic piston squeezes the diaphragm between two stainless steel flanges with mating chevron grooves which prevent the diaphragm from sliding when the driver is pressurized. A hydraulic load of 460 kN is applied on the piston by pressurizing hydraulic fluid with an air driven pump. Just below the diaphragm are a set of knife blades (like those described in Roshko & Baganoff, 1961). They cut the diaphragm as it deforms under the pressure of the driver gas, and therefore guarantee a repeatable rupture mode. All diaphragms are made of 6061Al. The thickness is 0.152 mm or 0.254 mm to produce M =1.3 and M =1.5 shock waves, respectively.

3.2.3 Driven Section

The driven section is 11.4 cm square 4140 cold-drawn steel tubing, with 19 mm wall thickness. The inside corners have radius of curvature 2.5 cm. To remove the scale produced

during drawing, the tube was honed with a silica extrusion process; all parts were then nickel plated. Some furrows, about 15 mm in width and 0.4 mm in depth, aligned with the drawing direction, and present on all the inner sides of the tube, and some randomly distributed hollows of depth about 0.08 mm remained after honing. Other imperfections inside the tube are found at the joining of two successive sections (or two successive segments of the driven section), and at the location of the mechanism for the retraction of a metal plate in the preparation of an interface (see Sec. 3.3) The main effect of these surface imperfections is the generation of transverse acoustic waves, that start radiating upon the passage of a shock in front of them, as was documented by Brouillette (1989). If the imperfection extends transversely across the whole span of the tube side, the passage of a plane shock generates a cylindrical acoustic wave, extending over the same distance. At more localized imperfections, the sonic disturbances generated are probably three-dimensional. Because of the wall roughness, and of the high Reynolds numbers of the flow ($Re \approx 10^6$ for an air speed of 100m/s and a length scale of 10 cm), the boundary layers that develop behind the shock wave are taken to be fully turbulent. This is substantiated by the structures observed on the windows in schlieren experiments which are interpreted to be longitudinal or hairpin vortices in the boundary layer.

The driven section is composed of two segments 2.13 m in length, and either one or two segments of 60.5 cm. One of the long segments is mounted just below the lower half of the diaphragm section. At the top of this segment is a pin joint that supports the whole tube and allows to tilt it to a maximum angle of 7° from the vertical. The second long segment is mounted below the first one; below it is the first segment of 60.5 cm. This segment was specially modified to allow for the installment of the plate retraction mechanism used to prepare an interface in the far end wall configuration. The test section is always mounted below this short tube segment. In the close end wall configuration the interface is located within the test section, a contoured plug molded out of RTV silicon rubber is inserted in the bottom part of the test section, and the end plate is mounted just below the test section. In the far end wall configuration, another short segment (60.5 cm) is mounted below the test section. Contoured plugs molded out of polyester resin are inserted in this segment to adjust the tube end wall to the desired location. The end plate is mounted below the second short segment.

3.2.4 Test Section

The test section consists of four 6160-T6 aluminum plates, 5.1 cm thick, dip brazed together to form a square inner cross section, 11.4 cm on the side (matching that of the driven portion of the shock tube). Its total length is 38.7 cm. The corners are sharp. Hand sculpted epoxy fillets are used to smoothly connect the cross sections of the driven part of the tube (which have rounded corners) to that of the test section. On one wall of the test section is the slot used to install the plate mechanism for preparing the interface in the close end wall configuration. On the two walls perpendicular to the latter are the openings to mount the windows and their frames. When schlieren imaging is performed, the windows are made of optical grade glass, 38 mm thick. In the experiments using X-rays it is necessary to minimize X-ray absorption at the windows. The glass windows are thus replaced by two NARMCO Rigidite 5208/T300 carbon fiber plates 1 mm thick *. To support the composite plates against the pressure from the gases inside the test chamber, a pair of dip brazed aluminum grid structures are used. They consist of aluminum plates 1.5 mm thick and 37 mm wide, the same as the thickness of the glass windows. They are arranged to form 16 cells: the 4 central ones are square while the remaining 12 are rectangular (see Fig. 3.2.2). The spacing of the grids is different for the two crates to account for the parallax due to conicity (6 deg) of the X-ray beam. The central cells of the front and back structures have a side of 28.6 and 32.3 mm respectively. Thus the shadow of the front grid falls on that of the back one, and only one trace is recorded on the film.

3.3 Plate Mechanism

To prepare an interface between two gases of different densities, the shock-tube is equipped with a system (see Fig. 3.3.1) consisting of a thin (1.2 mm) stainless steel plate, a stepper motor to slide the plate in and out of the shock tube, and a plug with a molded RTV rubber gasket to guide the plate in its motion and to seal against leaks from the inside to the outside of the tube. O-rings of 1 mm diameter are glued around the plate to seal against leaks from below to above it. The DC stepper motor (Superior Electric Slo-Syn Model M092-FF402) is connected to the plate by means of a ball screw. The motor is powered by a motion control driver (Superior Electric Modulynx Model PDM155), in turn

* The author gratefully acknowledges Dr. Norman Johnston, of the NASA Langley Research Center, for providing the plates at no cost.

controlled by an 8085 microprocessor board, supplying one TTL pulse per motor step. The system was designed and built by Brouillette (1989). The plate is retracted at a speed of 10 cm/s. To prepare the interface, the plate is inserted in the tube, the heavy gas is slowly (1.5 l/min) introduced in the volume below the plate through an opening in the bottom plugs. As the heavy gas enters, it pushes out the light gas from an opening just beneath the plate, located on the side of the test section in the close end wall configuration, and on the side of the modified tube segment in the far end wall configuration. After about 3 times the volume of gas between the retractable plate and the tube bottom have circulated, the gas below the plate is sufficiently pure to perform an experiment.

The plate is retracted, so that the gases come in direct contact and start to diffuse into each other. During its withdrawal the plate drags along a volume of fluid, due to the no-slip boundary condition on its surface. Once the plate completes its motion out of the test section, the pumped fluid flows back toward the opposite wall as a surface gravity-wave. It is assumed that the induced perturbations are two-dimensional; Brouillette (1989) reports of experiments performed with the plate retracting along the direction of the light beam (instead of normal to it), and states that no 'regular' single scale perturbation was detected, the interface appearing nominally flat. Depending on the amount of time, τ, elapsed between the end of plate retraction and shock arrival at the interface, the wave motion results in different initial conditions. These can not be determined by pictures of the interface taken before its interaction with a shock; but, on the basis of schlieren photographs and X-ray images taken at different times after shock-acceleration of the interface, one can draw the following conclusions: For $\tau < 0.5$ s the interface is a quasi-sinusoidal perturbation at the side where the plate exits and flat and diffused (with random, small scale perturbations) at the opposite side. For $\tau \approx 1.2$ s the interface is quasi sinusoidal across its span; for convenience, this type of interface will be called 'single scale' throughout the rest of this work. For $4.0 < \tau < 8.0$ s, the interface is wholly of diffused type, thicker than for $\tau < 0.5$ s and again, featuring random perturbations of small amplitude; this type of interface will be called 'multiscale' in the rest of the work. Some of the images taken at late times actually suggest the presence of three-dimensional perturbations, but it cannot be determined if these are the developments of disturbances initially on the interface, or the consequence of the interaction of the acoustical waves generated at the wall imperfections with the two-dimensional disturbances on the interface.

From the data generated from the X-ray negatives it is deduced that in some runs stratification takes place in the xenon during its introduction. It is speculated that some leaking occurs along the perimeter of the plate, causing some xenon to enter the air volume above the plate, and some air to contaminate the xenon field below it. The leaks are due to the fact that the surface against which the O-ring glued to the edges of the plate is supposed to seal is interrupted by thin (0.05 mm) slits located between the windows and the frames. Great care was taken in trying to seal the slits by means of silicone rubber, but some minor ones might have remained.

3.4 Pressure Measurements

Two PCB Piezotronics pressure transducers (model 113) are used to record the passage of the waves generated by the refraction at the interface and the reflections at the end wall. In the close end wall configuration they are mounted 30 cm and 71 cm respectively above the interface. In the far end wall configuration they are 37.5 cm and 67.5 cm above the interface. Their sensitivities are 282 mV/bar and 406 mV/bar, respectively. Their output is recorded using Computerscope hardware and software from RC Electronics, mounted on an IBM-AT microcomputer, sampling at a frequency of 125 kHz. From the pressure traces the speed and strength of the incident and various reflected waves are evaluated. The top transducer also provides the trigger signal to the time delay generator which actuates either the X-ray source or the spark gap, depending on the imaging technique used.

3.5 Gases

In all of the experiments the driver gas is nitrogen at room-temperature. The test gas for the radiography experiments is xenon, chosen because of its large X-ray absorption. For the schlieren experiments both xenon and sulfurhexafluoride are used. Properties of the three gases are collected in Table 3.4.1.

Table 3.4.1 Gas Properties @ 25°C, 1 atm

Property	Air	Xe	SF6
Molecular mass m(kg/Kmol)	29	131	146.07
Density ρ (kg/m^3)	1.18	5.46	5.97
Atwood ratio A	0	0.637	0.668
Specific heat ratio γ	1.4	1.667	1.09[1]
Kinematic viscosity ν (10^{-6}m^2/s)	15.7[2]	4.119	2.47[3]
Diffusion coefficient in air[4] F (cm^2/s)	0.204	0.124	0.097
Index of refraction (for mean of sodium D lines)	1.000264[5]	1.000702[6]	1.000717[7]

3.6 Imaging Techniques

3.6.1 Radiography

Figure 3.6.1 shows a plan view of the experimental layout. A flash X-ray source (Hewlett-Packard Flash X-Ray Electron Beam System Model 43731A) is mounted 1.83 m from the rear window of the test section, with its axis perpendicular to the planes of the windows and to the direction of motion of the plate. The source generates a 50 ns X-ray flash. At each run a 20×25 cm 3M-XM X-ray negative (manufactured for medical imaging), sandwiched between two 3M-T12 fluorescent screens (also used in medical diagnostics) in a

1 Stull & Prophet (1971)

2 Kreith & Black (1980)

3 Baker & Mossman (1971)

4 Calculated using molecular theory from Hirschfelder *et al.*(1954)

5 Liepmann & Roshko (1957)

6 Kaye & Laby (1971)

7 Marshall (1976)

film-holder mounted on the outside of the rear window, is exposed. A schematic of the film holder and the test section is presented in Fig. 3.6.2. The film holder is mounted with its left, short side aligned with the left, vertical edge of the windows (as seen from the X-ray source) and it extends 3.4 cm beyond the right side of the test section. A pair of aluminum step-wedges (of thickness ranging from 0.3 to 14.4 mm, and density $\rho_{Al} = 2.7$ kg/m^3) are placed on the front of the film holder, in the area not covered by the test section. Thus, when the X-ray flash is fired, the images of the gases inside the test section and of the aluminum step wedges on its side are recorded on the negative; the aluminum step wedges are used for calibration, as described in Sec. 4.1.

3.6.2 Schlieren System

The setup consists of a standard layout (see Fig. 3.6.3). A spark gap, with a 10 kV 0.1 μF capacitor, is located at the focus of a spherical mirror (of focal length 1.5 m and clear aperture 20 cm). The diverging light beam is collimated by the mirror and reflected through the test section. An identical mirror collects the parallel beam and focuses it onto a knife edge. The image is recorded on Ilford XP-1 film (400 ASA) with a Nikon FE2 camera, using an 85 mm Nikkor lens mounted on bellows. To adjust the schlieren sensitivity the position of the knife edge can be varied with a precision x-y positioner.

3.7 Operation

At the beginning of each run the driver section is pressurized to about 0.7 atm below the bursting pressure of the diaphragm in use; the boost tank is pressurized to 41 atm or 81 atm, depending on the diaphragm thickness. When an X-ray image is to be taken the X-ray pulser is charged to 80 kV. To run a schlieren visualization experiment, the room lights are turned off and the camera shutter is opened. An 8085 microprocessor board controls the experimental sequence which consists of: Retracting the plate from the test section; let the desired time interval elapse (so as to prepare the interface of interest); open the high flow-rate solenoid valve thus discharging the high-pressure boost-tank into the driver section. This ensures diaphragm rupture within 500 ms of the solenoid valve opening. As it travels toward the interface, the shock passes in front of the two pressure transducers. The signal from the uppermost transducer triggers the digital delay box that fires either the X-ray flash or the spark gap.

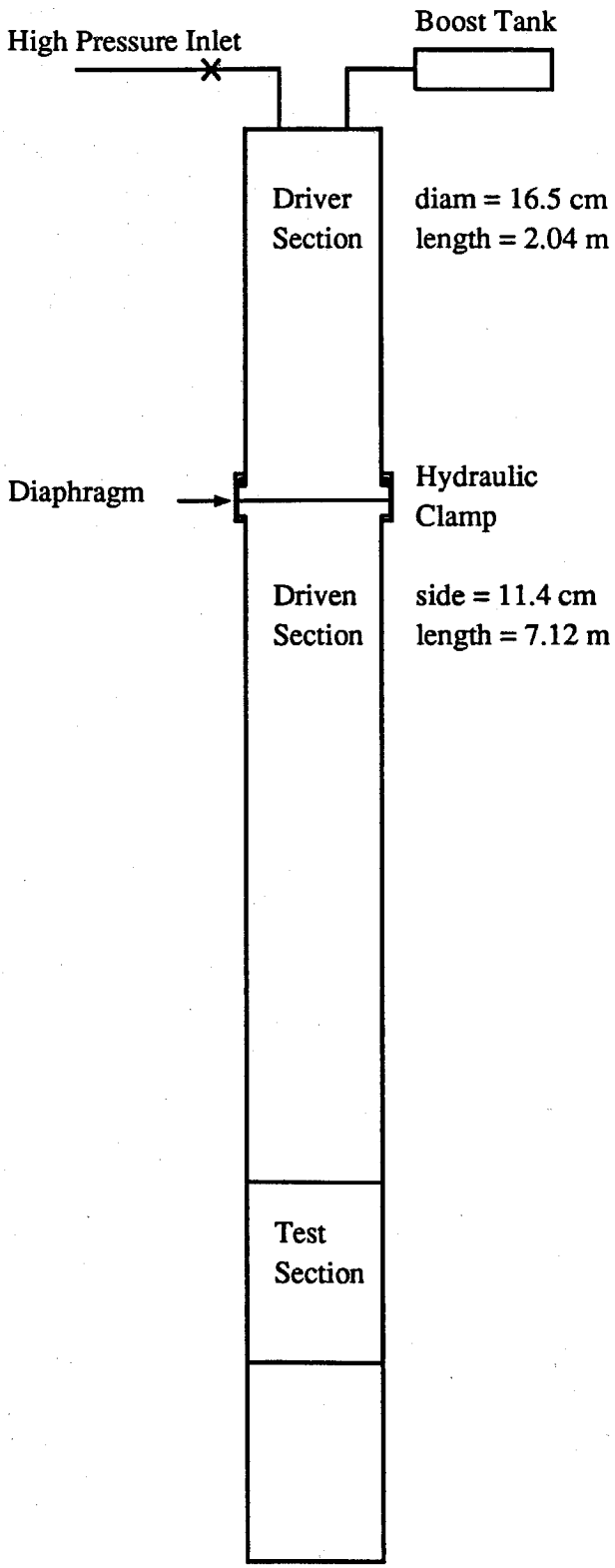

Fig.3.1.1 Schematic of GALCIT Vertical Square Shock Tube.

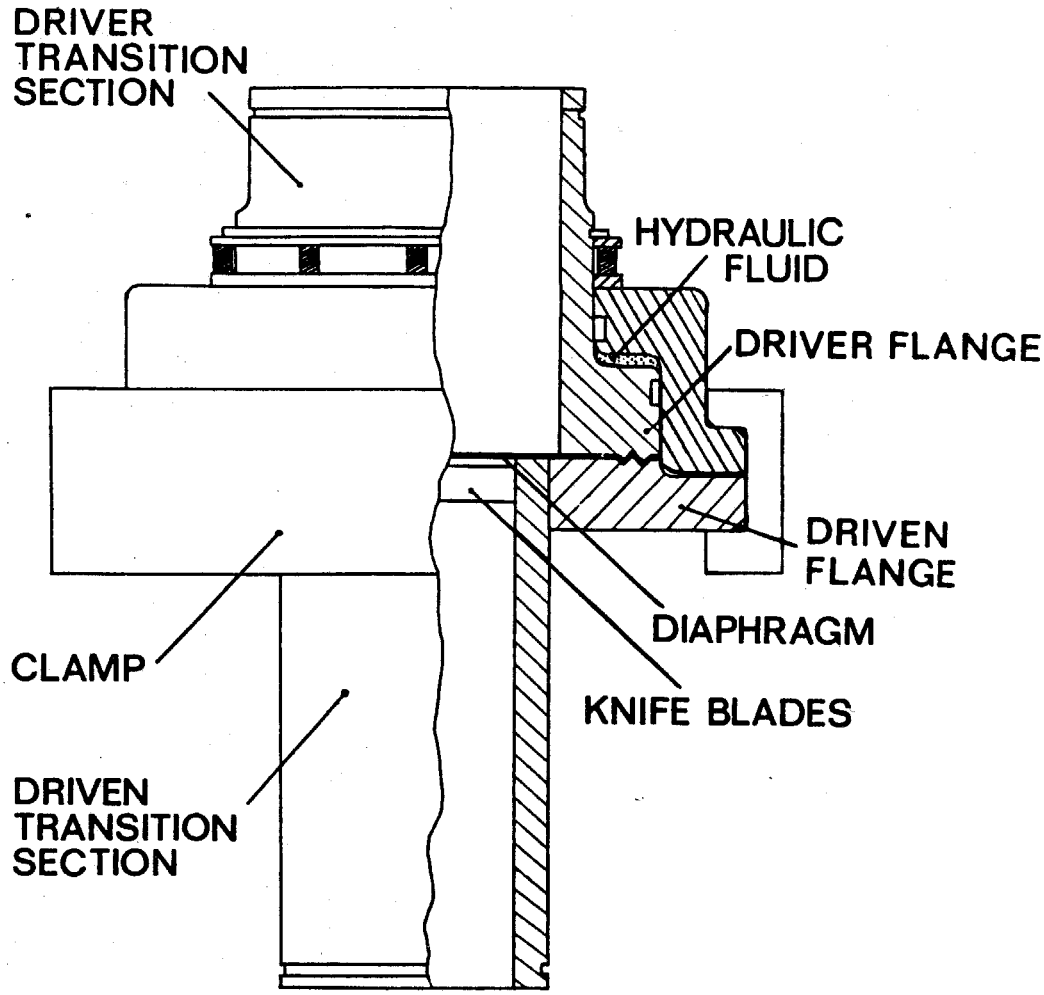

Fig.3.2.1 Diaphragm Section, from Brouillette (1989).

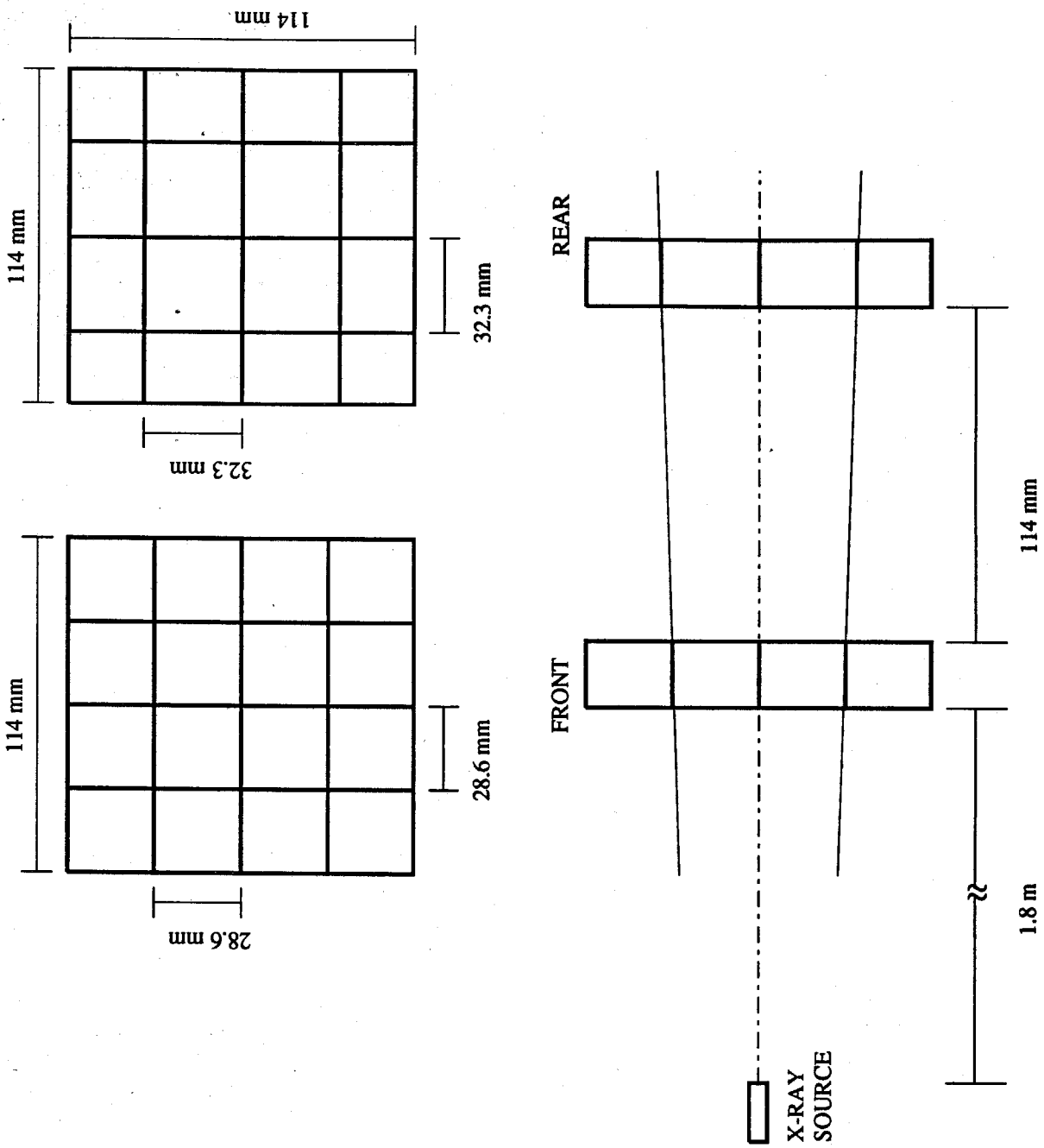

Fig.3.2.2 Support Structure for the Carbon Fiber Windows.

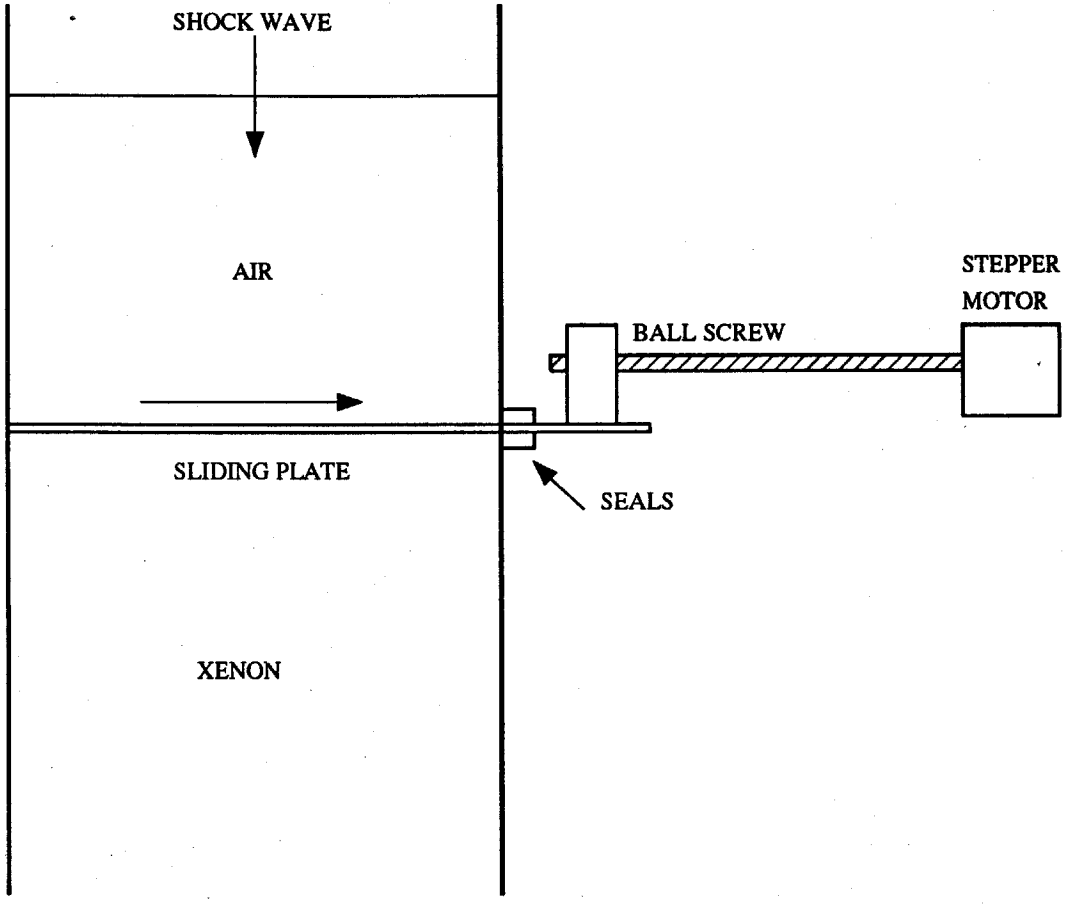

Fig.3.3.1 Plate Retraction Mechanism.

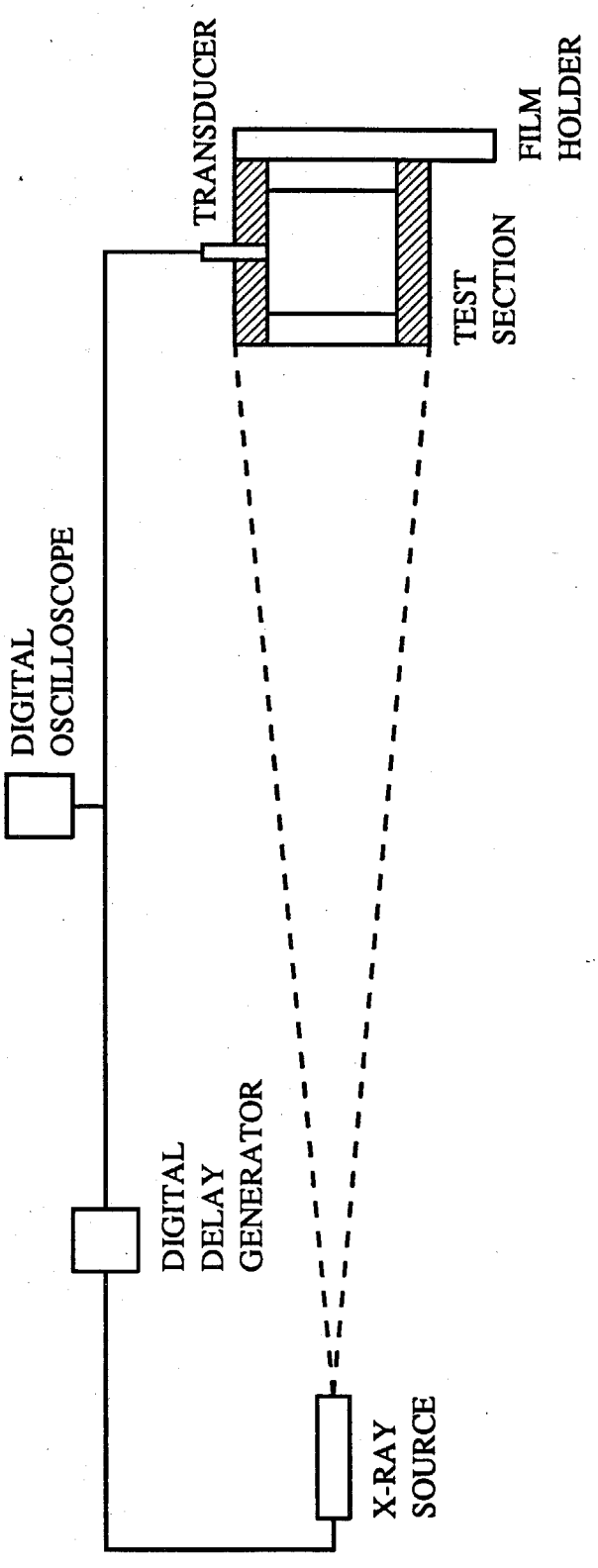

Fig.3.6.1 Layout of X-Ray Imaging System.

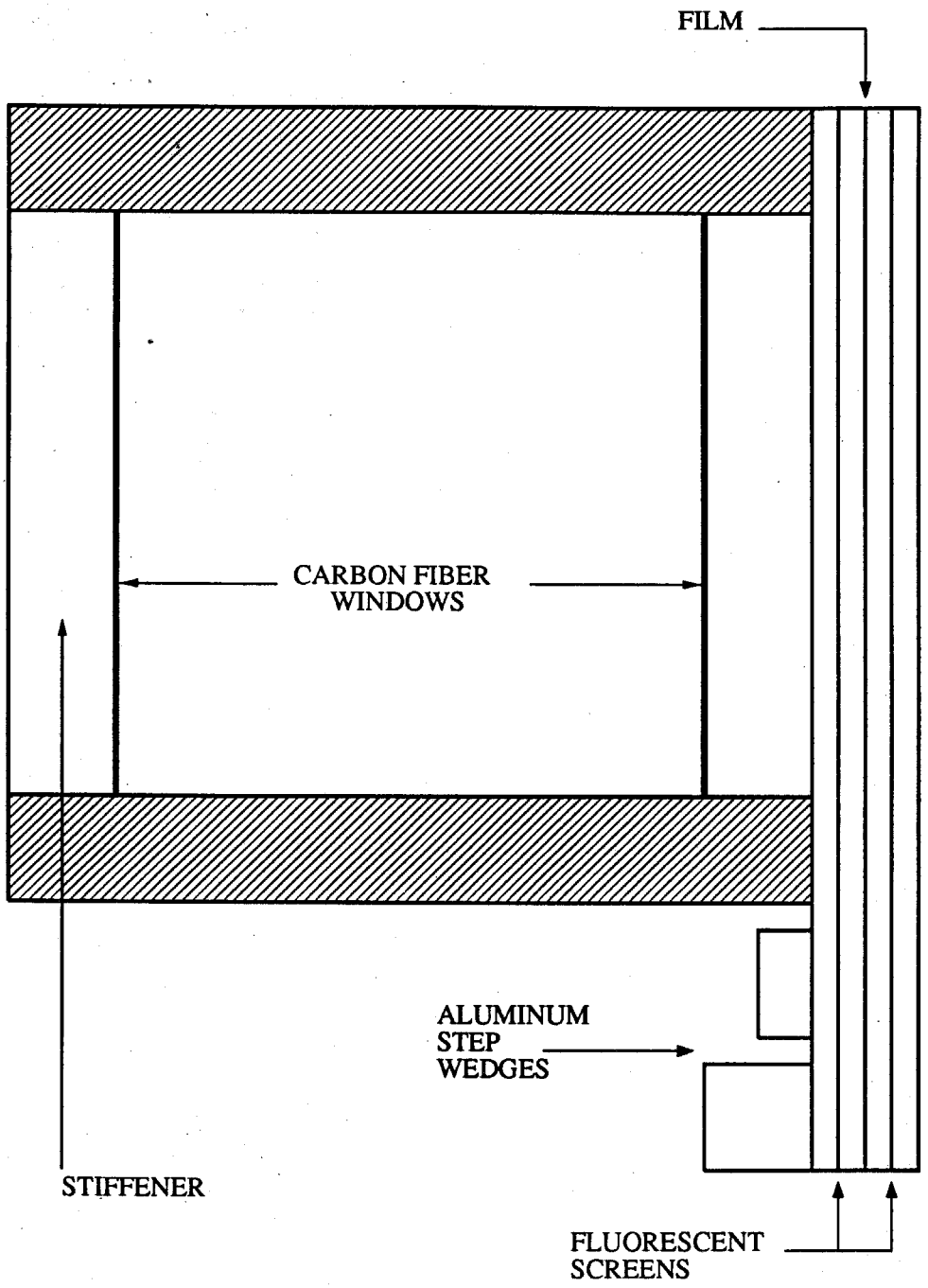

Fig.3.6.2 Detail of Test Section and Film Holder.

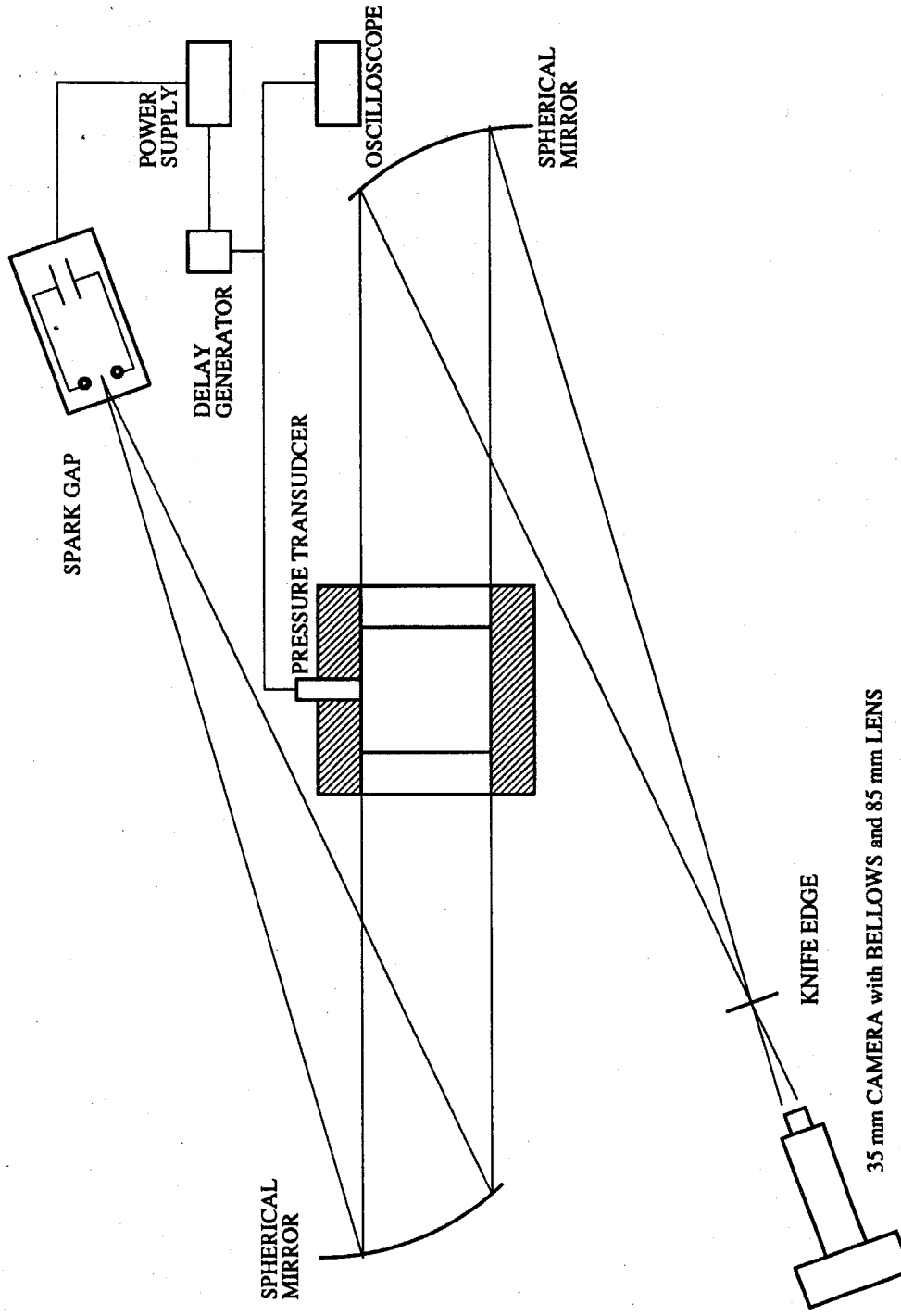

Fig.3.6.3 Layout of Schlieren Imaging System.

CHAPTER 4

IMAGE ANALYSIS

4.1 Image Processing

The image recorded in any given run on an X-ray negative consists of three main portions: One at the left of the picture, corresponding to the test section; one in the middle, corresponding to the side wall of the test section and one to the right corresponding to the aluminum step wedges. The middle portion is removed from the developed negatives, since it carries no information, and the two remaining parts are joined together.

The optical density of the developed film is measured by:

$$D = \log \frac{I_v}{I_{v0}} . \tag{4.1.1}$$

where I_{v0} is the intensity of a beam of visible light incident on one side of the negative, and I_v the intensity of the beam of light transmitted through the negative. The optical density is a monotonic function of the exposure, which in turn is a time integral of the intensity of the X-rays that reach the fluorescent screens between which the film is sandwiched. The intensity is spatially modulated by the xenon (in the test section) and by the aluminum step wedges, following Lambert's law:

$$\frac{I_x}{I_{x0}} = e^{-\sigma(P_E)\rho l} , \tag{4.1.2}$$

where I_{x0} is the intensity of the X-ray beam, of photon energy P_E, impinging on thickness l of a material of density ρ and X-ray absorption coefficient $\sigma(P_E)$, and I_x is the intensity of the X-ray beam emerging from the slab. In the present case, the aluminum has a spatially constant density and variable thickness, as described in Sec. 3.6.1. The xenon on the other hand has constant thickness (the depth of the test section) and density varying in space, $\rho_{Xe} = \rho_{Xe}(x, y, z)$ (from now on the subscript Xe will be dropped, and the symbol ρ will always refer to xenon density, unless otherwise specified).

When the density varies in the z-direction, Lambert's law takes on the form

$$\frac{I_x}{I_{x0}} = e^{-\sigma(P_E)\int_0^l \rho(x,y,z)dz} . \tag{4.1.3}$$

The term

$$d = \sigma \int_0^l \rho dz \tag{4.1.4}$$

is the optical depth of the medium traversed by the X-ray. The measured density is therefore the average across the depth of the test section. X-ray absorption is low in regions of low xenon density and the radiographs appear correspondingly dark (high D); conversely, X-ray absorption is large in regions of high xenon density and the negatives are more transparent there (low D). Through an appropriate calibration, one can link the optical density of the film to the local xenon density.

Image processing begins with the digitization of the negatives. A Truelite DC backlight Illumination System is used to illuminate the X-ray plate; a Sony AVC-D1 CCD images the plate and its output is sent to an Epix Inc. Silicon Video Frame Grabber (installed on an IBM AT microcomputer) which yields a field of 376 × 480 8-bit pixel values. The system is schematically depicted in Fig. 4.1.1. In processing this field it is necessary to account and correct for the following items:

1. Temporal fluctuations of the intensity of the illumination box and of the CCD output
2. Calibration of the CCD response
3. Spatial nonuniformity of the illumination box
4. CCD 'pixel noise' (spatial fluctuations)
5. Spatial nonuniformity of the X-ray beam
6. Relationship between xenon density and aluminum thickness
7. Temporal variations of the X-ray beam (from shot to shot) both in spatial distribution of the intensity and in spectral composition

To reduce the noise due to the time fluctuations of the light box and CCD outputs (item 1) 25 digitizations of the image $V(x,y)$ are averaged into one final record. The intensity distribution $V_0(x,y)$ of the backlight illumination system without any negative is also recorded.

The relationship between the response $V(x,y)$ of the CCD camera to light intensity $I_v(x,y)$ (item 2) is determined using a series of commercially available neutral density filters illuminated by the backlight source. The quantity I_v/I_{v0} is known for each filter. Measurements of both neutral density filters and X-ray negatives with our system must be corrected for spatial nonuniformity of the CCD response and of the backlight source (items 3 and 4). This is accomplished by correcting the response $V(x,y)$ of the CCD camera recorded by the frame grabber with the signal $V_0(x,y)$ recorded without any filter or negative,

$$V_c(x,y) = \frac{V(x,y)}{V_0(x,y)/\overline{V}_0}\,, \tag{4.1.5}$$

where $\overline{V}_0$ is the average reference signal over the entire backlight source.

To obtain the CCD response, the corrected values are averaged over the area of each filter to determine $V_c(I_v/I_{v0})$. A linear fit

$$V_c = b_1\frac{I_v}{I_{v0}} + b_2 \tag{4.1.6}$$

is shown in Fig. 4.1.2, where $b_1 = 399.4$ and $b_2 = 28.4$ are the slope and the vertical intercept, respectively. This result is applicable to the processing of X-ray negatives if the viewing region of the CCD camera on the backlight source is always maintained the same. The optical density of a digitized negative follows from Eq. 4.1.1 and Eq. 4.1.6

$$D(x,y) = \log\left(\frac{b_1}{V_c(x,y) - b_2}\right). \tag{4.1.7}$$

X-ray negatives exposed with no xenon or aluminum step wedges , showing the 'background field', have shown that the X-ray intensity is not spatially uniform (item 5). The only corrections that can be made to account for this error are on the optical density of portions of the negatives from each run where the gas field is uniform. It is therefore necessary to make use of the relationship between optical density (D) and exposure (E). A portion in the range $0.22 < D < 2.2$ (the limits of the range covered in our experiments) of

the relation between D and E, obtained in plotted form from 3M, Inc., is fitted with the function

$$\frac{D - D_{min}}{D_{max} - D_{min}} = \frac{\tanh(p_1 \log E - \log E_0) + 1}{2} \tag{4.1.8}$$

and is shown in Fig. 4.1.3. Here p_1 is a scaling factor. Observation of the background-field negatives shows that most of the spatial nonuniformities of the X-ray beam are in the horizontal direction. Thus the correction is made using the signals from reference strips at the top and bottom of the negative where the air and xenon fields, respectively, are uniform.

The optical density distribution $D_r(x)$ in a 25-pixel-high reference strip at the top of each negative is evaluated. The strip is chosen to be entirely in a region about 300 pixels wide occupied by air, both in the test section and above the aluminum wedges, where X-ray absorption by xenon is always zero. The optical density is averaged at each value of x over the height of the strip. The distribution of exposure across the strip $E_r(x)$, is then evaluated from the $D = D(E)$ curve. The same is then repeated for a strip at the bottom of the test section, entirely in the xenon field (not extending to the aluminum wedges).

The method is to determine by how much the exposure at a each x-location on the strip differs from the maximum exposure reached in the strip, $\Delta E(x) = E_{max} - E_r(x)$. This is used as a measure of the spatial variations of the intensity of the incoming X-ray beam at the top and bottom of the film plate. The variations in the y-direction, at a fixed x, are estimated as a linear interpolation between the top and bottom values. In this manner, one can generate a matrix $\Delta E(x, y)$. In particular, at each x-location in the negative one can correct the optical density in four steps:

i. Measure the local optical density $D(x, y)$;

ii. Deduce what the exposure $E(x, y)$ is, through the $D = D(E)$ curve;

iii. Generate the correct value of the exposure by adding the correction term for that location $E_c(x, y) = E(x, y) + \Delta E(x, y)$;

iv. Deduce the corrected optical density D_c from the $D = D(E)$ curve using the corrected value of exposure $E_c(x, y)$.

The corrected optical density field $D_c(x, y)$ is the one from which $\rho = \rho(D_c)$ is sought. From now on the subscript 'c' will be dropped and D will always refer to the corrected

optical density. The link between xenon density and grey level is the product of the relation between xenon density and aluminum thickness (generated once from radiographs of known xenon density, item 6) and the relation between aluminum thickness and optical density (generated for each negative). Rigorously, a 'xenon wedge' (*e.g.* a prism with depth varying linearly from its bottom to its top, with front and back surfaces consisting of carbon fiber plates of the same type used for the test section windows, and containing pure xenon) should have been used in place of the aluminum step wedge, so as to eliminate one unnecessary step (the $\rho = \rho(l_{Al})$ relation; item 6) in the calibration procedure. This was not pursued, due to the greater simplicity of fabricating the aluminum wedges.

If the X-ray beam were monochromatic it would be possible to determine $\rho(l_{Al})$ simply from absorption coefficient data available in the literature. But since the X-ray source used in the present experiments emits with an unknown spectral distribution, a calibration cell was designed and fabricated especially for measuring the correspondence between xenon density and aluminum thickness. It consists of a hollow cylinder, of inner diameter 12.7 mm and length 11.4 cm (the same as the side of the test section). The cell is closed at both ends by carbon fiber plates identical to those used as windows in the test section. The cell is filled with xenon at pressures ranging from 0.35 bar to 3.45 bar, corresponding, at room temperature, to densities in the range from 1.86 kg/m^3 to 18.58 kg/m^3. For each negative, the averaged optical density of each aluminum step is evaluated and the function

$$l_{Al} = p_0[\mathrm{csch}(D - p_1) - \mathrm{csch}(p_2 - p_1)] \qquad (4.1.9)$$

is fitted through the data points with a nonlinear least squares fitting algorithm to determine the $l_{Al} = l_{Al}(D)$ relation, l_{Al} being the aluminum thickness, for that negative. This function is similar in shape to that of Eq. 4.1.8 (see Fig. 4.1.3), which is the shape that best fits the optical density *vs.* exposure data (Fig. 4.1.3). The relation between aluminum thickness and optical density should follow a similar law since the logarithm of the exposure is a linear function of the aluminum thickness. The dependence of Eq. 4.1.9 is chosen because it follows the data better than the hyperbolic tangent function at low values of D. The curves resulting from this procedure, for the runs with the calibration cell, are shown in Fig. 4.1.4. The difference between the different curves is due to shot-to-shot variations of the X-ray source intensity and spectral distribution. Collapsing the curves onto a single one, by plotting $[l_{Al}/p_0 + \mathrm{csch}(p_2 - p_1)]$ *vs.* $\mathrm{csch}(D - p_1)$, (see Fig. 4.1.5) shows that the

scatter in the data is at most 6%, thus indicating that the selection of Eq. 4.1.9 for the non linear fit is an appropriate one. Next, the averaged optical density of the xenon region of the cell, D_{Xe}, is evaluated for every negative. For each negative the aluminum thickness equivalent to the xenon density is found by inverting $D_{Xe} = D(l_{Al})$. A set of eight (l_{Al} , ρ) pairs is generated and a linear least squares fit performed through the data, yielding

$$\rho\,(\mathrm{kg/m^3}) \;=\; 1.83\, l_{Al}\,(\mathrm{mm})\,. \tag{4.1.10}$$

This is the desired $\rho = \rho(l_{Al})$ relation, shown in Fig. 4.1.6.

For every negative from actual shock tube experiments, the optical density of the various aluminum thicknesses is measured and a non linear least squares fit through these data to Eq. 4.1.9 is performed, yielding the $l_{Al} = l_{Al}(D)$ correspondence for the given experiment. By combining this $l_{Al} = l_{Al}(D)$ law with Eq. 4.1.10, one gets the $\rho = \rho(D)$ for that plate, an example of which is shown in Fig. 4.1.7. This operation is repeated for each negative, thereby accounting for the shot-to-shot variations of the X-ray tube (item 7). To summarize the calibration results, $\rho(D)$ is fitted to the same function as l_{Al}, *viz.*

$$\rho \;=\; p_0[\mathrm{csch}(D - p_1) - \mathrm{csch}(p_2 - p_1)]\,. \tag{4.1.11}$$

The results are plotted in Fig. 4.1.8. As before the scatter is due to shot-to-shot variations. Collapsing the data (Fig. 4.1.9) yields three parameters, p_0, p_1, p_2, presented in Table 4.1.1. The first parameter measures energy, the second measures effective absorption coefficient of the X-ray beam and the third measures the fog level of the X-ray plates.

This concludes the discussion of all the items in the list of the necessary corrections.

An example of the application of this procedure is shown in Fig. 4.1.10: From the profile of corrected (items 1, 2, 3, 4, 5) optical density across the interface at a fixed $x-$location (a), through the calibration curve for the negative (items 6, 7) (b), one gets the corresponding xenon density profile (c). This last plot shows that a linear interpolation has been carried out across the horizontal walls of the stiffening structure (corresponding to the three spikes in (a)).

Table 4.1.1. Parameters for the Non Linear Least Squares Fit of the Calibration Data.

Run #	p_0	p_1	p_2
0295	2.02032	0.231000	0.876000
0296	1.17669	0.257000	0.790000
0297	2.90787	0.210000	1.00700
0298	2.29482	0.226000	1.12500
0299	2.36070	0.232000	1.22400
0300	1.38348	0.259000	0.969000
0301	5.75169	0.171000	1.42400
0302	2.23260	0.269000	0.917000

4.2 Data Reduction

In these experiments we measure the distortion and thickness of the interface. The distortion is the manifestation of the Richtmyer-Meshkov instability; the thickness is a consequence of the mixing induced at the interface by the vorticity baroclinically generated at the time of interaction with the shock wave.

4.2.1 Interface Distortion

In order to study the distortion of the interface a 'mean interface shape' is constructed from the density data. It is then decomposed into its Fourier modes and the time evolution of each mode is examined. To define a 'mean interface shape' a xenon density profile is constructed for each vertical column of pixels in the image. The y-coordinate of the centroid of the density profile at each x-location is calculated from

$$y_c(x) = \frac{\int_0^Y \rho(x,y)dy}{\rho_m}, \tag{4.2.1}$$

(see Fig. 4.2.1) where Y is the height of the field of view in the test section and ρ_m is the asymptote in the xenon field. The locus of all these centroids is the mean interface shape $y_c(x)$. The shape constructed by Eq. 4.2.1 exhibits high frequency noise (partly due to the CCD noise unsuppressed by averaging over 25 digitizations, and partly to the graininess of the film) and three interruptions corresponding to the vertical elements of the stiffening grid. The gaps are filled by linear interpolation. To carry out a modal analysis of $y_c(x)$, its spatial

spectrum is constructed by FFT. To minimize the undesired effects of truncation in physical space (like leakage through the side-lobes of the FFT of the rectangular box function, *i.e.* the $\sin(k)/k$ function) the function $y_c(x)$ is windowed with a Hanning function, given by

$$H(x) = \frac{1}{2}[1 - \cos(\frac{2\pi x}{L})] \tag{4.2.2}$$

where L is the width of the field of view. To generate a smooth interface shape, the FFT of $y_c(x)$ is taken without the use of the Hanning window, and the shape is reconstructed using only the first six modes of the spectrum (a low-pass digital filter in the frequency domain). An example is presented in Fig. 4.2.2, superimposed to the noisy shape from which it is generated. Partial reconstruction without windowing suffers from truncation effects, as can be seen at the extreme edges.

4.2.2 Interface Thickness

To determine the interface thickness from the density data, one needs a density profile, $\overline{\rho}(y)$, free of any artificial thickening introduced by averaging over the distortion of the interface. In the extreme case, obtaining a density profile of a discontinuous, sinusoidal interface, by averaging across its entire span, does not give a step function but a curve with a finite gradient, and the interface thickness deduced from this curve coincides with the amplitude of the sinusoid. To avoid that, before averaging, the profile at each x-location is shifted vertically, by the distance between its centroid and a reference centroid. This is equivalent to making the interface perfectly flat. A typical result of this operation, on the data with interface distortion given in Fig. 4.2.2, is the density profile shown in Fig. 4.2.3. (The values of x_l and x_r indicated in the caption represent the x-positions, in mm, of the leftmost and rightmost profiles used for the averaging, respectively.) Then the interface thickness, δ, is defined by (see Fig. 4.2.3):

$$\delta = h_1 + h_2 \tag{4.2.3a}$$

where

$$h_1 = \frac{1}{\rho_c}\int_{y_c}^{Y} \rho dy \tag{4.2.3b}$$

and

$$h_2 = \frac{1}{\rho_m - \rho_c}\left(\rho_m y_c - \int_0^{y_c} \rho dy\right) . \tag{4.2.3c}$$

Here ρ_c and y_c are the values of xenon density at the centroid, and its $y-$position. This definition corresponds to finding the height of the two rectangles whose bases are the xenon density at the centroid and the difference between the maximum xenon density and that at the centroid, and whose areas are the same as those of the regions delimited by the density profile, the horizontal line through its centroid and the two asymptotes of the profile. In Fig. 4.2.3, cross-hatching indicates equivalence of areas 1 and 2 and areas 3 and 4, respectively. When the asymptote in the xenon field is oblique rather than vertical, a trapezoid is used instead of a rectangle, as shown in Fig. 4.2.4. This oblique asymptote indicates a stratification in the xenon, possibly due to some small leaks along the perimeter of the plate separating the xenon from the air above. The thicknesses obtained from profiles with oblique asymptotes are indicated with circles in the figures of Ch. 5 and Ch. 6.

4.2.3 Density Contour Plots

Another way to examine the data is to generate contour plots of the density field. To that end, the density values are linearly interpolated across the walls of the stiffening structure. To avoid the effects due to truncation in physical space, the mirror image of the density field with respect to the x and y axes is constructed, rendering the field periodic. It is then smoothed using an ideal low pass filter, in the frequency domain. This filter is a cylinder of height 1 and elliptical cross section. The two semiaxes correspond to the number of modes used in the x and y directions, respectively. The example shown in Fig. 4.2.5 is generated with a filter having 20 and 40 modes in the x and y directions, respectively. The dashed lines in the figure indicate the position of the walls of the stiffening structure across which the data is interpolated.

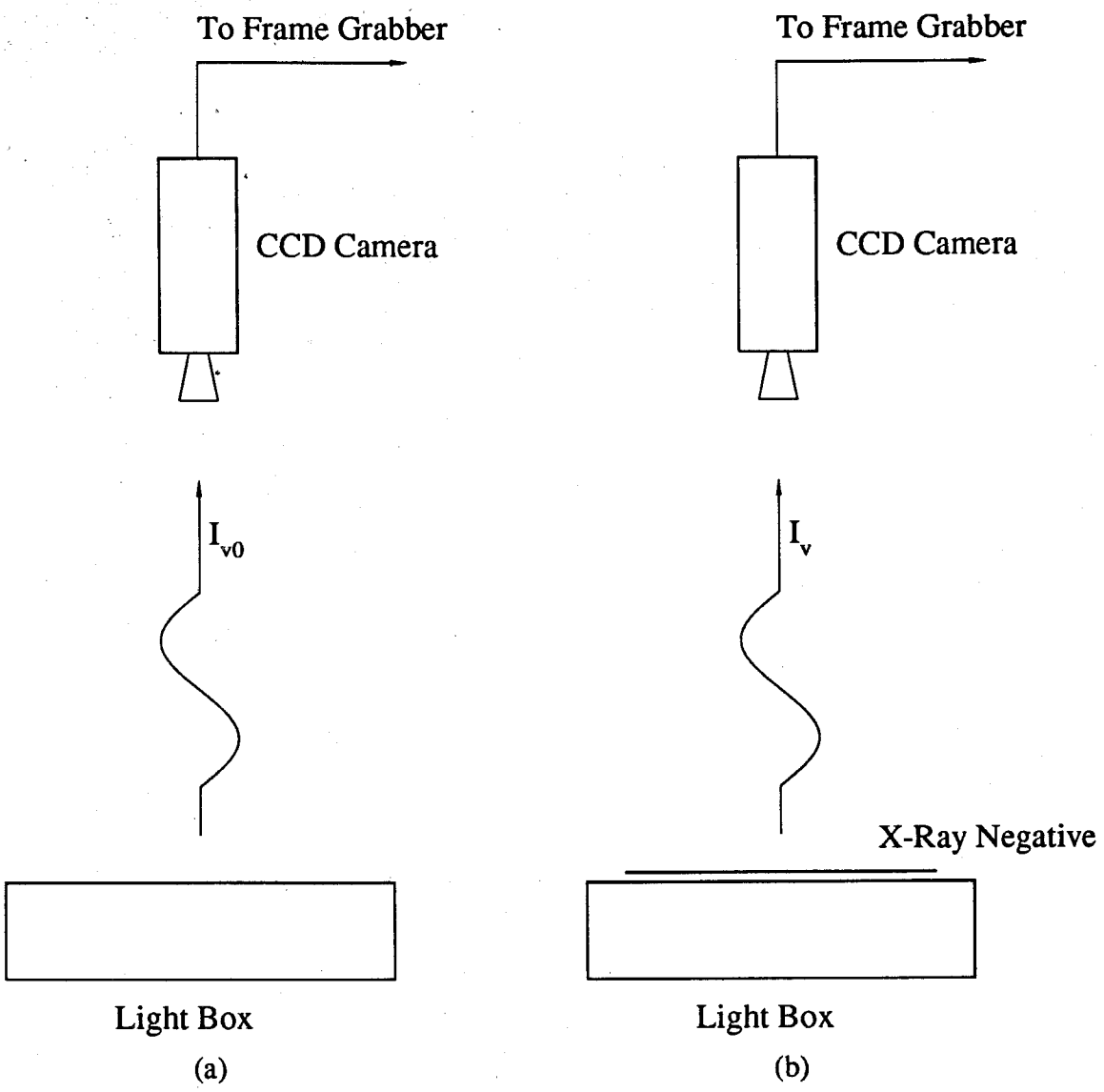

Fig.4.1.1 System for the Digitization of the X-ray Negatives. a) Digitization of the Illumination Background. b) Digitization of the Negative.

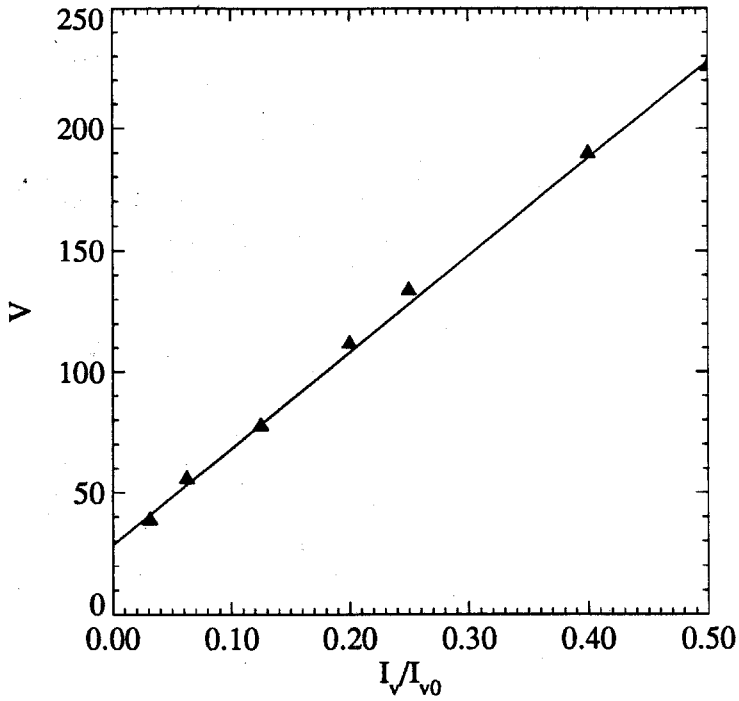

Fig.4.1.2 CCD Camera Response.

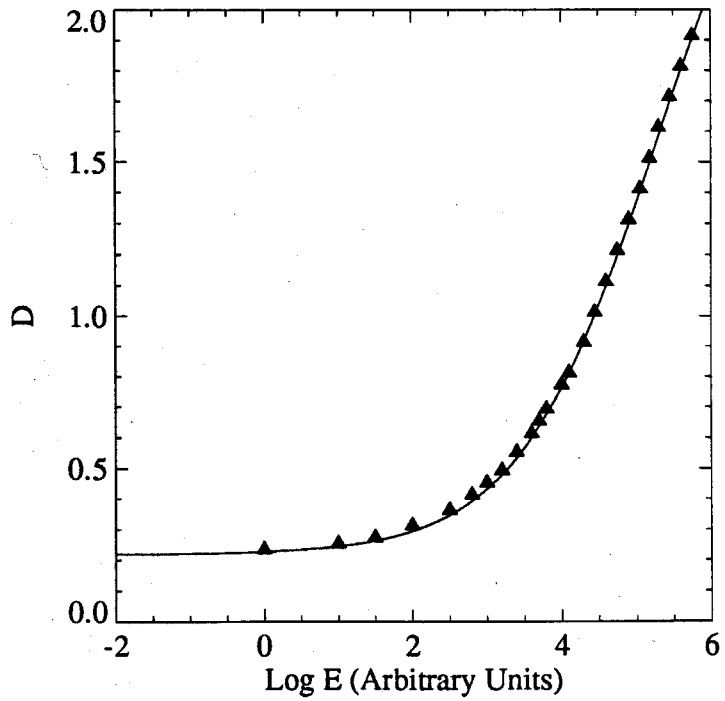

Fig.4.1.3 Response of 3M-XM Film with 3M-T12 Screens to Exposure.

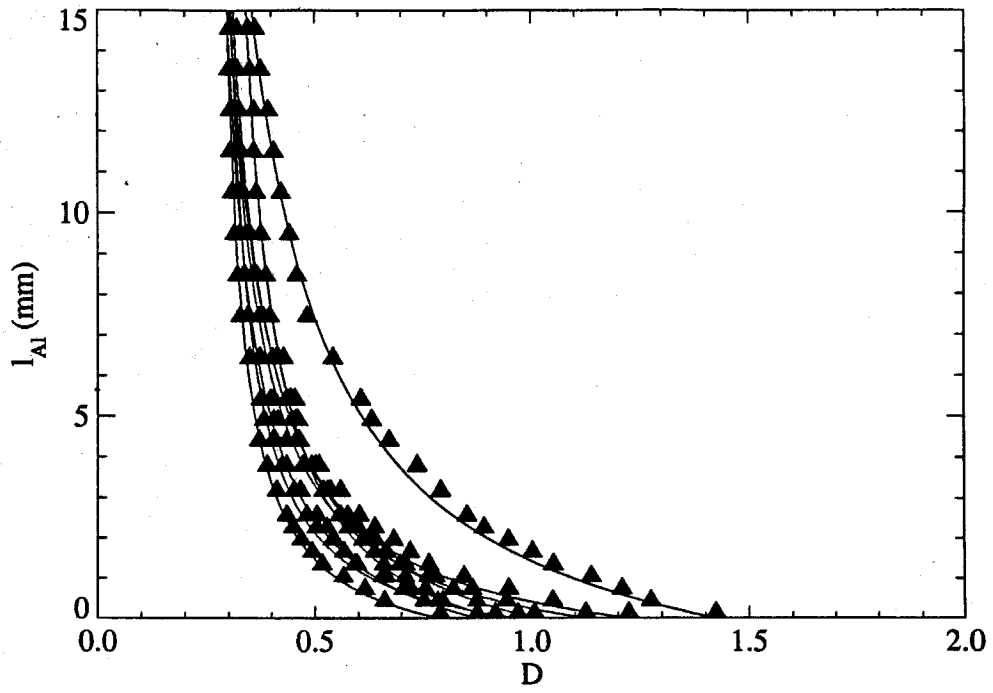

Fig.4.1.4 Aluminum Thickness *vs.* Film Density for Calibration Radiographs.

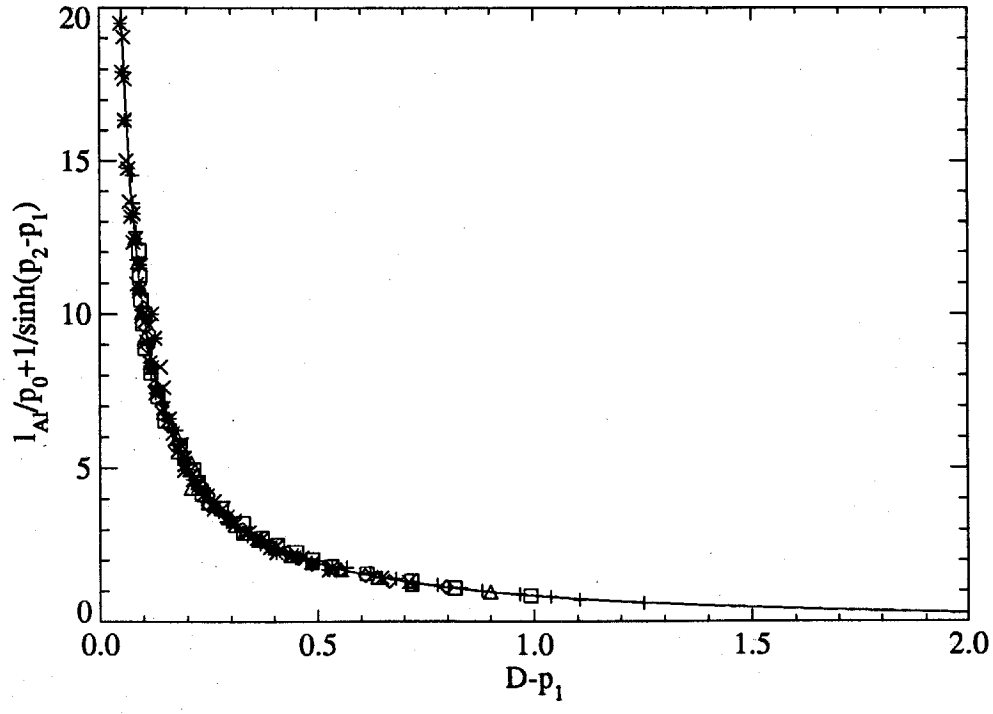

Fig.4.1.5 Normalized Curves from Fig. 4.1.4.

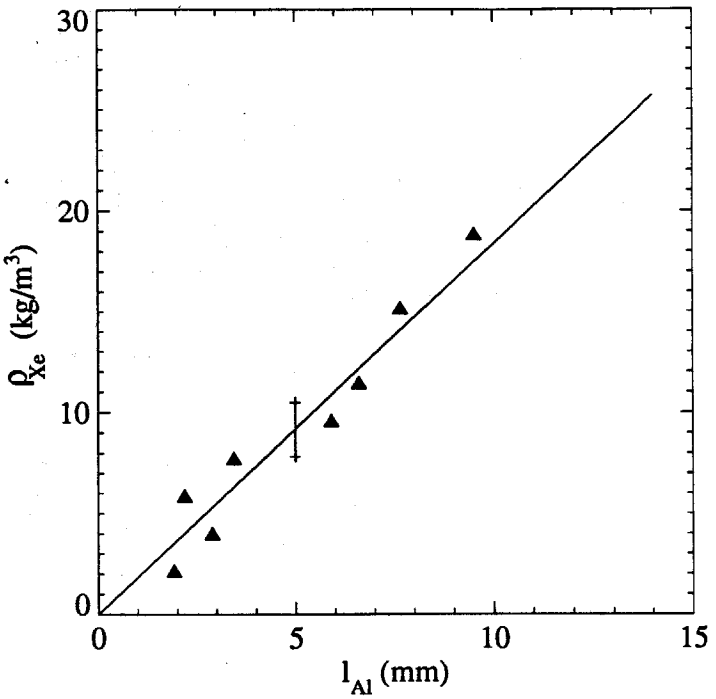

Fig.4.1.6 Calibration of Xenon Density *vs.* Aluminum Thickness.

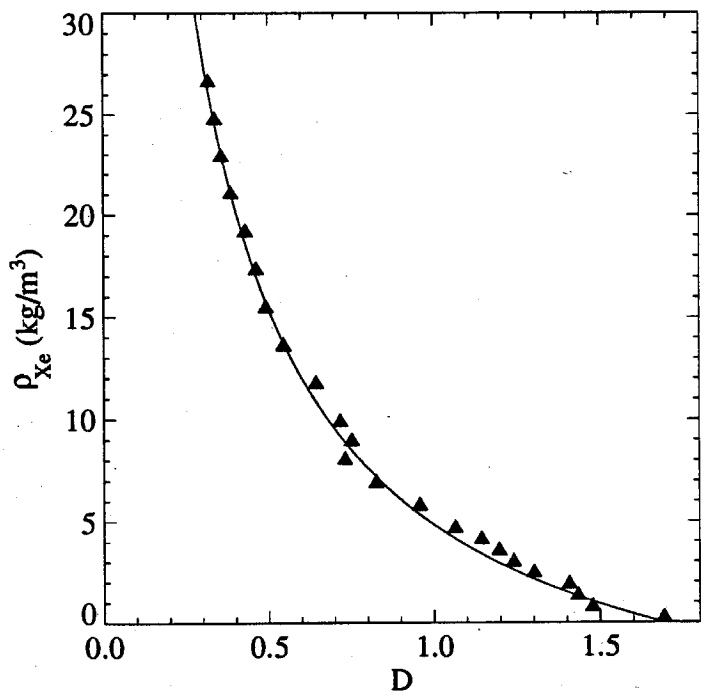

Fig.4.1.7 Example of Calibration Curve for an X-ray Negative. Run #0547, CEW, τ = 8.0s, M_i = 1.32, t = 1.08ms.

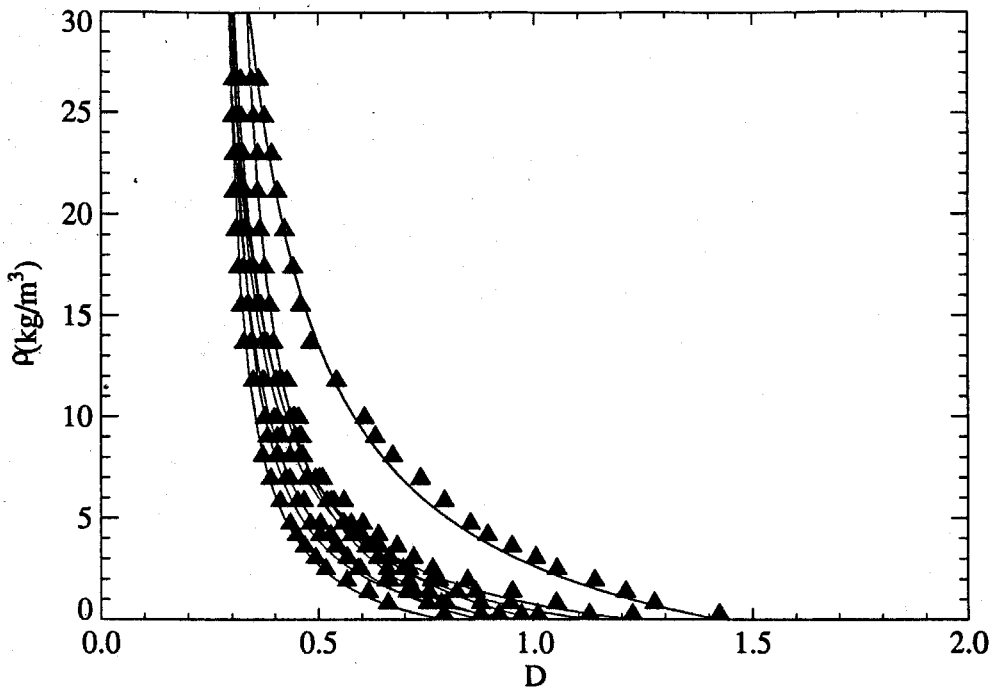

Fig.4.1.8 Xenon Density *vs.* Film Density for Calibration Radiographs.

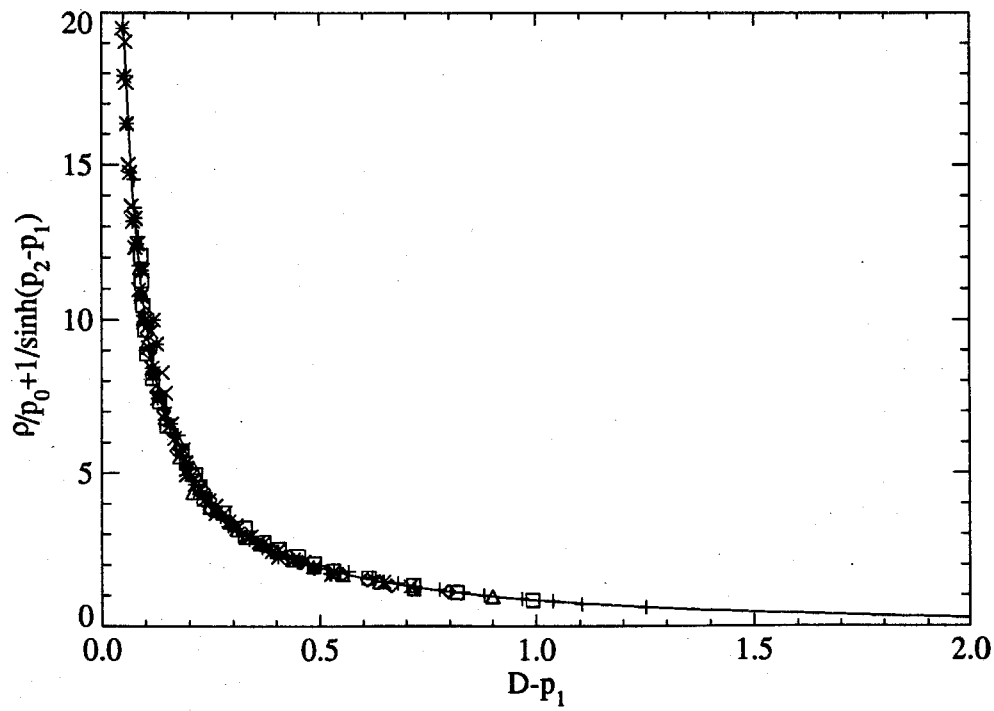

Fig.4.1.9 Normalized Curves from Fig. 4.1.4.

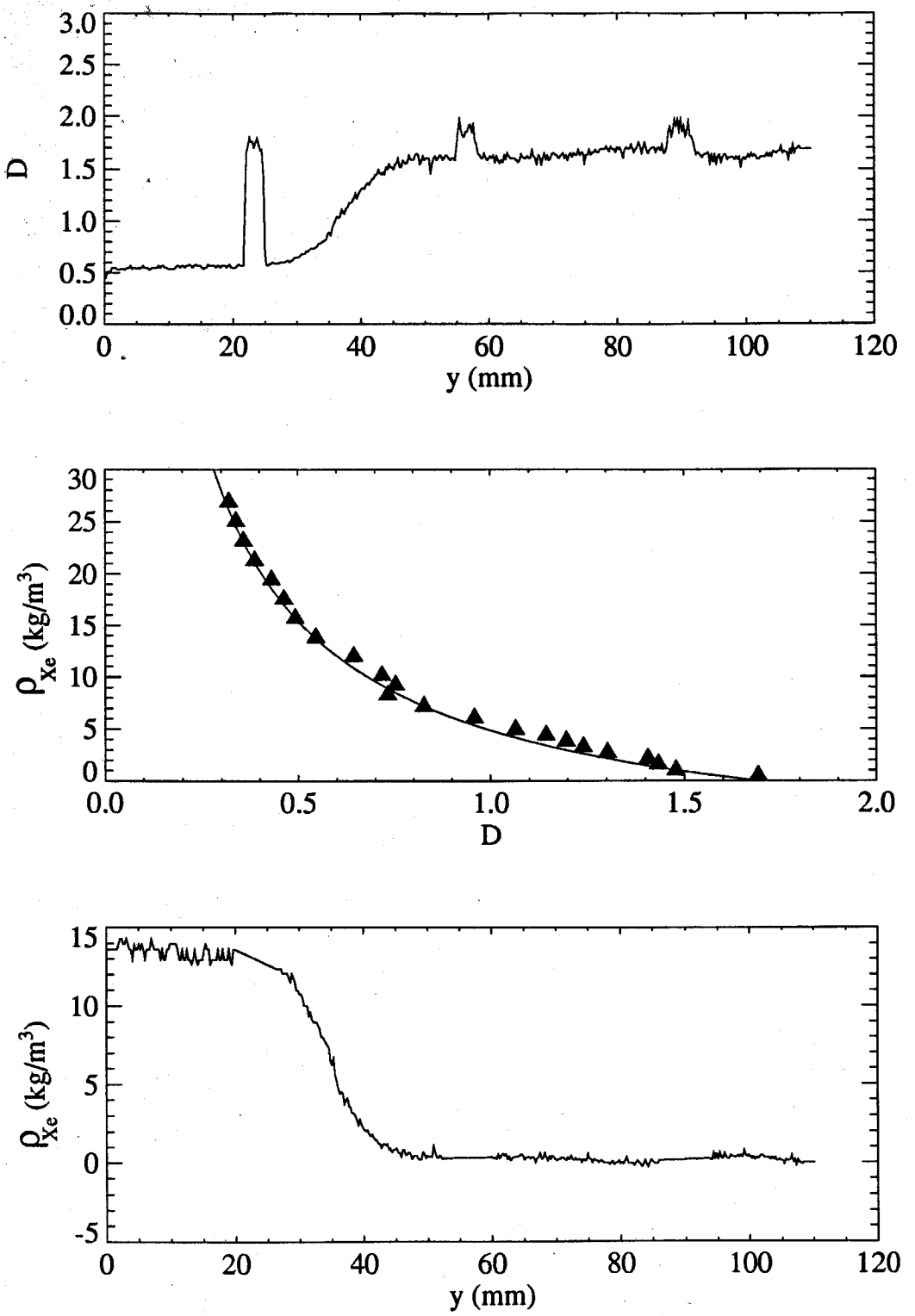

Fig.4.1.10 Calibration Steps: From an Optical Density Profile (a), through the Calibration Curve (b), to a Xenon Density Profile (c). Run #0547, CEW, $\tau = 8.0$s, $M_i = 1.32$, $t = 1.08$ms.

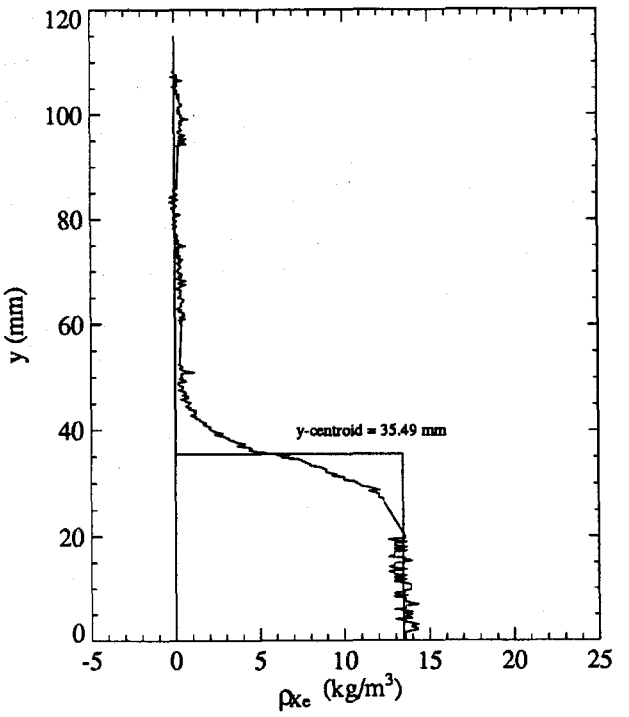

Fig.4.2.1 Determination of the Centroid of a Density Profile. Run #0547, CEW, $\tau = 8.0$s, $M_i = 1.32$, $t = 1.08$ms. $x = 17.1$ mm.

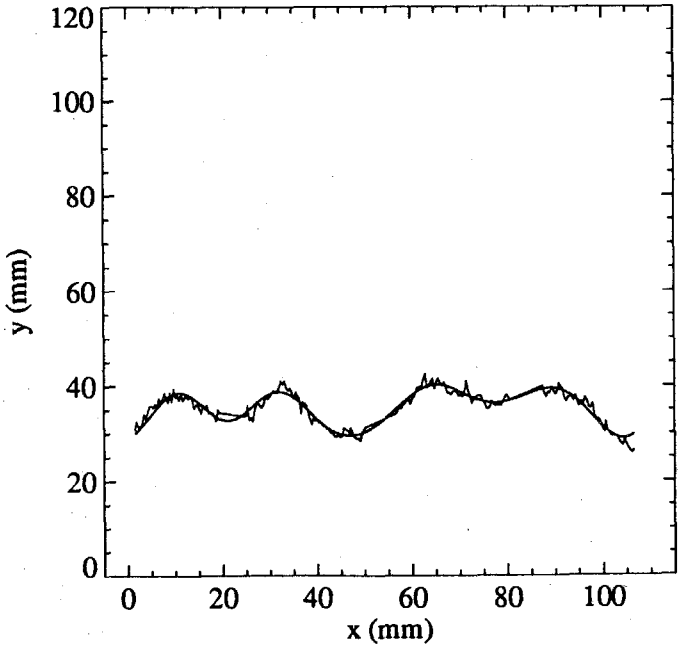

Fig.4.2.2 Mean Interface Shape. Run #0516, CEW, $\tau = 1.2$s, $M_i = 1.32$, $t = 5.85$ms.

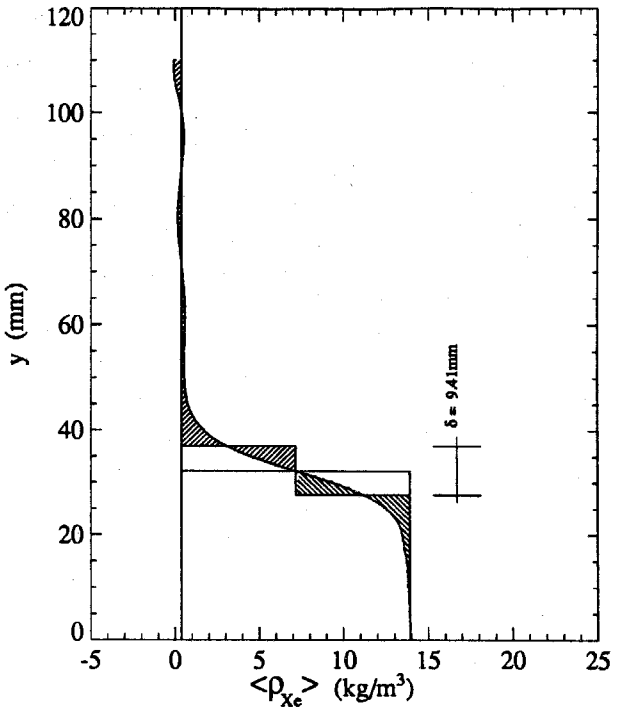

Fig.4.2.3 Average Density Profile and Interface Thickness. Run #0547, CEW, τ = 8.0s, M_i = 1.32, t = 1.08ms.x_l = 0, x_r = 105.

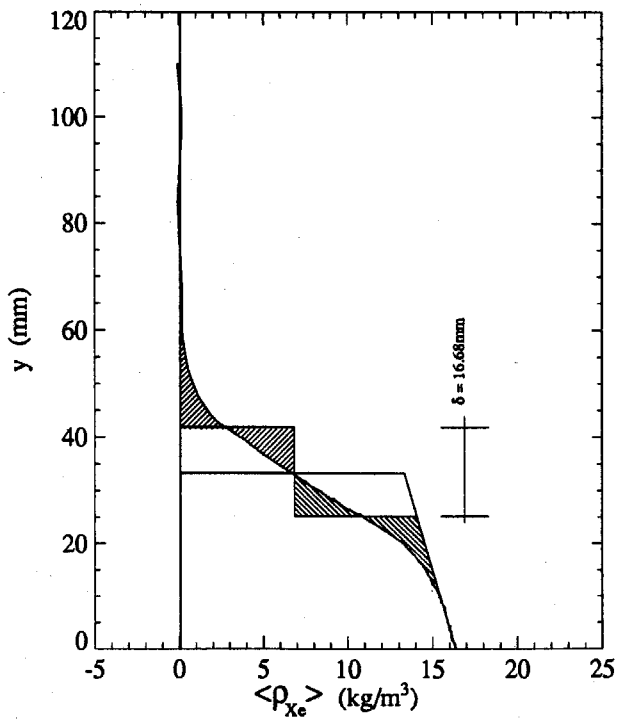

Fig.4.2.4 Average Density Profile and Interface Thickness for Oblique Xenon Density Asymptote. Run #0533, CEW, τ = 1.2s, M_i = 1.32, t = 5.57ms.x_l = 0, x_r = 105.

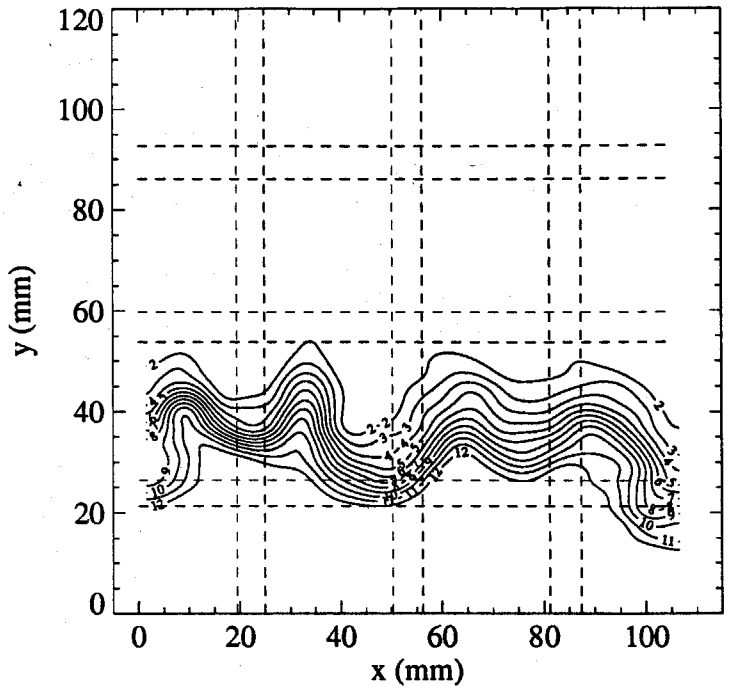

Fig.4.2.5 Density Contours Generated from Filtered Two-Dimensional Density Field. Run #0516, CEW, $\tau = 1.2$s, $M_i = 1.32$, $t = 5.85$ms.

CHAPTER 5

SINGLY AND DOUBLY SHOCKED INTERFACES

5.1 Introduction

This chapter describes and discusses the results of experiments in which only the incident shock wave, or the incident and one reflected shock, interact with the air/xenon interface. Initially distorted and nominally flat interfaces are studied, and their behavior is compared.

In both cases the Mach number of the incident wave is $M_i = 1.32$. The close end wall configuration permits the study of singly shocked interfaces at times from 0 to about 0.65 ms after interaction with the incident shock, while the far end wall configuration allows the imaging of interfaces from about 3 to about 4 ms after the same interaction. Furthermore, the near and far end wall configurations permit the study of interfaces from 0.0 to 0.5 ms and from 0.5 to 3.0 ms after interaction with the shock reflected from the end wall, respectively. Figures 5.1.1 and 5.1.2 show the $y-t$ diagrams for the two cases: The origins of the y and t axes coincide with the initial position of the interface and the arrival of the incident shock, respectively. The two dashed, vertical lines represent the edges of the test section window. The incident shock sets the interface in motion toward the bottom of the shock tube. The Mach number of the shock transmitted in the xenon is $M_t = 1.44$, while that of the shock reflected in the air is $M_{r0} = 1.10$. The transmitted shock reflects from end wall of the shock tube with Mach number $M_{r1} = 1.36$, intercepts the downward moving interface at time t_c and, since the xenon is denser than the air, a shock is transmitted and a rarefaction is reflected; the interface is set in an upward motion. The rarefaction reaches the bottom of the shock tube, reflects and catches up with the upward moving interface t_e; it is reflected as a compression wave and transmitted as a rarefaction. These reverberations continue in time following the same pattern. Table 5.1.1 shows the values of the interaction times for the close and far end wall geometries, and the interface position above the end wall at the time of interaction with the reflected shock and the reflected expansion, respectively. Table

5.1.2 shows the values of the interface speed, and of the density, speed of sound and acoustic impedance of air and xenon upon interaction with the incident and reflected shocks, and reflected expansion. All the data presented in these two tables are calculated using one dimensional gasdynamics.

Table 5.1.1. Interaction Times and Interface Positions for M_i =1 .32, Air/Xe Interface.

Geometry	t_c (ms)	Int. Pos. (mm)	t_e (ms)	Int. Pos. (mm)
CEW	0.64	49	1.20	70
FEW	4.30	289	7.00	389

Table 5.1.1. Relevant Parameters for M_i =1 .32, Air/Xe Interface.

	Preshock	Shock	Reshock	Expansion
u (m/s)	0	98 ↓	37 ↑	12 ↓
ρ_{Air} (kg/m^3)	1.21	2.19	3.06	2.65
a_{Air} (m/s)	340	389	416	405
$(\rho a)_{Air}$ kg/m^{2}s	411	852	1273	1073
ρ_{Xe} (kg/m^3)	5.46	8.90	11.65	10.18
a_{Xe} (m/s)	176	211	233	227
$(\rho a)_{Xe}$ kg/m^{2}s	960	1878	2715	2311
$\frac{(\rho a)_{Xe}}{(\rho a)_{Air}}$	2.33	2.22	2.13	2.15
A	0.637	0.605	0.584	0.587

In the close end wall configuration, the interface is initially located within the test section, 2 cm below the top edge of the windows, and 11 cm from the shock tube end wall. In the time interval $0 < t < t_c$ we obtain one image of the interface at $t \approx 0.30$ ms. In the far end wall configuration, the initial distance between the interface and the end wall is 71 cm. It takes the interface about 3 ms to propagate to the test section, so no image is obtained before $t = 3.0$ ms; the reflected shock reaches the interface about 4.5 ms after the interaction with the incident one, and there is a 2.5 ms time window to image the reshocked interface, before $t_e = 7.0$ ms, when the first reflected rarefaction arrives at it.

5.2 Single Scale Interfaces

As described in Sec. 3.3, the interface distorted with a nominally quasi-single-scale perturbation is generated by letting 1.2 s elapse between the completion of plate retraction and shock arrival at the interface.

5.2.1 Incident Shock

Figure 5.2.1 is the image of the optical density field of an X-ray negative exposed 0.26 ms after the incident shock has interacted with the air-xenon interface. The digital image is composed of 8-bit pixels, whose value thus ranges between 0 and 255, corresponding to 100 times the local value of the grey level of the film ($D \times 100$). The gray scale used here (shown to the side of the test section) has been stretched to enhance the contrast of the negative, by representing the minimum value of the optical density in the negative ($D = 0.55$, pixel value 55, in the xenon region) by $D = 0$ and the maximum value ($D = 1.65$, pixel value 165, in the air region) by $D = 2.55$. The grid pattern in the picture is the shadow of the aluminum stiffening structure. From top to bottom one can see shocked air (light gray, near white, indicating large D values, large exposure, low X-ray absorption), the interface (the steep transition from the light to the dark gray), shocked xenon (dark gray, indicating small D, small exposure, large X-ray absorption), the transmitted shock wave (the sharp discontinuity between dark and medium gray), and unshocked xenon (medium gray, indicating medium D, medium exposure, medium X-ray absorption). The interface looks essentially flat; no distortions can be detected by visual inspection of the image. However, as image processing of this image and the subsequent development of the interface will show, perturbations of finite amplitude, and wavelength between 27.5 mm and 110 mm

(the first four modes) are present. The transmitted shock wave also appears undistorted. Figure 5.2.2 shows the mean interface shape, calculated from the density data as described in Sec. 4.2, (noisy line), and its reconstruction using only the first six modes and no windowing (smooth line). The individual plots of these first six components are collected in Fig. 5.2.3. Mode 1 dominates all the others with an amplitude of about 0.75 mm. Figure 5.2.4 shows the average density profile for the run. The top, center and bottom portions of the curve (essentially vertical) represent the air, shocked and unshocked xenon fields respectively. The portion of the curve joining the top and middle regions represents the interface, while that joining the middle and bottom regions represents the shock wave. The fact that the shock wave does not look like a perfectly horizontal segment in the density profile is a consequence of averaging over a total of about 220 density profiles, following the procedure described in Sec. 4.2. The interface thickness measured from the average density profile is about 7 mm.

Figure 5.2.5 shows the optical density of a radiograph taken 3.82 ms after the initial shock-interface interaction; the mean interface shape is shown in Fig. 5.2.6. At this time the perturbations on the interface are more evident; two crests and three troughs are distinguishable. The interface thickness measured from the average density profile is about 11 mm. Thus, the thickness has changed only slightly in the time interval between the two runs, *i.e.* 3.58 ms. The slope of the interface at the right wall of the test section in Fig. 5.2.5 is due to the shear stress in the viscous boundary layer behind the transmitted shock.

5.2.2 Reflected Shock

Interface distortion becomes more visible after interaction with the reflected shock. Figure 5.2.8 is an image of the optical density of an X-ray photo taken 5.38 ms after the arrival of the incident shock and only 1.13 ms after interaction with the reflected shock. The mean interface shape is shown in Fig. 5.2.9. The reflected wave induces a negative growth rate on the interface (since the Atwood number at the interface is negative in this case). Thus, upon interaction with the reflected wave, the perturbation amplitude decreases, until flattening of the interface, the crests become the troughs and viceversa, and the perturbations grow at the same rate that led to the flattening. At $t = 5.38$ ms the interface exhibits disturbances whose amplitude is comparable with their wavelength.

Two large vortices are visible at the walls, where the reflected shock wave has interacted with the boundary layers generated by the incident wave. This is also visible from the

density contours, shown in Fig. 5.2.10. The average density profile across the interface is shown in Fig. 5.2.11.

A radiograph taken 6.68 ms after the arrival of the first shock (2.43 ms after interaction with the reflected one) is presented in Fig. 5.2.12. The structures appearing most different from the previous image are the wall vortices: The roll-up which was clearly visible in Fig. 5.2.8 is no longer clear. The size of the core of the vortices has increased by about 50%. The crest at the middle of the interface has tilted toward the right, and it has distorted into a mushroom-like shape. The interface mean shape is presented in Fig. 5.2.13, density contours in Fig. 5.2.14, and the average density profile in Fig. 5.2.15. This latter is obtained following the procedure described in Sec. 4.2, but restricting the averaging to the region between the wall vortices. This restriction is applied to all the density profiles for photographs where the wall vortices occupy a large fraction of the interface. The mean interface shape looks less distorted at $t = 6.68$ ms than it does at $t = 5.31$ ms. To explain this, one must remember that the definition of mean interface shape is an integral one (see Sec. 4.2). Therefore the line in Fig. 5.2.13 is an average between the shapes of the highly distorted, uppermost layers of the interface (where the xenon density is minimum) and the lower, less distorted portions (where the xenon density is largest). Actually, this smoothing effect is observed, to a greater or lesser extent, in all of the plots of interface shape. The wall vortices also play an important role, as will be discussed in a separate section at the end of this chapter.

Figure 5.2.16 is a collection of reconstructed mean interfaces for 10 runs; the lines are located where the interface actually is within the test section. The most distorted are the mean shapes of the interfaces imaged just after interaction with the reflected shock. At later times the smoothing effect of the integral definition makes the mean shapes look less perturbed. Figure 5.2.17 shows the time behavior of the first six modes on the interface; the incident shock strikes the interface at $t = 0$ ms. The reflected shock arrives at the interface at $t = 4.25$ ms, and is indicated in the plots by the first vertical line. Mode 1 is the only one exhibiting some growth before the arrival of the reflected shock. The passage of the reshock induces a negative growth rate (since the Atwood number is negative for a shock going from the heavy into the light gas). Because of this, the mode amplitudes decrease to zero (interface flattening) and then grow with a reversed phase (the crests become the

troughs and viceversa). To avoid plotting a negative mode amplitude (unphysical), the point of zero crossing is deduced by the data and represented by an open circle, and the post-shock growth rates are measured between the point of zero crossing and the next value of the mode amplitude. For the reflected shock, the only useful data are those from the first radiograph after the interaction with the reshock. Data from later photographs are adversely affected by the flattening described above, and for this reason are represented with open symbols in the plots.

Modes 5 and 6 show virtually no growth and their amplitude is at all times smaller than that of the first 4 modes. The amplitudes of the higher modes are not presented in the plots, since they are consistently smaller than those of the lower order modes.

Table 5.2.1 summarizes the growth rates of the first four modes, due to the incident and the reflected shocks, along with the values calculated from the theory (Eq. 2.3.6); the initial values of the amplitude used in the calculations are the measured ones. After the incident shock, the Atwood number is 0.61 and the measured interface thickness is about 7 mm; thus the values of the growth reduction factor, ψ are between 1.15 and 1.25 for wavelengths between 110 mm and 27.5 mm (see Fig. 2.2.3, where all the Atwood numbers are for pre-shock conditions). After the reshock the Atwood number becomes 0.58 and the interface thickness starts at a value of about 7 mm; the values for ψ are larger than for the singly shocked interface (between 1.25 and 2.53). From Eq. 2.3.6 one sees that the growth rate depends on the wave number directly and through ψ. Now, $\psi(k) \approx \xi k$ with $\xi < 1$, and therefore the net effect on the growth rate is that it becomes larger as k increases. The other important parameter is the initial amplitude of the perturbations: The large difference between the growth rates of the first and the higher modes, after the reshock, is to a great extent due to the fact that the post-reshock amplitude measured for the first mode is between 3 and 4.5 times that of the others.

The distortions measured after the first shock are actually too small to allow for a comparison with the theory. The comparison holds more significance after interaction with the reflected shock, (at least until the mean interface flattening due to averaging starts to occur).

Brouillette (1989) found growth rates of 2.13 m/s and 5.45 m/s for an air/SF_6 interface upon interaction with the incident and the reflected shock, respectively (M_i = 1.32). To

explain the large differences from the present results, two facts must be considered: First, Brouillette's imaging was with the schlieren method which, as will be discussed in the next chapter, produces photographs with different details than the radiographs discussed here. The perturbation amplitude read from the prints took into account the mushroom shape of the interface whereas, in the present experiments, the mode amplitude is measured from the mean interface shape, in which the mushroom distortions are smoothed over. Secondly, in Brouillette's case no modal decomposition was possible and the amplitude was measured from the superposition of all waves; here the amplitude of each wavelength is studied separately.

Table 5.2.1 Growth Rates of the First 4 Modes. Far End Wall Configuration. $M_i = 1.32$

Mode	$\frac{d\eta}{dt}$ (m/s)					
	Incident Shock			Reflected Shock		
	$t_1 - t_2$ (ms)	measured	calculated	$t_1 - t_2$ (ms)	measured	calculated
1	0.0 - 4.25	0.19	2.08	4.89 - 5.38	2.31	3.25
2	0.0 - 4.25	0.04	1.09	4.50 - 5.38	1.32	0.56
3	0.0 - 4.25	0.07	1.57	4.56 - 5.38	2.24	1.19
4	0.0 - 4.25	0.01	1.82	4.44 - 5.38	1.91	1.42

A discussion of the behavior of the interface thickness in time is delayed to Sec. 5.5.1, after a detailed discussion of the effects of the wall vortices is given and a correction algorithm is proposed (Sec. 5.4).

5.3 Multiscale Interfaces

For these interfaces the growth rate of short wavelength disturbances is large (see Eq. 2.3.3). On the other hand, their initial amplitude is very small and the thickness to wavelength ratio is large, yielding a large value of the growth reduction factor, ψ, for the interface, both of which tend to make the growth rate small. The net result is that the interface thickens rather slowly. It looks essentially flat throughout the process (except for

the distortions induced on its edges by the wall effects), and its thickness increases with time, in a manner similar to that for the single scale interfaces.

5.3.1 Incident Shock

Figure 5.3.1 is the image of the optical density of an X-ray plate exposed 0.32 ms after shock arrival at the interface. The transmitted shock is also visible in the figure. The interface shape and the average density profile are shown in Fig. 5.3.2 and Fig. 5.3.3, respectively. All perturbations are just at the noise level; the interface thickness is about 10 mm.

The optical density of a radiograph taken at 3.82 ms is shown in Fig. 5.3.4, and the interface shape in Fig. 5.3.5. From this latter and from the density contours, shown in Fig. 5.3.6, no clear crest or trough can be distinguished on the interface. The single scale interface in Fig. 5.2.5, imaged at the same time, after being accelerated by a shock wave of the same strength, already exhibits two clear 'humps' on its upper surface. In the present case, the interface thickness is again about 10 mm, indicating that, also for the multiscale interface, the growth induced by the first shock cannot be observed over a time of about 4 ms.

5.3.2 Reflected Shock

An image of the reshocked interface, taken at $t = 5.82$ ms is shown in Fig. 5.3.8. The interface shape, the density contours, and the average density profile are shown in Figs. 5.3.9 through 5.3.11. The only distortions on the interface are apparently those due to the wall vortices, visible in both the optical density image and the density contours. The slight concavity in the middle of the upper layers of the interface is due to the strain induced by the images of the wall vortices (sketched in Fig. 5.3.12).

Figure 5.3.13 is a radiograph taken at $t = 6.69$ ms. Again the only deformations on the interface are those due to the wall vortices, as can also be seen from the density contours (Fig. 5.3.15). Figure 5.3.16 shows the density profile for the interface, obtained with the same caveats to the standard procedure described for that of Fig. 5.2.15. A thorough discussion of the shape of this profile, and of the effects that the wall vortices have on it, is presented in the next section.

Figure 5.3.17 shows the mean interface shape at the times of the various snapshots; the distortion that develops is due to the wall vortices both at the walls, where they cause the interface to 'hump', and at the middle where the strain they induce causes a concavity in the interface (best seen in Fig. 5.3.15). The same considerations made earlier on for the single scale interfaces (*viz.* that the mean interface is the result of an average between the highly distorted top layers and the less distorted bottom ones) holds in the present case as well, although the difference in shape between the top and bottom of the interface is smaller.

The time evolution of the mode amplitudes shown in Fig. 5.3.18 must therefore be understood in the same sense: The disturbances are localized at the walls, where the Richtmyer-Meshkov instability due to the interaction of the reflected shock with the boundary layer left behind the incident wave amplifies the local interface distortion, generating the wall vortices. Once these have developed (by, say, $t \approx 5.80$ ms) their effect on the interface dominates that of shock-induced amplitude growth and therefore the theory used in the previous section cannot be used here for comparison with the measurements.

As for the single scale interfaces, the evolution of the interface thickness will be discussed after treatment of the effect of the wall vortices.

5.4 Effects of the Wall Vortices

The cross sections of the wall vortices are visible in many of the photographs presented in this chapter. Although not easily visible from the images, the same vortices also develop on the front and back windows of the shock tube, as sketched in Figs. 5.4.1 and 5.4.2. Thus, a region of essentially pure xenon, at the center of the shock tube, is surrounded by a vortex tube, whose composition is a mixture of air and low density xenon. To describe how X-ray absorption is affected by this flow pattern, it is useful to recall Lambert's law (Eq. 4.1.3) and the definition of optical depth (Eq. 4.1.4). Here, since absorption by the air is always neglected, it is assumed that the absorption coefficient σ is simply that of pure xenon. In the present case, three optical depths are relevant: That of the vortex tubes aligned with the X-ray tube axis (whose cross section is clearly visible in the photographs), for which ρ is low and l is large (the full side of the test section); that of the pure xenon in the region surrounded by the vortex tubes, for which ρ is high and l is moderate; and that of the

vortex tubes on the windows, for which both ρ and l are small. Being the result of an integrated average of X-ray absorption across the whole test section, the central portions of the radiograph show the sum of the effects of the latter two optical depths. This is easily seen in the density contours in Fig. 5.3.15; the central region, delimited by the wall vortices at the sides, and by the steep concentration of density lines at the top and bottom, actually represents the fact that pure xenon only occupies a fraction of the shock tube cross section there. The average density profile of Fig. 5.3.16 is in direct correspondence with the contours, and shows a first increase through the real interface, then a region of nearly constant values (the central region of the contour plot), and finally another increase across the bottom portion of the vortex tubes. The point made here is that the interface thickness determined from this density profile is too large. A corrected profile is needed, representing only the density of the xenon in the region surrounded by the wall vortices, as depicted in Fig. 5.4.2.

At a fixed y-location in the air above the interface, the value of the optical depth is small and essentially constant in x; similarly, at a y-location in the xenon field, the value is large and constant in x. At a fixed y-location within the wall vortices, the optical depth changes with x, being lowest at the sides (where it is entirely due to the wall vortices) and highest in the middle (where it is due to the wall vortices and the xenon between them), as depicted in Fig. 5.4.3. Two average values of optical depth can be constructed, one over the whole width of the field of view, $\overline{d}$, the other only across its central portion, $\overline{d_c}$ (away from the wall vortices). Now, if the wall vortices were only at the side walls and not on the front and back walls, the optical depth distribution would be the same at the sides but higher in the middle, since the whole depth of the test section would be filled with xenon. The proposed correction consists of constructing a new optical depth distribution, such that its overall average is the same as the average over the central portion of the uncorrected distribution. This is accomplished by multiplying the optical depth by the ratio $\overline{d_c}/\overline{d}$. This makes the value of the corrected distribution at any x-location higher than the corresponding value of the uncorrected distribution, the difference being larger in the middle than at the sides. The average over the central portion of this corrected distribution is thus larger than the corresponding average for the uncorrected distribution. The central portion of the optical depth field is that from which the average density profile is evaluated. Nothing guarantees that the central portion of this new distribution is the ideal one (without wall vortices), since

it is not possible to decouple the optical depth of the wall vortices from that of the xenon between them and estimate what the xenon optical depth is. This operation is repeated at all y-locations, with the correcting factor changing with y from a value of 1 in the xenon field, through values larger than 1 in the wall vortices region, and back to 1 in the air region. As an example of the application of this algorithm, Fig. 5.4.4 shows the corrected average density profile corresponding to the uncorrected one shown in Fig. 5.3.16. The plateau in the central portion of the profile has in large part disappeared, and the density increases almost continuously from the top to the bottom of the profile. Yet, the profile exhibits an 'uncertain' behavior in its middle region, indicating that the correction does not solve the problem entirely.

5.5 Interface Thickness

5.5.1 Single Scale Interfaces

Figure 5.5.1 is a plot of the interface thickness, measured from the averaged density profiles, versus time. The two vertical lines indicate the arrival of the reshock and of the reflected expansion. The triangles indicate data deduced from the uncorrected profiles, while the diamonds represent values measured from the corrected ones. The circle indicates data measured in the close end wall configuration, immediately after interaction with the reshock (not feasible in the far end wall configuration); it is shown in the plots at the same delay from the reshock at which it was measured. Solid symbols represent data measured from average density profiles on which the effect of the wall vortices was small; the open symbols indicate that the effect of the wall vortices on the average density profiles was non-negligible (possibly even after applying the correction algorithm). A linear least squares fit is made to the pre-shock data, and one to the post-shock data from the corrected density profiles (but not using the data point represented by the circle, since it actually belongs to a different configuration).

Virtually no growth is detected until the reflected shock arrives at the interface. The linear interpolation through the post-shock data indicates a growth rate of about 7 m/s. Trying to model this growth with Eq. 2.4.2, and looking for the simplest possible form, *viz.*

$$\delta = \beta A'[v]t \tag{5.5.1}$$

the present data yield

$$\beta = 0.09 . \tag{5.5.2}$$

These data are a new contribution to the subject, in that the experiments are the first ones that measure the thickness of an interface with large wavelength perturbations. The idea of vertically shifting each density profile to follow the mean interface shape (as discussed in Sec. 4.2) is also new.

5.5.2 Multiscale Interfaces

Figure 5.5.2 is a plot of the interface thickness *vs.* time; the meaning of the symbols is the same as discussed in the previous section. As in the case of the single scale interfaces, no growth occurs after passage of the first shock. A linear least squares fit through the post-reshock data from corrected density profiles shows a growth rate of about 4 m/s. Modeling the growth with Eq. 5.5.1, the multiplicative constant is found to be

$$\beta = 0.05 . \tag{5.5.3}$$

The thickness growth rate for the multiscale interfaces is thus about one half of that of the single scale ones.

In his schlieren visualization experiments with air/SF_6, multiscale interfaces, accelerated by the same $M_i = 1.32$ incident shock, Brouillette (1989) measured a post-reshock thickness growth rate of 1.1 m/s; the multiplicative constant β thus was $\beta = 0.01$. It is important to note the differences between the measuring techniques used in the two cases. First, a schlieren imaging system adjusted to very high sensitivity generates inherently thicker interfaces than the X-ray imaging, since its signal is proportional to density gradients, regardless of the value of the density itself. Secondly, the thickness extracted from the present data is based upon the integral definition of Eq. 4.2.3, which produces smaller values than those obtained by measuring the height of the dark region in a schlieren photograph with a ruler. These systematic deviations in the thickness apparently are not reflected in the growth rates, which show the opposite effect. On the other hand, even the corrected density profiles yield overestimated thickness values. The net effect is that both thickness values and growth rates are larger in the present results than in those of Brouillette. This discrepancy remains an unresolved issue.

Table 5.5.1 summarizes the thickness growth rates from the present results and those of Brouillette (1989).

Table 5.5.1 Thickness Growth Rates. Far End Wall Configuration. $M_i = 1.32$

τ (s)	Present		Brouillette (1989)	
	$\frac{d\delta}{dt}$ (m/s)	β	$\frac{d\delta}{dt}$ (m/s)	β
1.2	6.77	0.09	NA	NA
8.0	3.64	0.05	1.1	0.01

All of the above considerations about the wall vortices point out the need for different experimental techniques, capable of 2-D imaging in a selected plane. In this way, measurements would no longer be integrated averages but rather localized to a fixed value of the third dimension. Typical examples of these techniques are planar laser induced fluorescence and planar Rayleigh scattering.

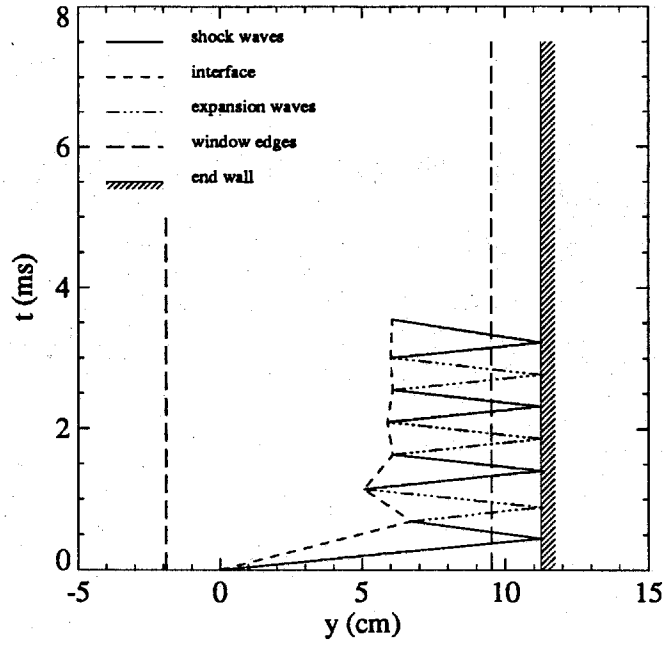

Fig.5.1.1 $y-t$ Diagram for the Close End Wall Configuration ($M_i = 1.32$).

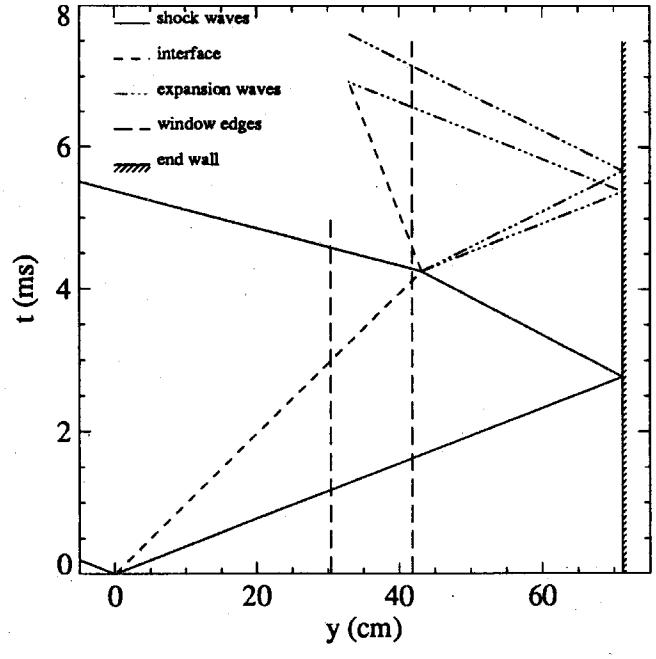

Fig.5.1.2 $y-t$ Diagram for the Far End Wall Configuration ($M_i = 1.32$).

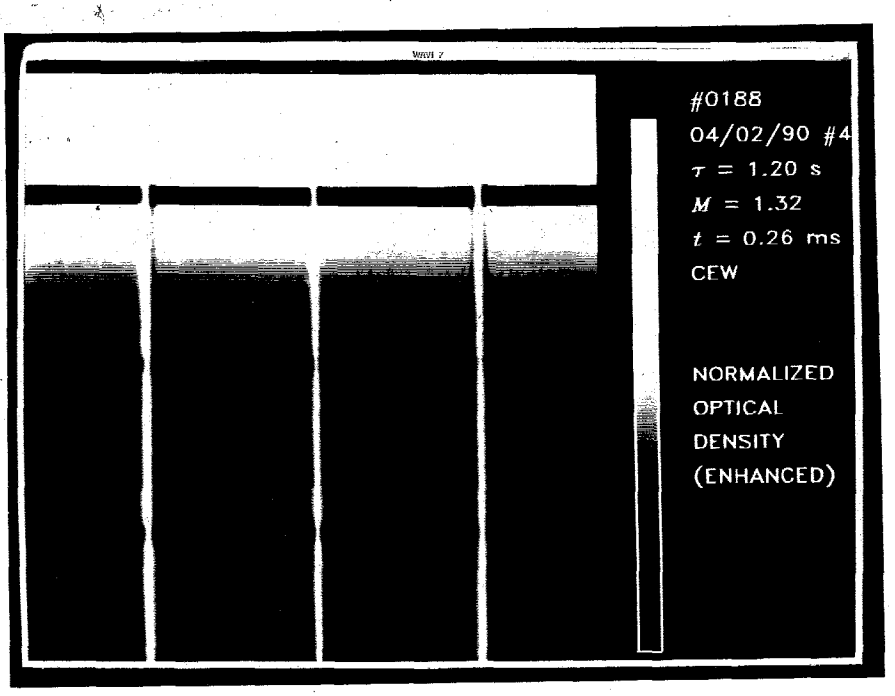

Fig.5.2.1 Air/Xenon. Run #0188. CEW. $\tau = 1.2$ s; $M_i = 1.32$; $t = 0.26$ ms. Optical Density of the Radiograph.

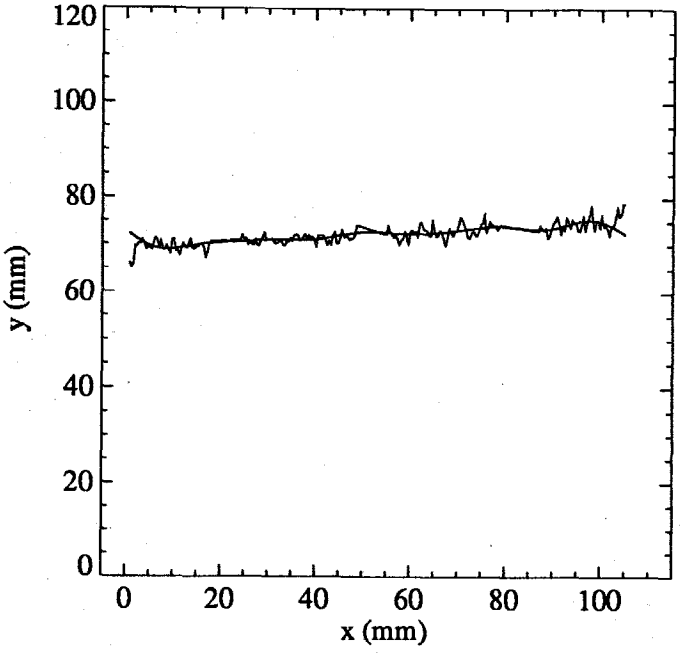

Fig.5.2.2 Run #0188. CEW. $\tau = 1.2$ s; $M_i = 1.32$; $t = 0.26$ ms. Mean Interface Shape.

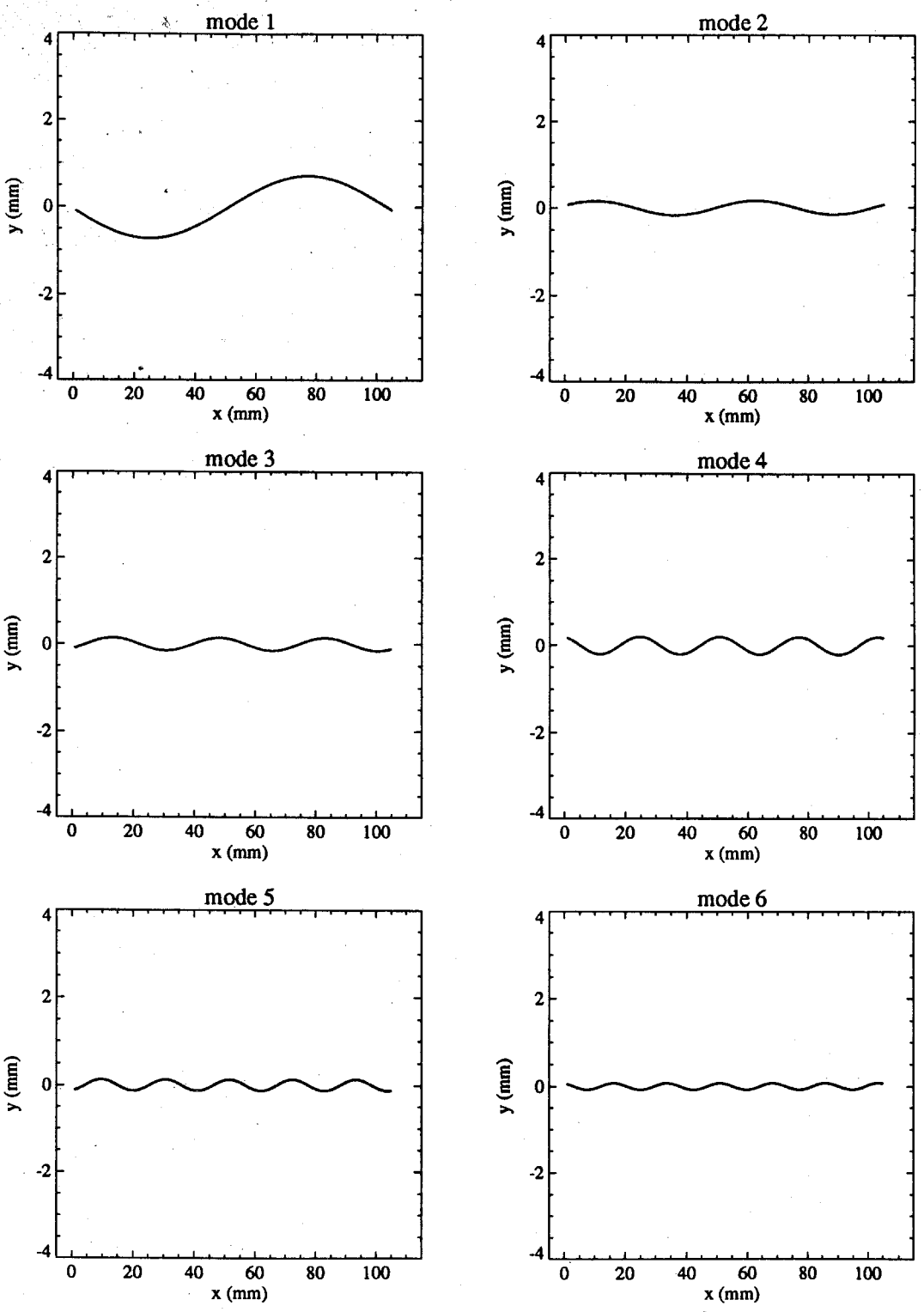

Fig.5.2.3 Run #0188. CEW. τ = 1.2 s; M_i = 1.32; t = 0.26 ms. First Six Components of the Mean Interface Shape.

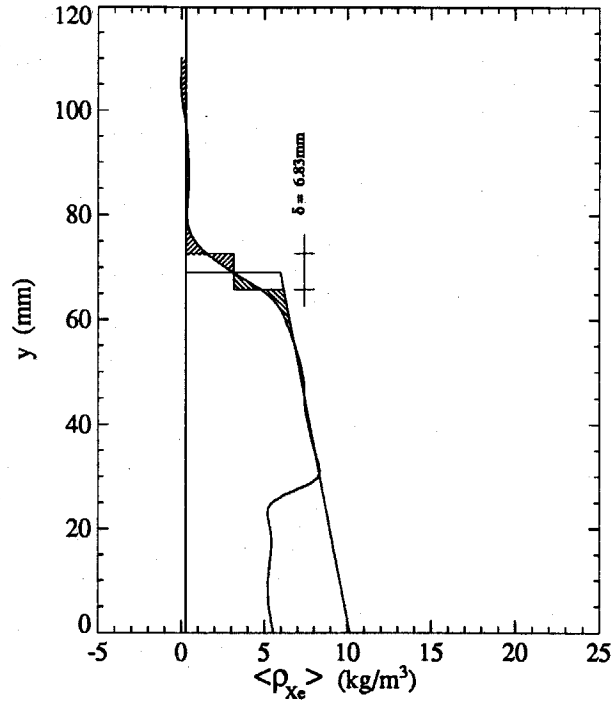

Fig.5.2.4 Run #0188. CEW. $\tau = 1.2$ s; $M_i = 1.32$; $t = 0.26$ ms. Average Density Profile. $x_l = 0$, $x_r = 105$.

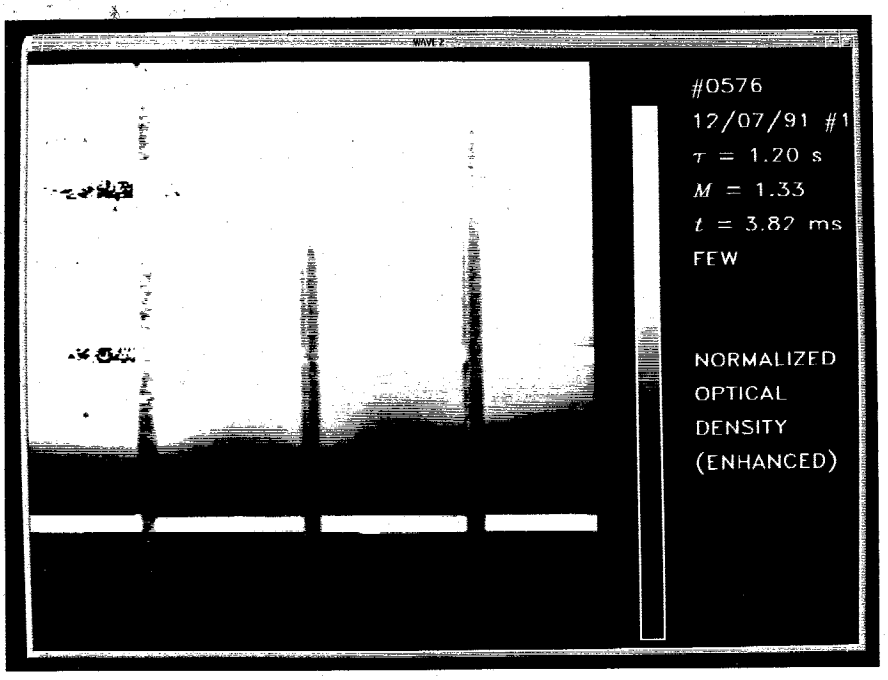

Fig.5.2.5 Air/Xenon. Run #0576. FEW. $\tau = 1.2$ s; $M_i = 1.32$; $t = 3.84$ ms. Optical Density of the Radiograph.

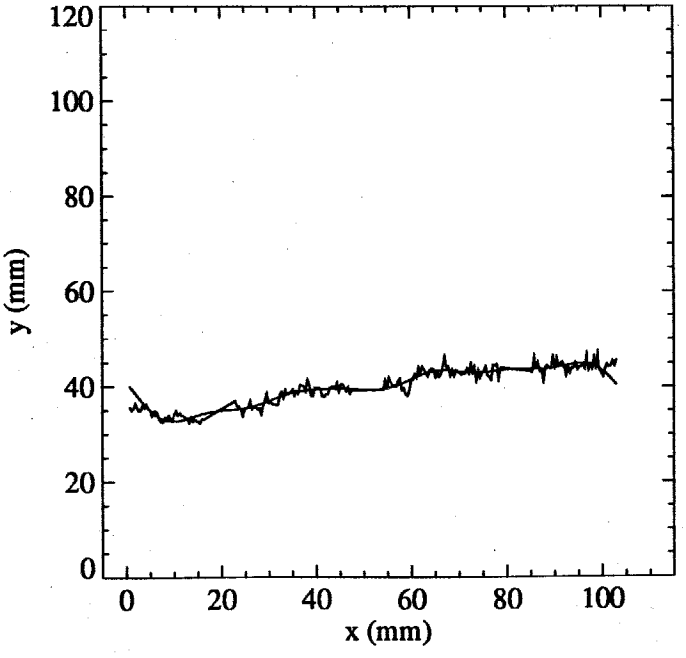

Fig.5.2.6 Run #0576. FEW. $\tau = 1.2$ s; $M_i = 1.32$; $t = 3.84$ ms. Mean Interface Shape.

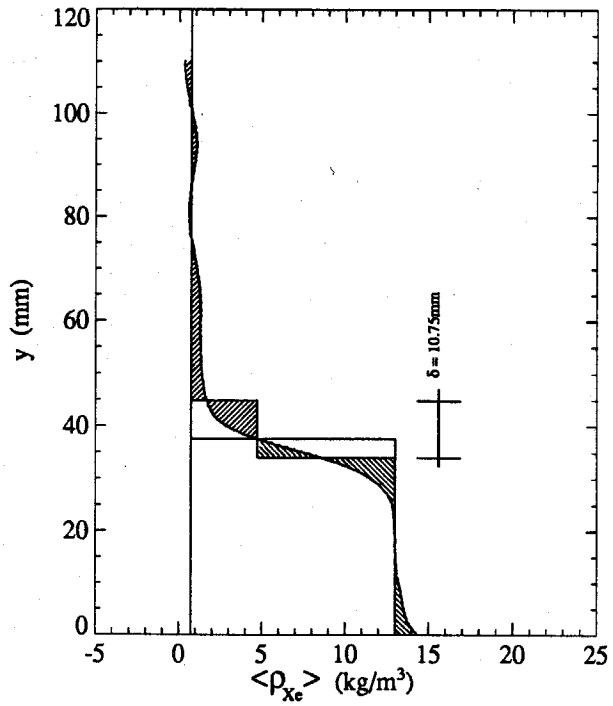

Fig.5.2.7 Run #0576. FEW. $\tau = 1.2$ s; $M_i = 1.32$; $t = 3.84$ ms. Average Density Profile. $x_l = 0$, $x_r = 105$.

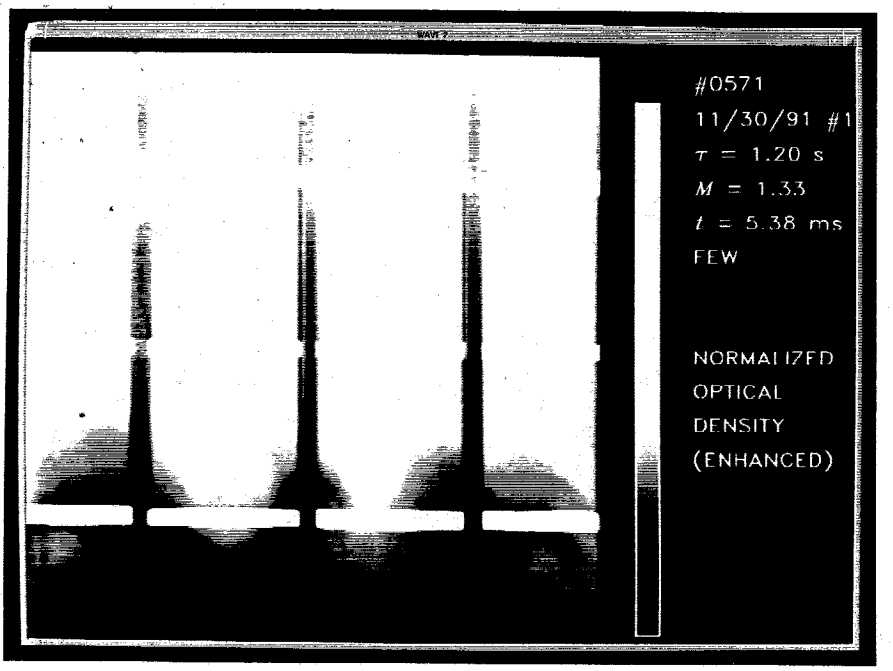

Fig.5.2.8 Air/Xenon. Run #0571. FEW. $\tau = 1.2$ s; $M_i = 1.32$; $t = 5.38$ ms. Optical Density of the Radiograph.

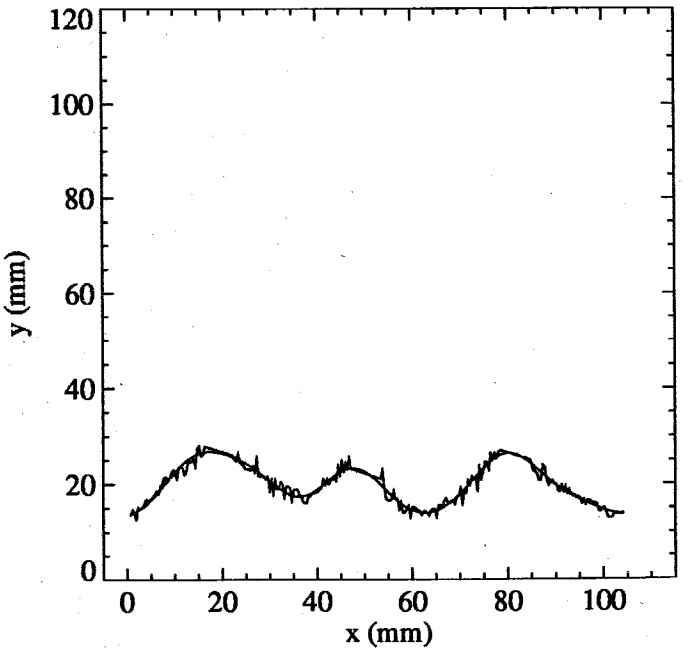

Fig.5.2.9 Run #0571. FEW. $\tau = 1.2$ s; $M_i = 1.32$; $t = 5.38$ ms. Mean Interface Shape.

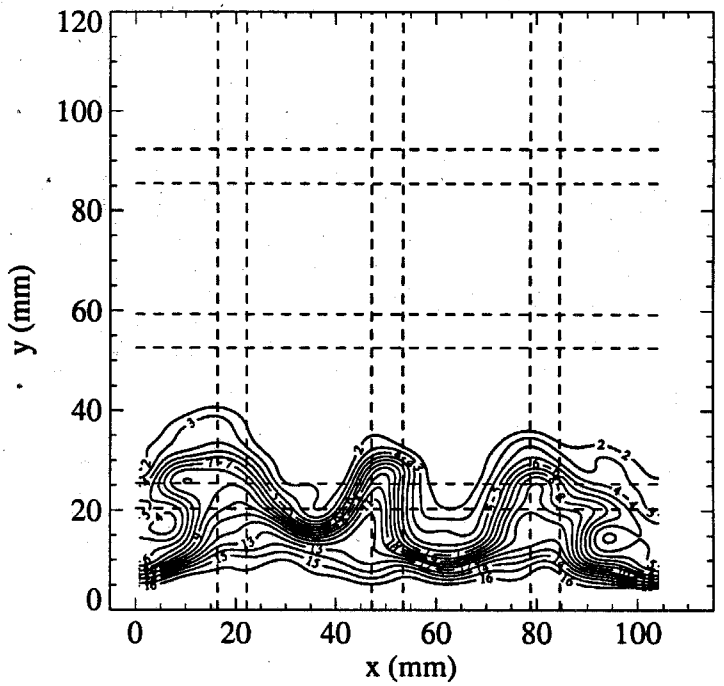

Fig.5.2.10 Run #0571. FEW. τ = 1.2 s; M_i = 1.32; t = 5.38 ms. Density Contours.

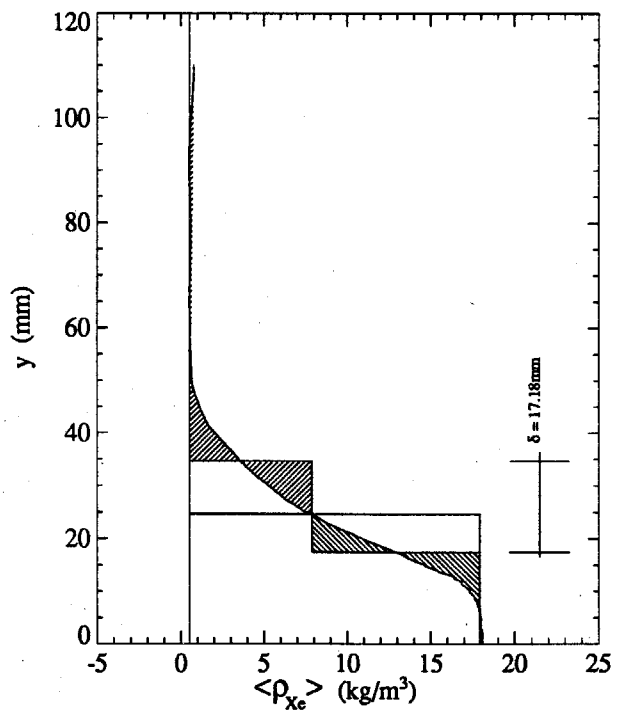

Fig.5.2.11 Run #0571. FEW. τ = 1.2 s; M_i = 1.32; t = 5.38 ms. Average Density Profile. x_l = 23, x_r = 78.

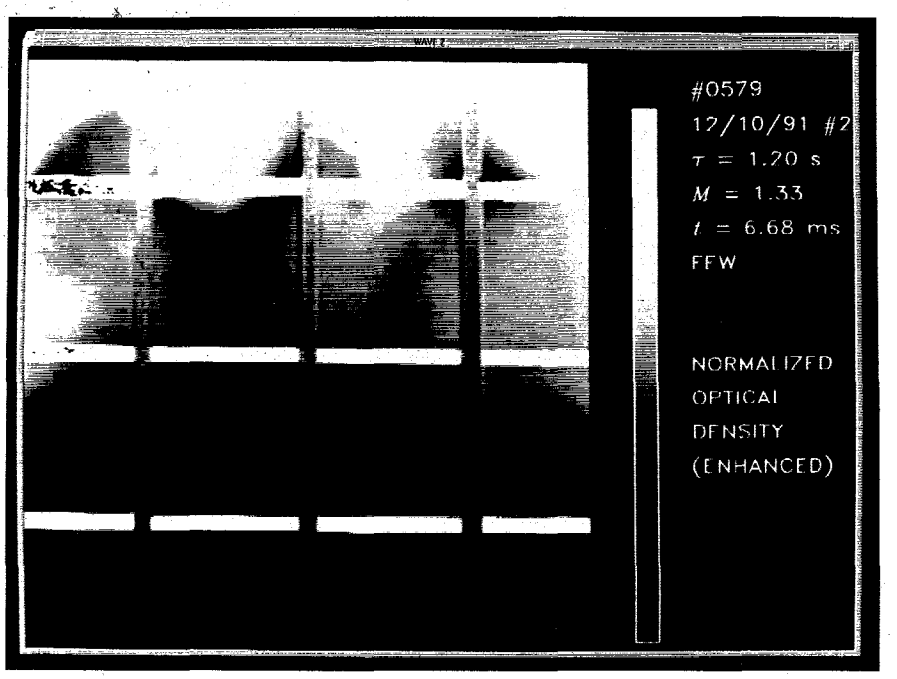

Fig.5.2.12 Air/Xenon. Run #0579. FEW. $\tau = 1.2$ s; $M_i = 1.32$; $t = 6.68$ ms. Optical Density of the Radiograph.

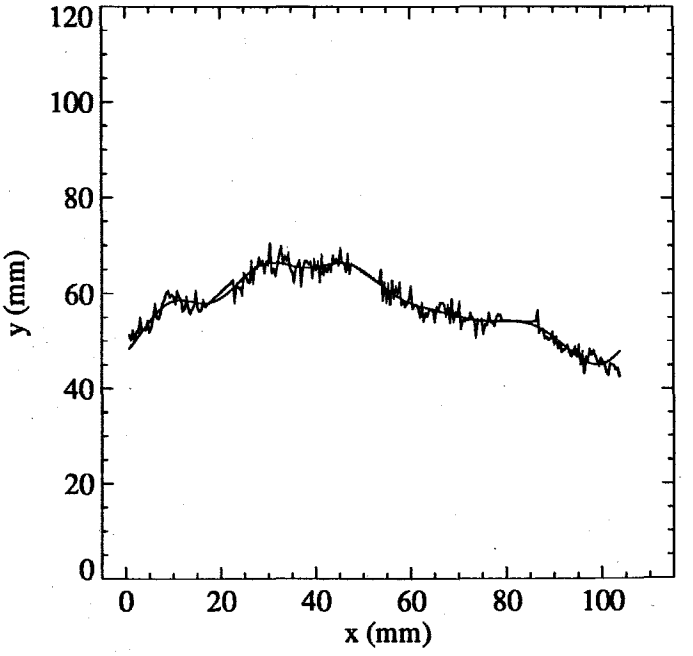

Fig.5.2.13 Run #0579. FEW. $\tau = 1.2$ s; $M_i = 1.32$; $t = 6.68$ ms. Mean Interface Shape.

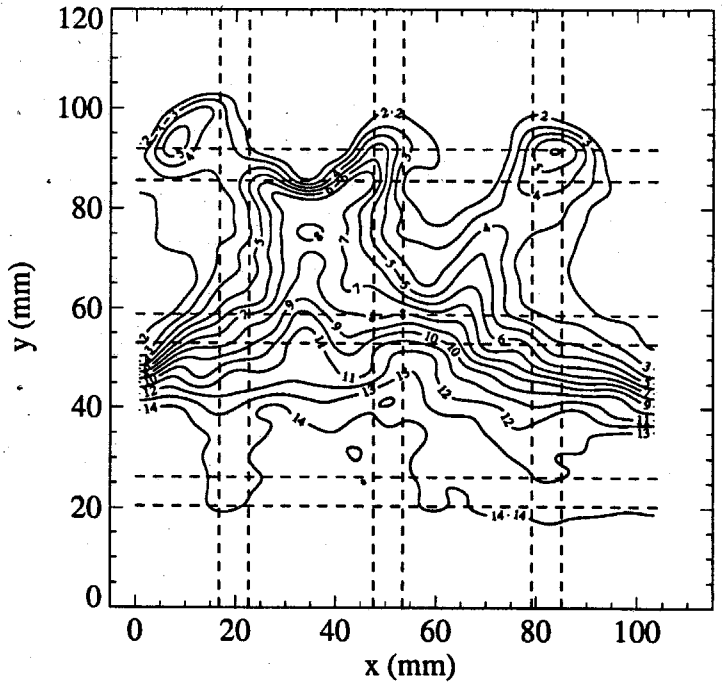

Fig.5.2.14 Run #0579. FEW. τ = 1.2 s; M_i = 1.32; t = 6.68 ms. Density Contours.

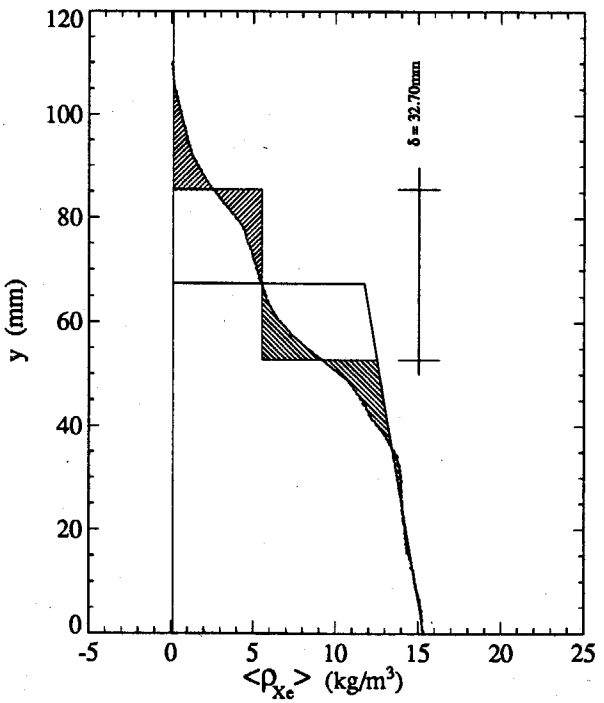

Fig.5.2.15 Run #0579. FEW. τ = 1.2 s; M_i = 1.32; t = 6.68 ms. Average density Profile. x_l = 30, x_r = 70.

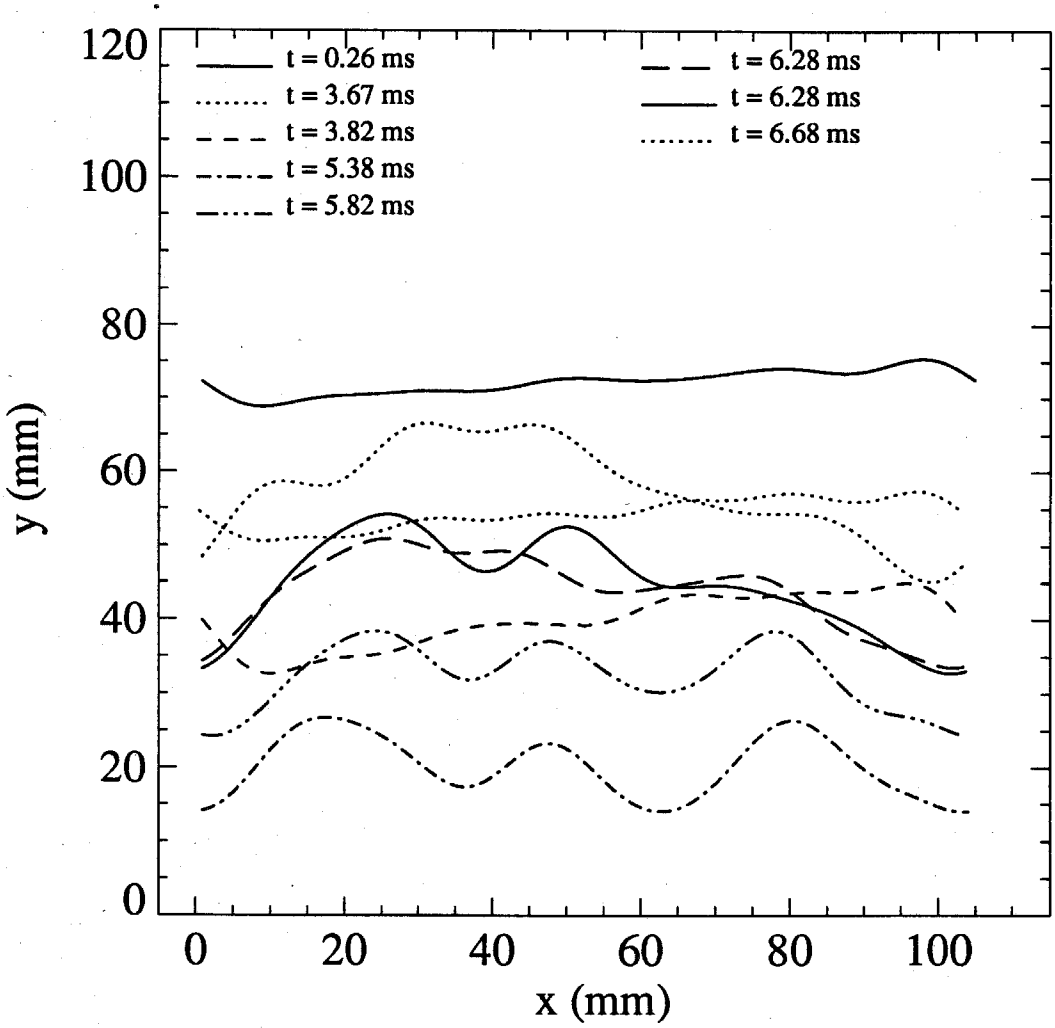

Fig.5.2.16 Far End Wall Configuration. τ = 1.2 s; M_i = 1.32; t = 6.68 ms. Mean Interface Shape at Various Times.

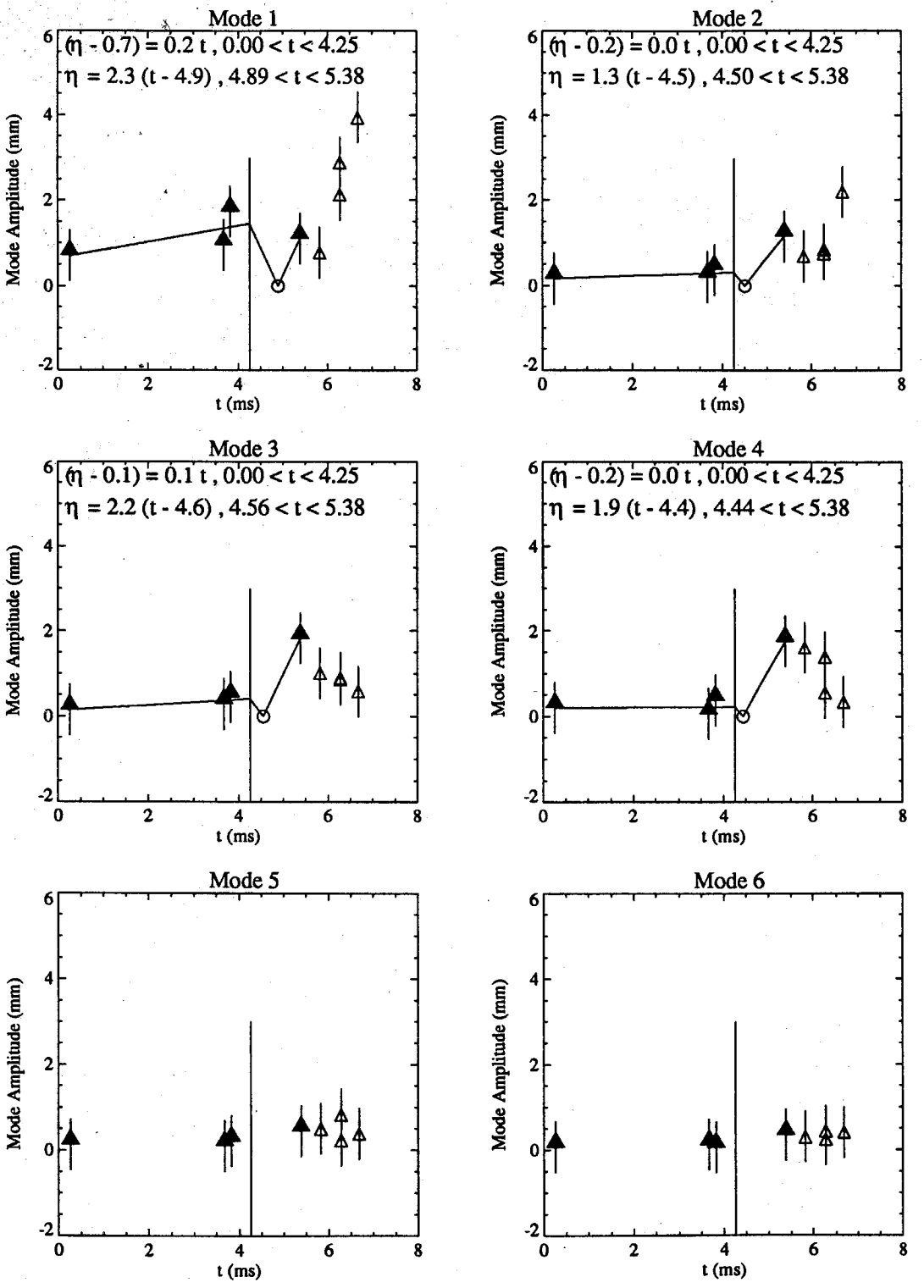

Fig.5.2.17 Far End Wall Configuration. τ = 1.2 s; M_i = 1.32. Amplitude of the First Six Modes *vs.* Time.

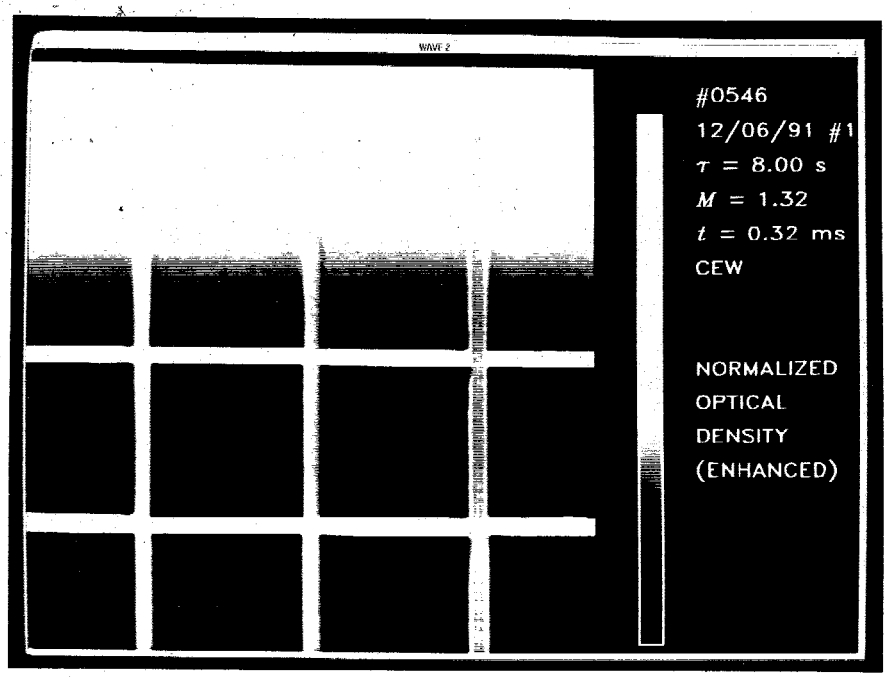

Fig.5.3.1 Air/Xenon. Run #0546. CEW. $\tau = 8.0$ s; $M_i = 1.32$; $t = 0.32$ ms. Optical Density of the Radiograph.

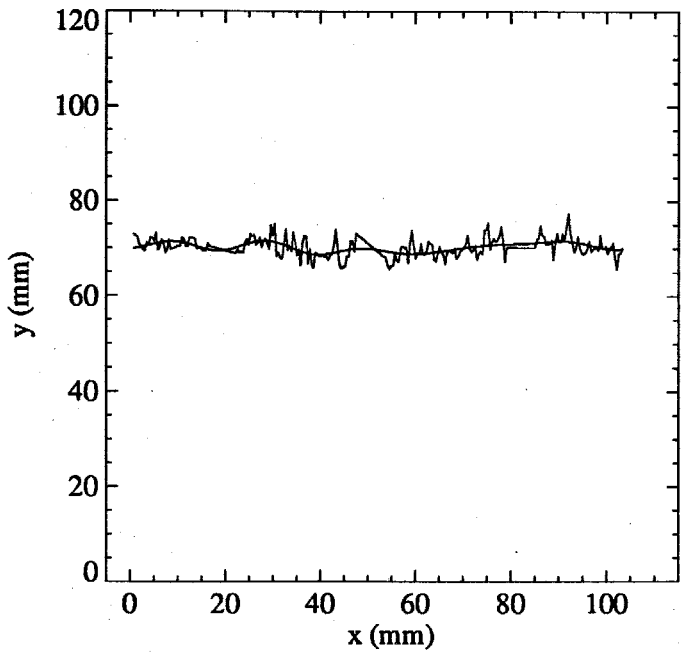

Fig.5.3.2 Run #0546. CEW. $\tau = 8.0$ s; $M_i = 1.32$; $t = 0.32$ ms. Mean Interface Shape.

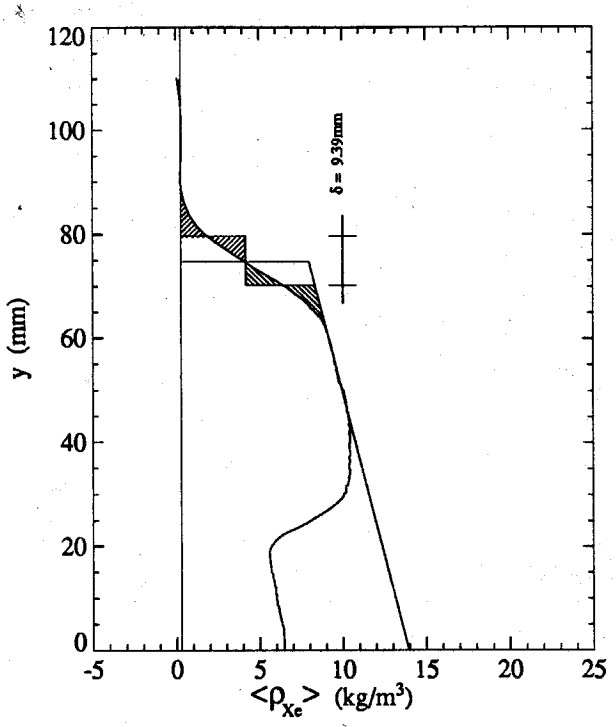

Fig.5.3.3 Run #0546. CEW. τ = 8.0 s; M_i = 1.32; t = 0.32 ms. Average density Profile. $x_l = 0$, $x_r = 105$.

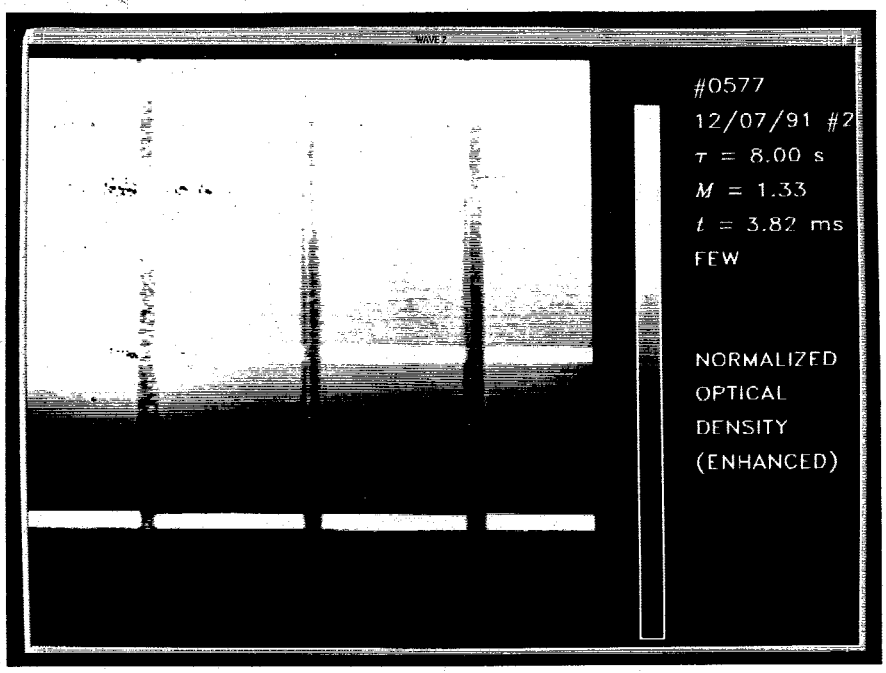

Fig.5.3.4 Air/Xenon. Run #0577. FEW. τ = 8.0 s; M_i = 1.32; t = 3.82 ms. Optical Density of the Radiograph.

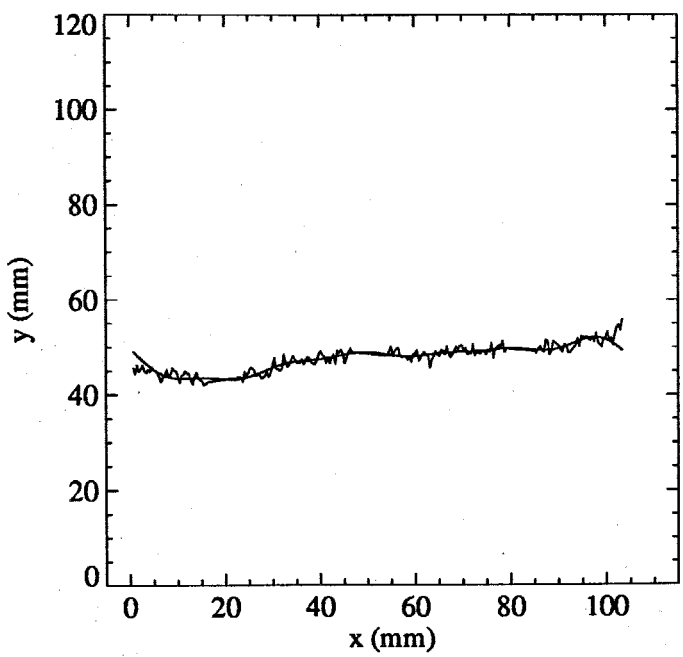

Fig.5.3.5 Run #0577. FEW. τ = 8.0 s; M_i = 1.32; t = 3.82 ms. Mean Interface Shape.

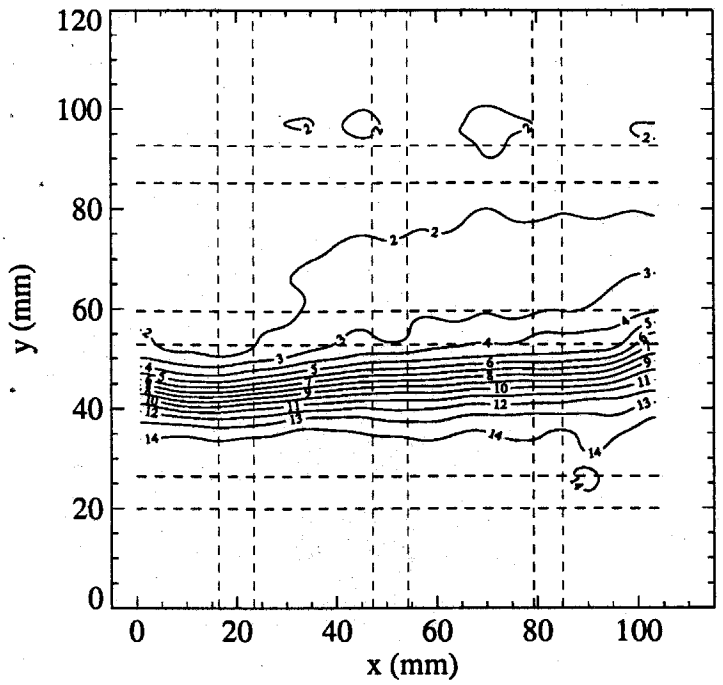

Fig.5.3.6 Run #0577. FEW. τ = 8.0 s; M_i = 1.32; t = 3.82 ms. Density Contours.

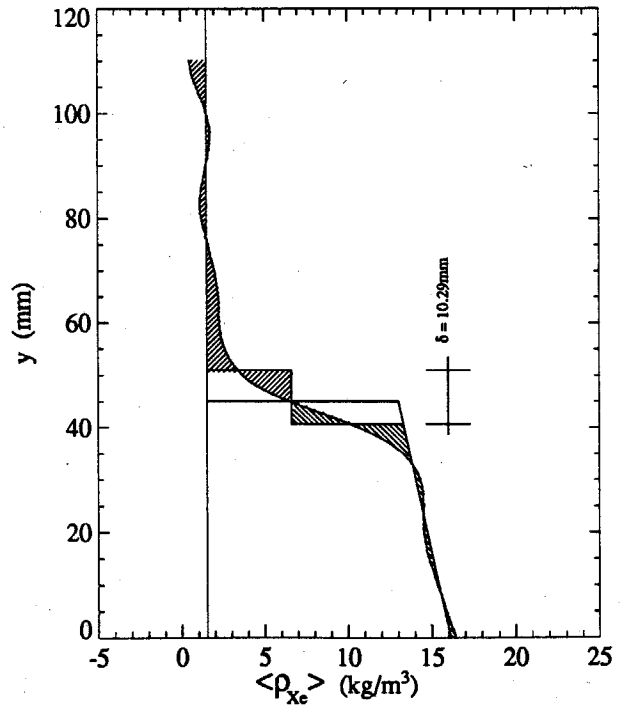

Fig.5.3.7 Run #0577. FEW. τ = 8.0 s; M_i = 1.32; t = 3.82 ms. Average density Profile. x_l = 0, x_r = 105.

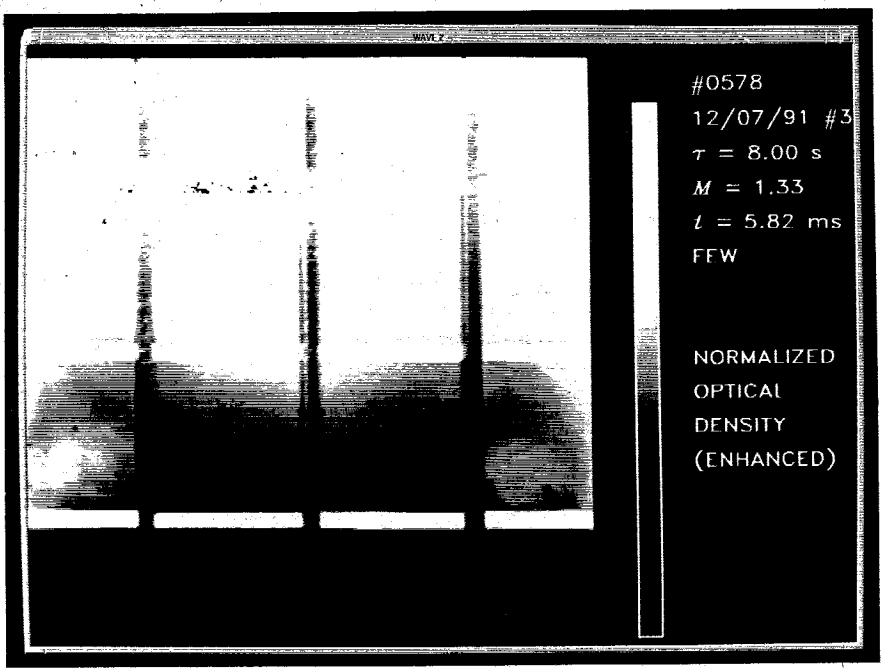

Fig.5.3.8 Air/Xenon. Run #0578. FEW. τ = 8.0 s; M_i = 1.32; t = 5.82 ms. Optical Density of the Radiograph.

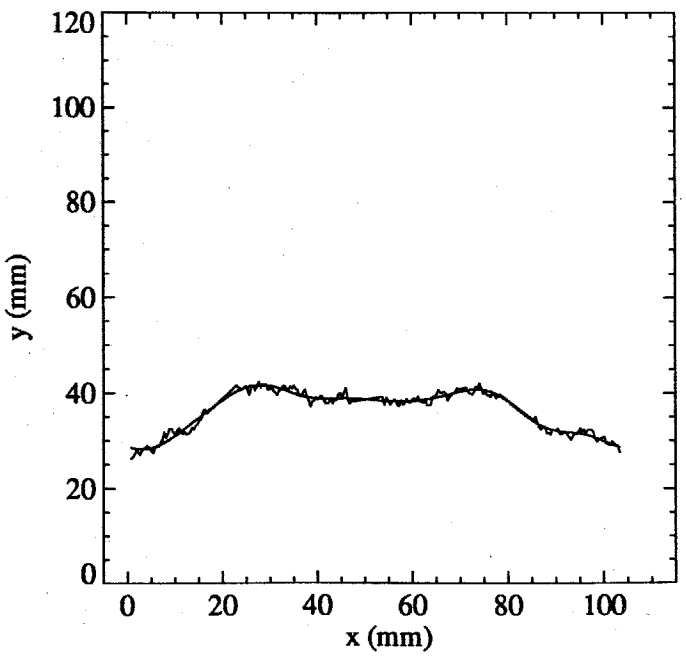

Fig.5.3.9 Run #0578. FEW. τ = 8.0 s; M_i = 1.32; t = 5.82 ms. Mean Interface Shape.

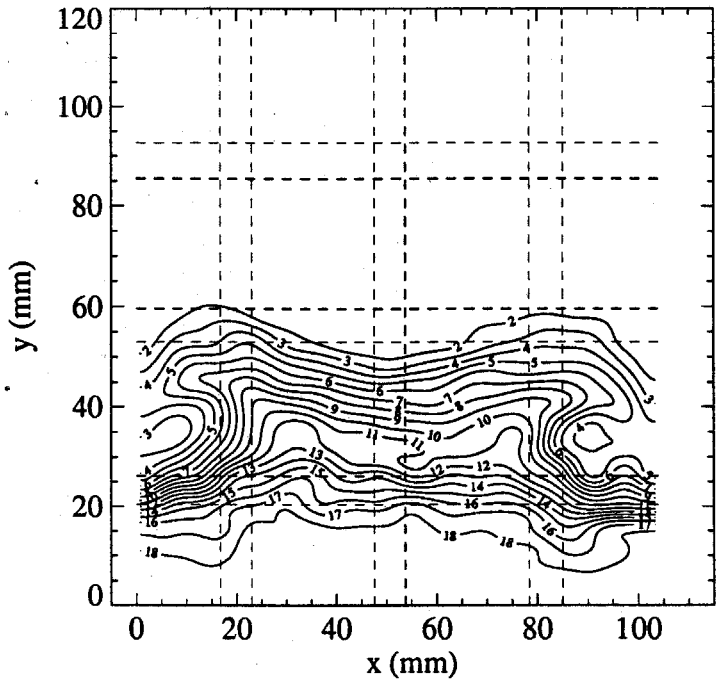

Fig.5.3.10 Run #0578. FEW. τ = 8.0 s; M_i = 1.32; t = 5.82 ms. Density Contours.

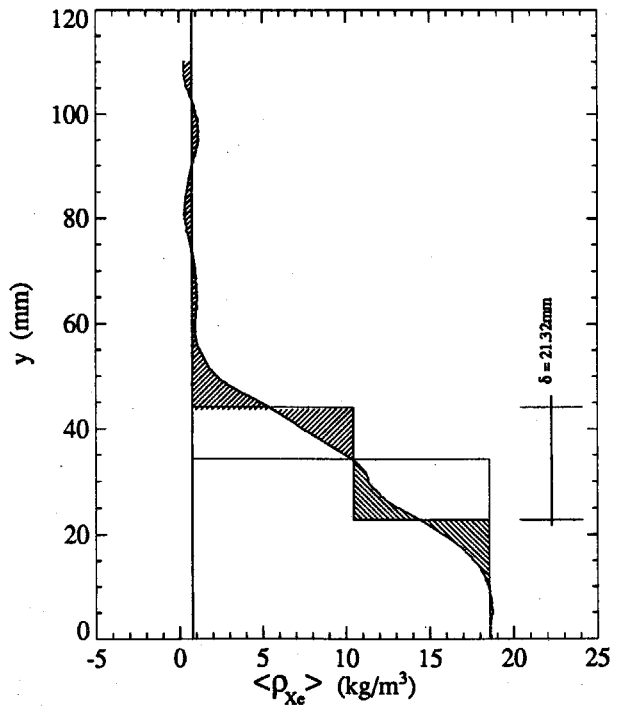

Fig.5.3.11 Run #0578. FEW. τ = 8.0 s; M_i = 1.32; t = 5.82 ms. Average density Profile. x_l = 30, x_r = 70.

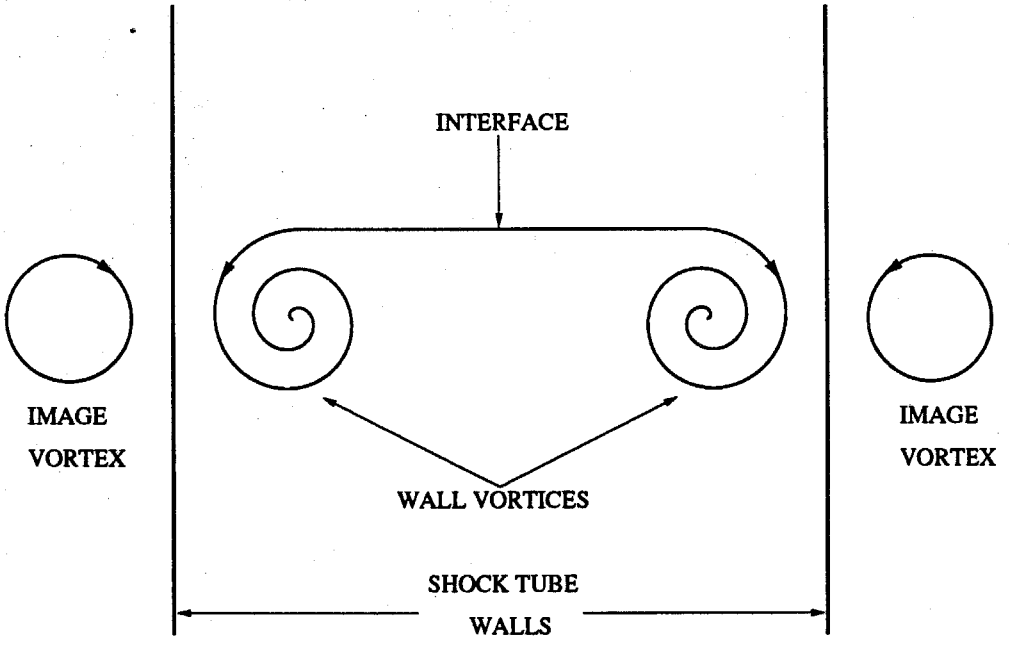

Fig.5.3.12 Schematic of the Images of the Wall Vortices.

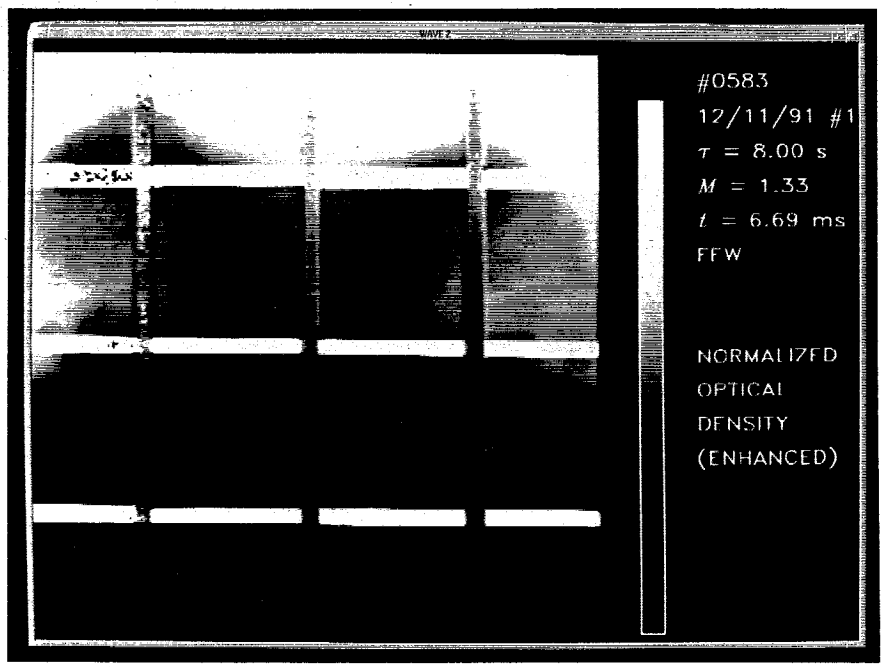

Fig.5.3.13 Air/Xenon. Run #0583. FEW. $\tau = 8.0$ s; $M_i = 1.32$; $t = 6.69$ ms. Optical Density of the Radiograph.

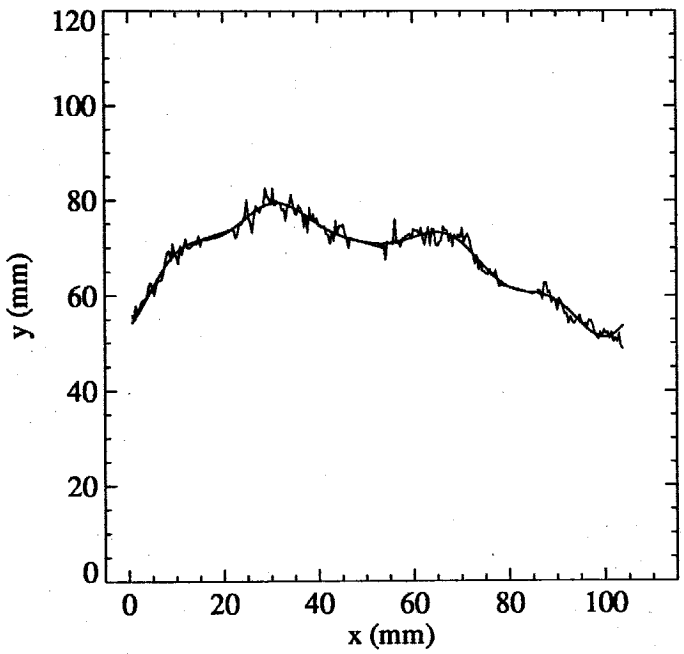

Fig.5.3.14 Run #0583. FEW. $\tau = 8.0$ s; $M_i = 1.32$; $t = 6.69$ ms. Mean Interface Shape.

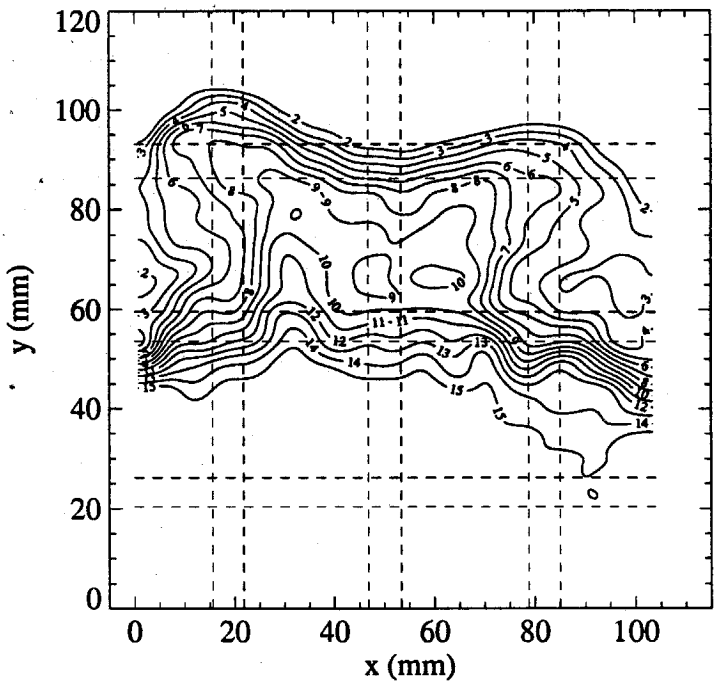

Fig.5.3.15 Run #0583. FEW. τ = 8.0 s; M_i = 1.32; t = 6.69 ms. Density Contours.

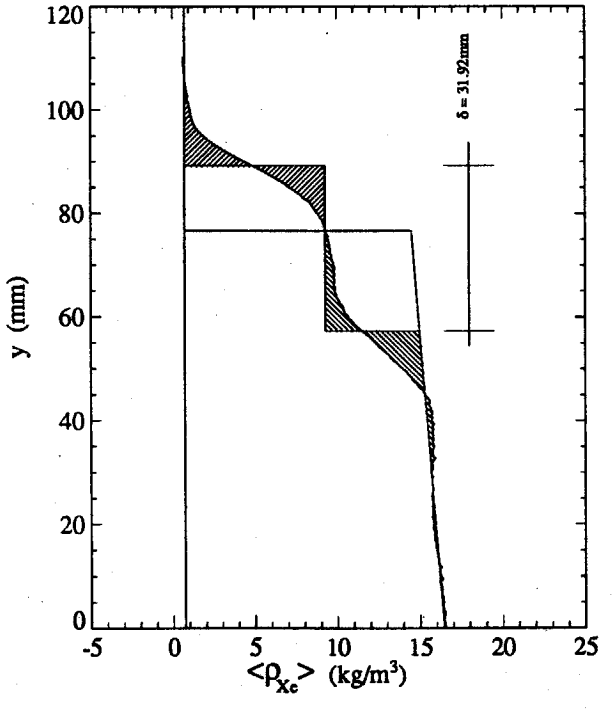

Fig.5.3.16 Run #0583. FEW. τ = 8.0 s; M_i = 1.32; t = 6.69 ms. Average density Profile. x_l = 30, x_r = 65.

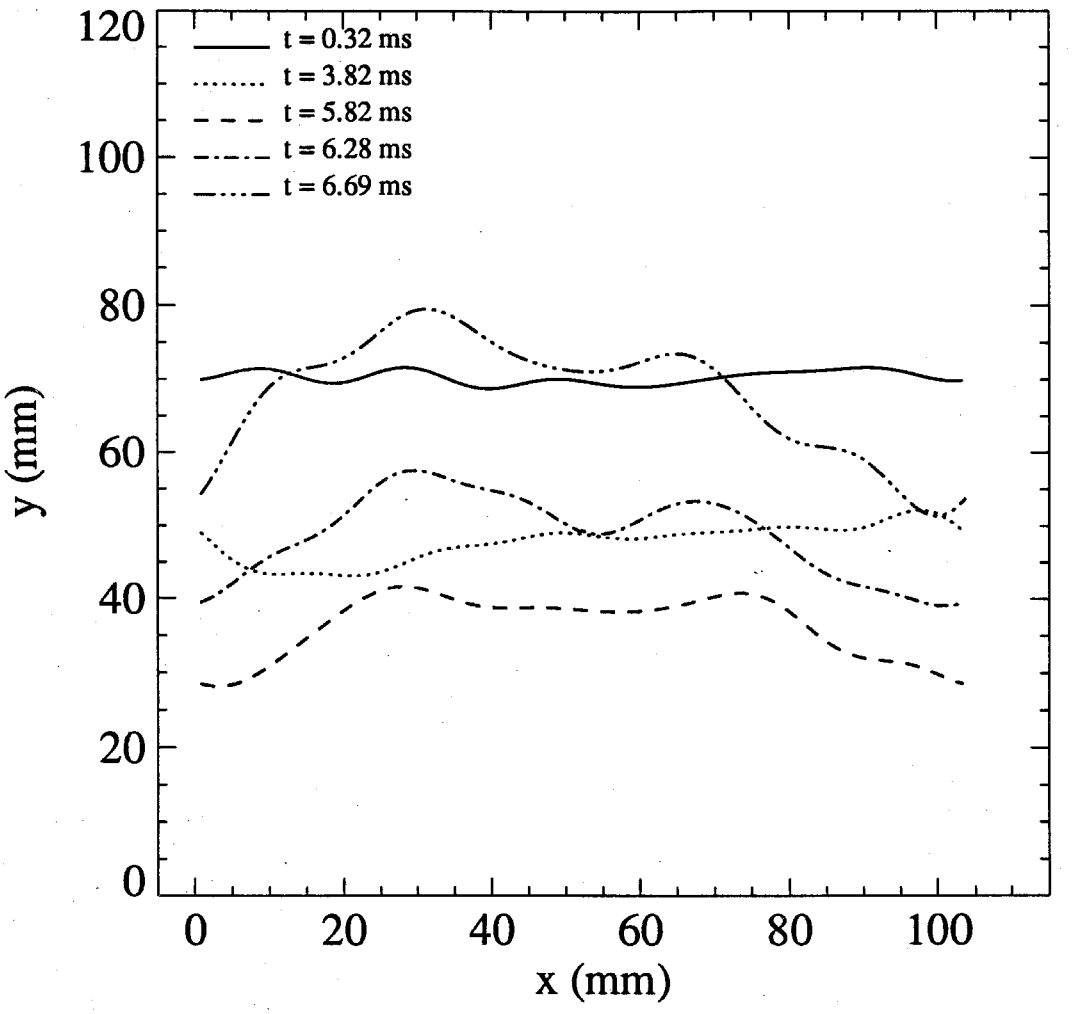

Fig.5.3.17 Far End Wall Configuration. τ = 8.0 s; M_i = 1.32. Mean Interface Shape at Different Times.

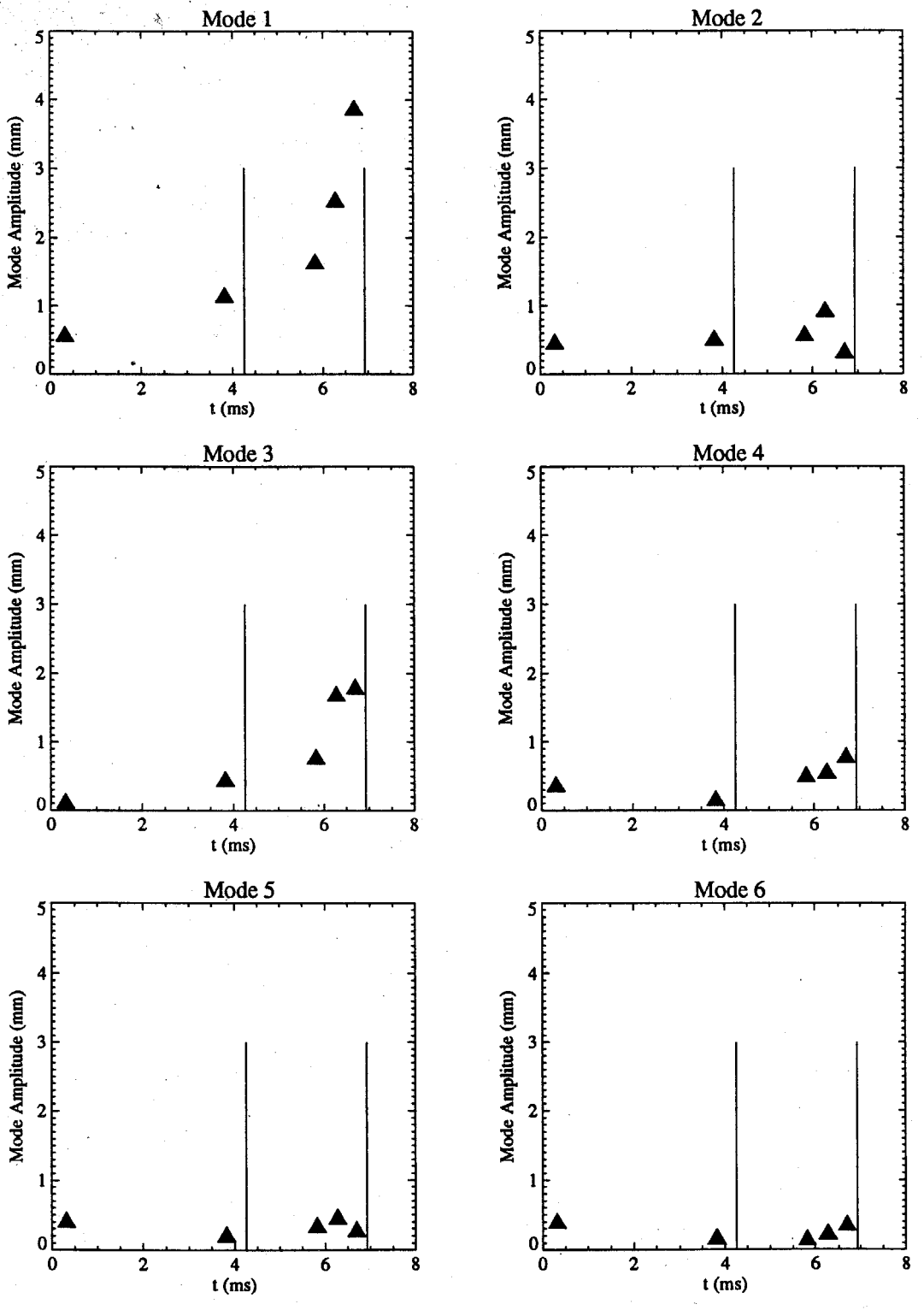

Fig.5.3.18 Far End Wall Configuration. τ = 8.0 s; M_i = 1.32. Amplitude of the First Six Modes *vs.* Time.

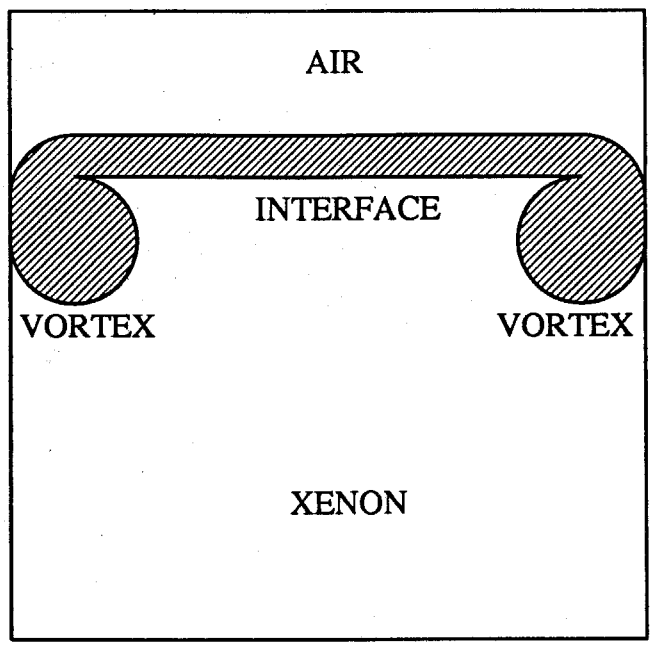

Fig.5.4.1 Schematic of Wall Vortices. Front View.

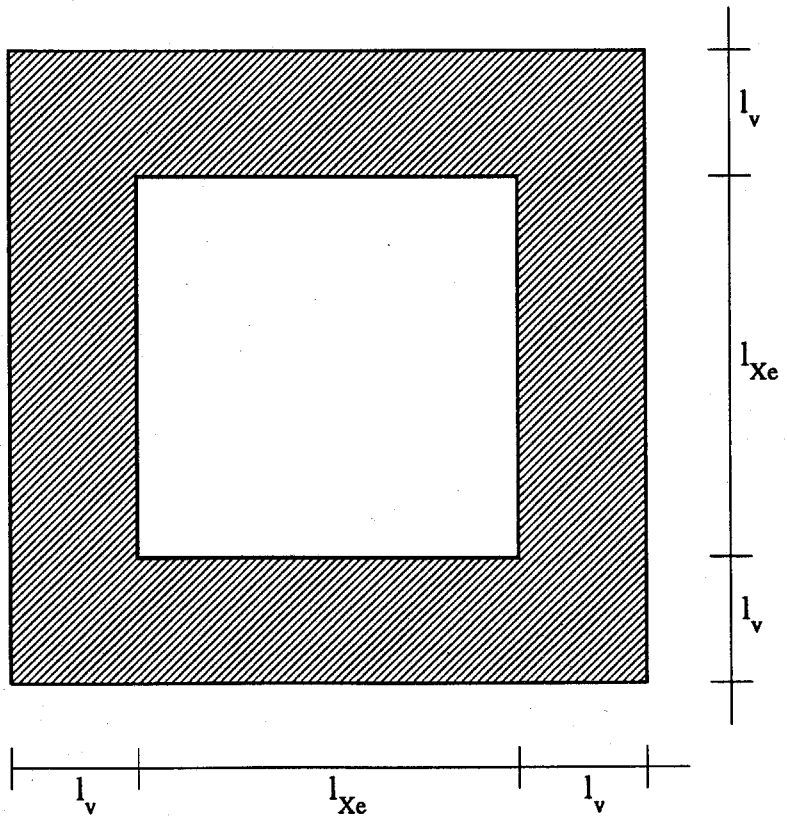

Fig.5.4.2 Schematic of Wall Vortices. Top View.

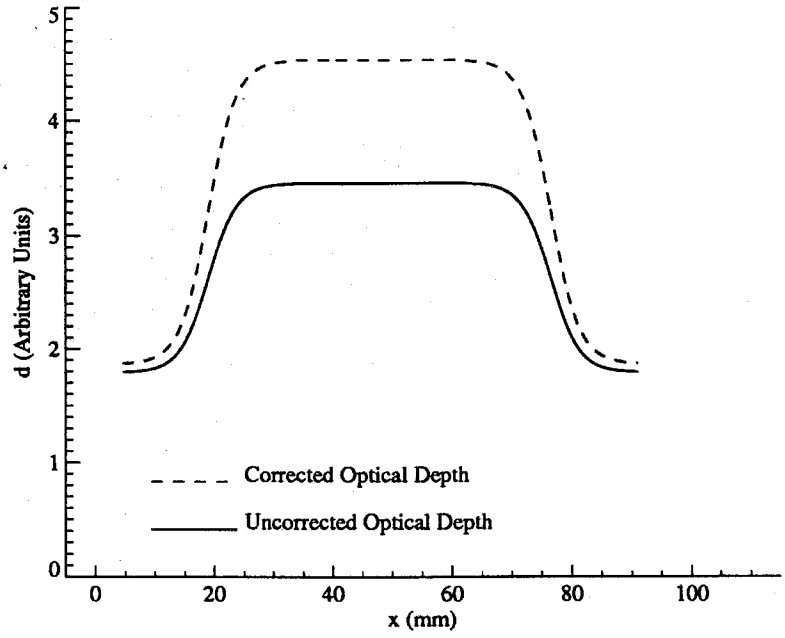

Fig.5.4.3 Correction of Optical Depth.

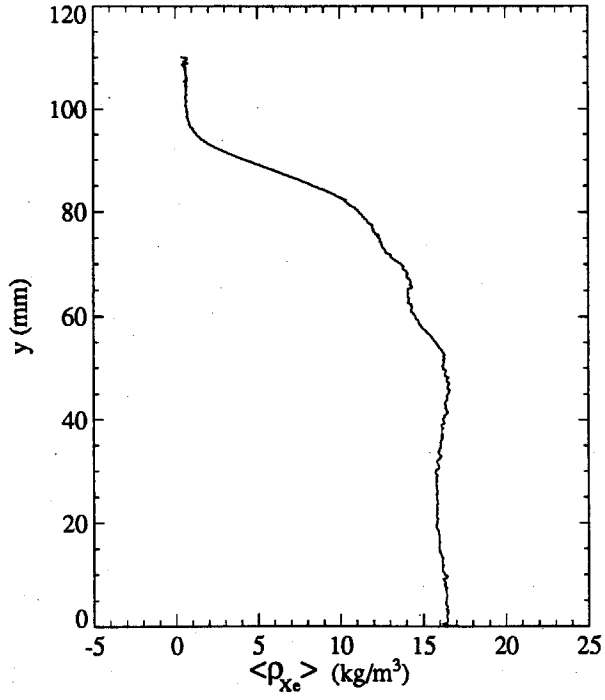

Fig.5.4.4 Run #0583. FEW. $\tau = 8.0$ s; $M_i = 1.32$; $t = 6.69$ ms. Corrected Average Density Profile. $x_l = 30$, $x_r = 65$.

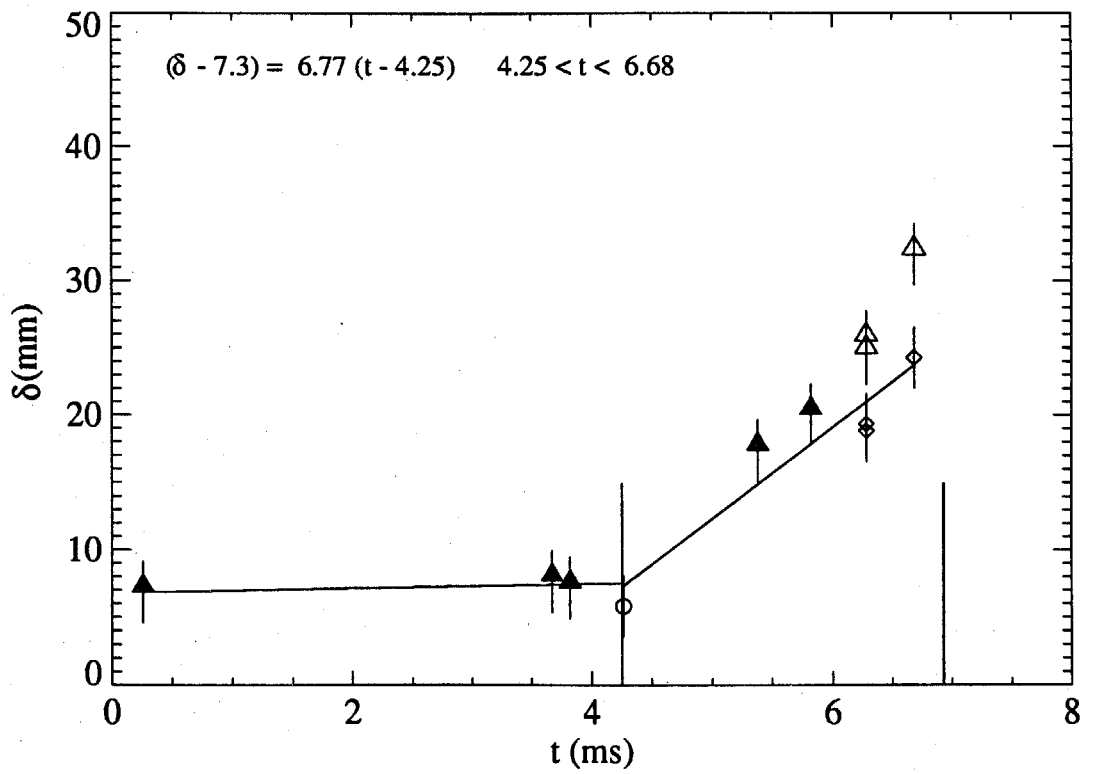

Fig.5.5.1 Far End Wall Configuration. τ = 1.2 s; M_i = 1.32. Interface Thickness *vs.* Time.

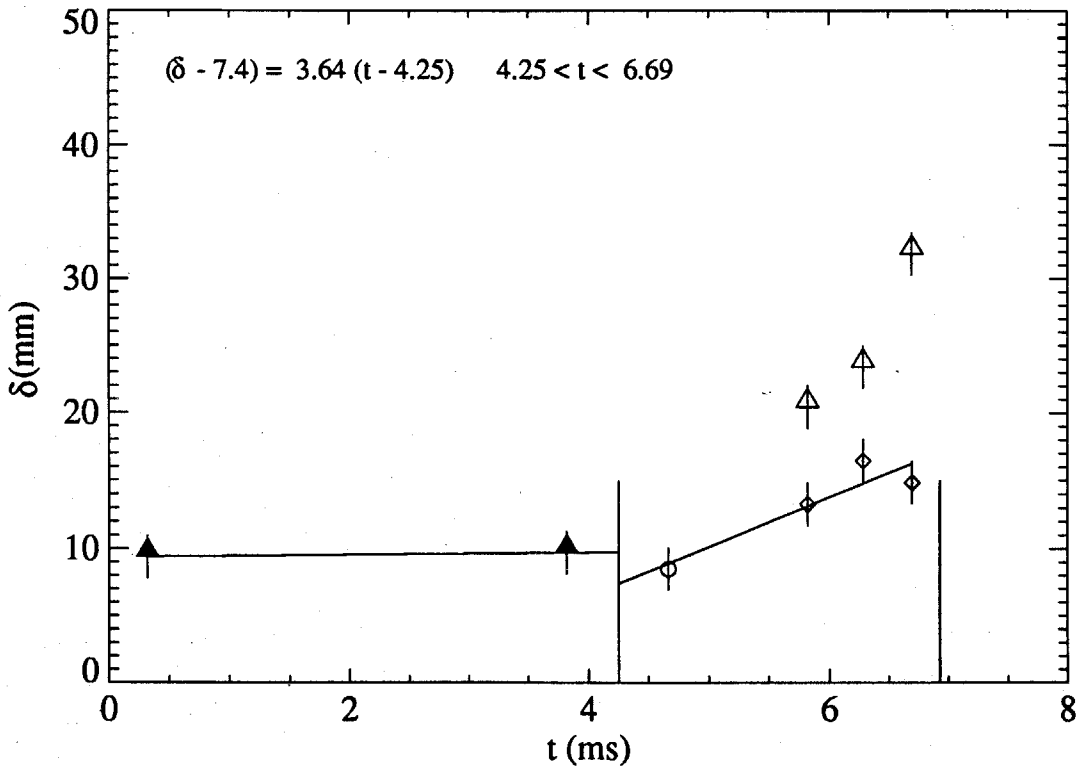

Fig.5.5.2 Far End Wall Configuration. τ = 8.0 s; M_i = 1.32. Interface Thickness *vs.* Time.

CHAPTER 6

MULTIPLY SHOCKED INTERFACES

6.1 Introduction

The experiments presented in this chapter are all performed in the close end wall configuration. The interface is initially located within the test section, 2 cm below the top edge of the windows, and 11 cm from the end wall of the shock tube. The goal is to study the effect of multiple wave reverberations on the growth of the interface perturbations and thickness. Both pseudo single scale and multiscale interfaces are studied, using accelerating shock waves of $M_i = 1.32$ and $M_i = 1.52$, and X-ray imaging and densitometry.

Schlieren visualization experiments are also performed, for the $M_i = 1.32$ case, on air/SF_6 and air/xenon interfaces, with both single scale and multiscale perturbations, to assure continuity with the work of Brouillette (1989), and lay some ground for a comparison between those results and the X-ray results obtained in the present experiments.

The $y - t$ diagram for the close end wall experiments on an air/xenon interface accelerated by a $M_i = 1.32$ shock wave is shown in Fig. 5.1.1 and discussed in Sec. 5.1; the diagram for an air/xenon interface and a $M_i = 1.52$ shock is shown in Fig. 6.1.1. The shock reflected in the air has $M_{r0} = 1.15$, the shock transmitted in the xenon has $M_t = 1.73$; the transmitted shock reflects from the end wall with $M_{r1} = 1.53$, intercepting the downward moving interface, setting it in an upward motion, and reflecting as an expansion wave.

For an air/SF_6 interface and a $M_i = 1.32$ shock (see Fig. 6.1.2) the transmitted wave has $M_t = 1.49$, and the shock reflected in the air has $M_{r0} = 1.09$; the wave reflected from the end wall has $M_{r1} = 1.47$.

The interaction times and interface position above the end wall for these two cases are given in table 6.1.1., where t_c and t_e indicate the times at which the first reflected shock reaches the interface, and the first reflected rarefaction reaches the interface, respectively. The properties of the two gases at the interface upon the first two wave interactions are reported in Tables 6.1.2 and 6.1.3 for the two cases, respectively.

Table 6.1.1. Interaction Times and Interface Positions. CEW Configuration.

Conditions	t_c (ms)	Int. Pos. (mm)	t_e (ms)	Int. Pos. (mm)
Air/Xe $M_i = 1.52$	0.54	52	0.83	67
Air/SF_6 $M_i = 1.32$	0.83	27	1.28	44

Table 6.1.2. Relevant Parameters for M_i =1 .52, Air/Xe Interface.

	Preshock	Shock	Reshock	Expansion
u (m/s)	0	152 ↓	55 ↑	25 ↓
ρ_{Air} (kg/m^3)	1.21	2.86	4.56	3.82
a_{Air} (m/s)	340	417	460	451
$(\rho a)_{Air}$ (kg/m^{2}s)	411	1193	2098	1723
ρ_{Xe} (kg/m^3)	5.46	10.82	15.70	13.78
a_{Xe} (m/s)	176	233	271	260
$(\rho a)_{Xe}$ (kg/m^{2}s)	960	2521	4255	3583
$\frac{(\rho a)_{Xe}}{(\rho a)_{Air}}$	2.33	2.11	2.03	2.08
A	0.637	0.582	0.550	0.566

Table 6.1.3. Relevant Parameters for M_i =1 .32, Air/SF_6 Interface.

	Preshock	Shock	Reshock	Expansion
u (m/s)	0	106 ↓	38 ↑	22 ↓
ρ_{Air} (kg/m^3)	1.21	2.15	3.08	2.94
a_{Air} (m/s)	340	387	417	413
$(\rho a)_{Air}$ (kg/m^2s)	411	832	1284	1216
ρ_{SF_6} (kg/m^3)	6.07	12.89	20.28	19.17
a_{SF_6} (m/s)	135	140	144	143
$(\rho a)_{SF_6}$ (kg/m^2s)	820	1805	2920	2740
$\frac{(\rho a)_{SF_6}}{(\rho a)_{Air}}$	1.99	2.17	2.27	2.25
A	0.667	0.714	0.736	0.734

6.2 Single Scale Interfaces

6.2.1 X-Ray Imaging and Densitometry

The properties of the interface just after interaction with an incident shock of M_i = 1.32 have been described in the previous chapter (Figs. 5.2.1 through 5.2.4). It is observed that no major changes occur on the interface until the interception with the shock reflected from the end wall. In the close end wall configuration, this interception takes place at t = 0.64 ms for M_i = 1.32; then the expansion fan reflected from the bottom reaches the interface at t = 1.20 ms. In the time interval between these two events the interface doesn't change its appearance. Figure 6.2.1 is the image of the optical density of a radiograph taken at 0.68 ms. Large disturbances have not yet developed on the interface, either on the X-ray picture or on the mean interface shape (Fig. 6.2.2), though the interface is tilted. At this stage the interface has an upward velocity of about 37 m/s. The average density profile is shown in Fig. 6.2.3, and from it an interface thickness of about 6 mm is measured,

indicating a compression due to the recent passage of the reflected shock.

The perturbations start to grow more visibly after the passage of the reflected expansion. At t = 2.04 ms, *i.e.*, only 0.94 ms after this interaction, the interface clearly shows three troughs and four crest (see Fig. 6.2.4). Wall vortices are also visible in the radiograph. By this time the interface has stopped moving inside the shock tube, locating itself at about 33 mm above the lower edge of the test section window. The mean interface shape is presented in Fig. 6.2.5, the density contours in Fig. 6.2.6 and the average density profile in Fig. 6.2.7.

The interface shown in Fig. 6.2.8 (t = 3.84 ms) has been processed by several reverberations of the wave field; the crests and troughs match fairly well the position of those in the previous photograph, and the plateau-like region on the right appears again, as confirmed by the mean interface shape shown in Fig. 6.2.9. The wall vortices are now more visible both in the photograph and in the density contours (Fig. 6.2.10). The average density profile is shown in Fig. 6.2.11.

By t = 5.85 ms (Fig. 6.2.16) the crest amplitude is of the order of the wavelength of the perturbations. Visual inspection of the radiograph shows the appearance of mushroom-like distortions on the sides of the second crest from the left. By this time the difference between the distortions of the upper and lower layers of the interface has become substantial (see the density contours in Fig. 6.2.18) and the interface shape, in Fig. 6.2.17, describes the distortion of a representative 'mean layer'. The interface thickness has grown to 14 mm, as seen in the density profile of Fig. 6.2.19.

Figure 6.2.24 is the interface at t = 7.57 ms (the latest time at which it is imaged); all of the elements progressively described for the previous pictures are present. The mean interface shape, the density contours and density profiles are shown in Figs. 6.2.25 through 6.2.27. It is to be noted that, in the many reverberation configuration, the wall vortices are never as large as they are, at the same times, in the far end wall geometry. Their effect on the measurements of the interface mean shape, and interface thickness (described in the previous chapter) are correspondingly smaller. The reason for the vortices being much smaller in the close end wall configuration than they are in the far end wall one is that they are generated by the interaction of the reflected shock with the interface distortion due to the boundary layer left behind it by the incoming shock (see Brouillette, 1989). The

wave travels from the heavy to the light gas, thus a phase reversal of the perturbation takes place, generating a spike of heavy gas which penetrates into the light one, generating a wall vortex. In this case the amplitude of the perturbation is of the order of the boundary layer thickness which is much smaller in the close end wall configuration than in the far end wall one.

Figures 6.2.28 and 6.2.29 show the interface mean shapes in time, for M_i =1.32 and M_i = 1.52, respectively. From the plot for M_i =1.32 one can deduce that the run to run repeatability of the phase of the perturbations is poor in some cases: *e.g.*, the interfaces near t = 6.0 ms do look similar, but shifted along the x-axis, one with respect to the other. The overall evolution of the interface distortion is nonetheless clear. These phase shifts seem less dramatic in the plot for M_1 = 1.52. The plots make use of a perspective view because, already by early times, the y-collocation of the interface within the test section is essentially constant and an ordinary two-dimensional plot would have all the shapes overlapping on each other.

The amplitude of the modes of the disturbances evolves as shown in Fig. 6.2.30 and Fig. 6.2.31, where the two vertical lines in each of the six plots indicate the arrival at the interface of the first reflected shock and first reflected expansion. Values for linear growth rates are obtained by least squares interpolation over different time intervals (indicated in Table 6.2.2 as $t_1 - t_2$) for the various modes. For M_i = 1.52, the first three modes exhibit growth rates that are about twice the corresponding ones in the M_i = 1.32 case, and mode 4 grows about three times faster; for both Mach numbers, all modes show saturation at amplitudes between 1.5 mm and 2.0 mm, except for mode 2 at M_i = 1.32 which seems not to saturate. The time evolution of modes 5 and 6 is also presented, but no linear fit is made to the data since their contribution to the interface shape appears negligible. The growth rates are summarized in Table 6.2.2, together with those calculated from the linear theory (Eq. 2.3.6), using the superposition of the effects of the first incident and reflected shocks and first reflected rarefaction.

The amplitudes and the thicknesses used to calculate the growth reduction factor ψ are those measured just after the incident shock, the reshock, and the reflected expansion. Other than for modes 1 and 3 with M_i =1 .52, all measured growth rates are smaller than the calculated ones. This may in large part be due to the fact that the growth rates depend

directly on the values of the amplitudes measured just after each interaction. In the present case the error in these measurements is probably large compared to the value itself, which is small. The measurements of the thickness have also an effect, since the growth reduction factor depends on them.

Table 6.2.2 Growth Rates of the First 4 Modes. Close End Wall Configuration.

Mode	$\frac{d\eta}{dt}$ (m/s)					
	$M_i = 1.32$			$M_i = 1.52$		
	$t_1 - t_2$ (ms)	measured	calculated	$t_1 - t_2$ (ms)	measured	calculated
1	1.1 - 4.75	0.24	0.58	0.8 - 3.5	0.41	0.20
2	1.1 - 4.75	0.33	1.61	0.8 - 3.5	0.57	1.00
3	1.1 - 4.75	0.41	1.58	0.8 - 2.5	0.98	0.23
4	1.1 - 4.75	0.29	2.02	0.8 - 2.0	0.98	4.43

In his close end wall measurements, Brouillette had found growth rates for an air/SF_6 interface accelerated by a $M_i = 1.32$ and $M_i = 1.48$ shock wave of 5.45 m/s and 11.68 m/s respectively (his theoretical values being 3.01 m/s and 7.69 m/s). The same considerations made for the comparison between the present work and his in the far end wall configuration apply to the close end wall one, *viz.* that the imaging techniques are different, and that the modal decomposition is only possible within the present data analysis. For an air/SF_6 interface, accelerated by a $M_i = 1.32$ shock, Brouillette had observed saturation of the growth of the perturbations at about $t = 2.0$ ms; in the experiments with an air/xenon interface interacting with a shock of the same strength, saturation does not take place until $t \approx 4.0$ ms at the earliest (for mode 4). The schlieren visualization experiments described in the next section show that an air/SF_6 interface evolves in time about 1.6 times faster than an air/xenon interface: Thus the comparison with Brouillette's findings is reasonable.

Plots of the interface thickness *vs.* time are presented in Fig. 6.2.32 for $M_i = 1.32$ and Fig. 6.2.33 for $M_i = 1.52$; linear fits made to the post-expansion data indicate that the interface thickness grows at rates of about 1.7 m/s and 1.9 m/s, respectively, from post-

expansion values of about 6 mm and 5 mm. For both Mach numbers the thickness increases steadily until about $t = 5.5$ ms after which it appears to drop (although only one data point is available at late times for the $M_i = 1.52$ case). Unfortunately, no power law behavior, after the linear one, can be deduced from the existing data.

The thickness growth rate for $M_i = 1.32$ in this multiple reverberation configuration (1.68 m/s) is 4 times smaller than that (6.77 m/s) observed in the far end wall configuration, where the same interface only interacts with the incident and the reflected shocks. One possible reason for this is that in the far end wall configuration the measured thickness is severely affected by the wall vortices (as was discussed in the previous chapter); because of this, the measured thickness values are overestimates of the real ones. Since this effect increases with time, the thickness growth rate is also overestimated.

Over a time interval of about 5 ms, laminar molecular diffusion would have increased the interface thickness to less than 7 mm, indicating an average growth rate of about 0.22 m/s. Taking the thickness as a measure of the mixing that occurs at the interface, it is seen that the reverberating waves enhance this mixing by a factor of about 10.

6.2.2 Schlieren Visualization

Schlieren photographs of air/SF_6 and air/xenon interfaces, taken at comparable times, are presented in Fig. 6.2.34 through Fig. 6.2.37. At $t = 1.62$ ms (Fig. 6.2.34) the air/SF_6 interface exhibits five crests and three troughs, and the air/xenon interface has four crests and three troughs. The air/SF_6 interface in this photo is apparently an exception, because in the later photos it also has four crests and three troughs. Wall vortices are already evident in both photographs. They form the two crests at the ends of each interface. Both pictures are taken after the interfaces have already interacted with the reflected expansion fan (see the $y - t$ diagrams). Prior to that event the disturbances on either interface are negligible.

Figure 6.2.35 shows the air/SF_6 interface at $t = 2.11$ ms and the air/xenon one at $t = 3.70$ ms. The periphery of the second crest from the left, in both pictures, has started to distort into a mushroom-like shape. The bottom of the photograph of the air/SF_6 interface shows a reverberating wave field between the interface and the end wall of the shock tube. Above it, the grey fine-scaled region lying roughly between the cross sections of the two

wall vortices is the image of the vortex on the front window of the test section. By these times the process seems out of its linear regime for both interfaces, in that the amplitude of the perturbations is of the same order of their wavelength, thus the linear theory for the growth rate of the perturbations (Eq. 2.3.6) would not be expected to apply. Nevertheless, using the theory to get an estimate of how the growth rates compare for the two interfaces gives the results presented in Table 6.2.1, in which are given the ratios of the growth rates of the various modes on the two interfaces,

$$\Gamma \equiv \frac{(\frac{d\eta}{dt})_{Air/SF_6}}{(\frac{d\eta}{dt})_{air/xenon}} , \qquad (6.2.1)$$

assuming an initial amplitude of 0.1 mm for all modes, an initial interface thickness of 10 mm, a 15% reduction of the thickness due to the incident shock, and neglecting the effects on the thickness of the reshock and of the first expansion.

Table 6.2.1. Ratios of the Calculated Growth Rates on Air/SF_6 and Air/Xenon Interfaces. Close End Wall Configuration. $M_i = 1.32$.

Mode	Γ		
	shock	reshock	rarefaction
1	1.29	1.98	1.07
2	1.27	2.04	1.23
3	1.26	2.01	21.18
4	1.26	2.04	14.39

After interaction with the incident shock the disturbances on the air/SF_6 interface grow faster than those on the air/xenon interface, because of a larger value of the product $A[v]$ (see Eq. 2.3.2); furthermore the reflected shock reaches the air/SF_6 interface later than it reaches the air/xenon interface. Because of both of these factors, the amplitude of the disturbances is larger on the air/SF_6 interface than on the air/xenon interface by the time the reflected shock arrives. This amplitude also appears as one of the factors in the expression for the growth rate. Upon interaction with the reshock, the product $A[v]$ is again larger for air/SF_6 than for air/xenon, and Γ is larger than after interaction with the

incident shock. The same observations apply when the reflected rarefaction interacts with the two interfaces. In this case the superposition of the various effects actually causes Γ for the various modes to behave strangely, in that the first two modes grow at almost the same rate, ($\Gamma \approx 1$) whereas the third and fourth mode growth rates are much larger for air/SF_6 than for air/xenon. ($\Gamma > 1$). From the experiments it is observed that an air/SF_6 interface imaged at time t looks closest to an air/xenon interface imaged at a time about 1.6 t. In fact, the two interfaces maintain their similarity at $t = 3.16$ ms (for air/SF_6) and $t = 5.19$ ms (for air/xenon) (see Fig. 6.2.36). The leftmost trough is more distinct on the air/SF_6 interface, but all other elements compare well. The mushroom-like distortion is now evident on all crests. By these times the photographs suggest the presence of three-dimensional effects: In particular, the third crest from the left on the air/SF_6 interface, and the second one on the air/xenon interface, actually look like two spikes, one in front of the other one. It is possible that these three dimensional effects are confined to regions near the windows and do not occur in the mean flow.

A final pair of schlieren photographs taken at $t = 4.68$ ms for air/SF_6 and $t = 7.21$ ms for air/xenon is shown in Fig. 6.2.37; the similarity between the two interfaces is still reasonable, although the only elements which are clearly distinguishable are the two crests and two troughs in the middle of the pictures. Thus, the schlieren images show that air/SF_6 and air/xenon interfaces look very similar at comparable times. Therefore, the differences between the radiographs of air/xenon interfaces and the schlieren images of air/SF_6 interfaces by Brouillette (1989) are due to the difference between the physical processes upon which the two imaging techniques are based (schlieren is sensitive to the density gradients in the field of view, whereas the signal recorded by X-ray imaging is a direct function of the density of the test gas), and not to a different response of the air/xenon interface to the impulsive acceleration.

6.3 Multiscale Interfaces

6.3.1 X-Ray Imaging and Densitometry

A multiscale, air/xenon interface imaged at $t = 0.32$ ms after interacting with a $M_i = 1.32$ shock was presented in Fig. 5.3.1. As described in the previous chapter, in the far end wall configuration not much happens to the interface until some time after interaction with the reflected shock, when wall effects become large, and actually affect the whole span of

the interface. In the close end wall case, the wall effects actually become visible after more than one reverberation, and their effect is never as large as in the far end wall configuration, for the reasons explained in Sec. 6.2.1.

Figure 6.3.1 is the image of a multiscale interface, taken at $t = 6.08$ ms. Wall vortices have appeared by this time, inducing some deformation on less than one third of the span of the interface, as can also be seen from the mean shape presented in Fig. 6.3.2. The interface thickness has grown to a value of about 14 mm. The interesting comparison is with a multiscale interface, reshocked only once, imaged at $t = 6.69$ ms, which is presented in Figs. 5.3.13 through 5.3.15; in that case, the wall vortices have grown so large that the effect the ones on the front and back windows have on X-ray absorption make it difficult to establish which is the real interface. In the present case, the density contours (Fig. 6.3.3) and the density profile (Fig. 6.3.4) show no plateau in the middle region, confirming that the effects of the wall vortices are small. In the same sense, the difference between the shapes of the top and bottom layers of the interface is smaller than it is in the far end wall configuration, and thus the mean interface shape does a better job in characterizing the interface as a whole. By $t = 11.07$ ms (Fig. 6.3.5) the distortions at the sides, induced by the images of the wall vortices, have become larger, but the middle of the interface is still essentially flat (Fig. 6.3.6). The density profile and contours are shown in Fig. 6.3.8 and Fig. 6.3.7, respectively.

The mean interface shape at various times is shown in Fig. 6.3.9 for $M_i = 1.32$ and Fig. 6.3.10 for $M_i = 1.52$. In both cases, the central portion of the mean interface shape is unperturbed at all times; the distortions at the sides are those due the wall vortices, and they appear more pronounced for $M_i = 1.52$.

To illustrate the quantitative effects of the wall vortices, the amplitudes of the first six modes *vs.* time are shown in Figs. 6.3.11 and 6.3.12, respectively. Interface thickening due to the Richtmyer-Meshkov instability, in the absence of wall effects, would induce no growth on the lower order modes. The fact that the wall effects are larger for $M_i = 1.52$ than for $M_i = 1.32$ is confirmed by the observation that the amplitude of all its modes is consistently larger.

The interface thickness as a function of time is given in Fig. 6.3.13 for $M_i = 1.32$, and Fig. 6.3.14 for $M_i = 1.52$. The growth rates are 1.03 m/s and 1.68 m/s, respectively, so, an increase in Mach number causes faster growth, *i.e.* faster mixing. For $M_i = 1.32$ the growth

is maintained all the way to 10.5 ms, whereas for $M_i = 1.52$ saturation is observed after about 7 ms. Both growth rates are smaller than their respective counterparts for the single scale interfaces. This might be due to both, the presence of large wavelength perturbations in the single scale case, and larger values of the initial thickness (with correspondingly larger values of the growth reduction factor, ψ, at all wavelengths) in the multiscale one.

The thickness growth rate for $M_i = 1.32$ (1.03 m/s) is 3.5 times smaller than that measured in the far end wall configuration (3.64 m/s) where the interface only interacts with the incident and one reflected shock. The same reasons suggested to explain the difference between the growth rates in the far and close end wall configurations for the single scale interfaces, *viz.* larger disturbances from thicker boundary layers, and thickness overestimates due to the presence of the wall vortices, apply in the multiscale case.

In his investigation of the thickness of a continuous, multiscale, air/SF_6 interface, Brouillette (1989) found a post-shock thickness of 11 mm and a growth rate of 2.4 m/s (*vs.* 1.05 m/s found in the present work), for $M_i = 1.32$ and a post-shock thickness of 9 mm and a rate of 4.4 m/s (*vs.* 1.7 ms reported here), for $M_i = 1.52$. This trend is opposite to what had been observed in the far end wall configuration where the measured thickness and growth rate were larger than those reported by Brouillette under the same conditions. The observations would thus suggest that the effect of the wall vortices is larger on the X-ray imaging than on the schlieren in the far end wall configuration, and smaller in the close end wall configuration. In conclusion, the discrepancy between the growth rates measured with X-rays imaging and those measured with schlieren imaging remains unresolved.

Brouillette proposed a (dimensional) correlation of the type

$$\frac{\mathrm{d}\delta}{\mathrm{d}t} = \chi \frac{A_0}{\delta_0'} \sum_{i=0}^{N-1} |[v]_i| \qquad (6.3.1)$$

and found a value of the constant χ of 0.17 $\pm$ 0.03 mm, by a least squares fit through his data. Applying the same model to the present results (for both single and multiscale interfaces, with N=3), yields a value of $\chi = 0.06 \pm 0.02$ mm. A slightly different model:

$$\frac{\mathrm{d}\delta}{\mathrm{d}t} = \chi \sum_{i=0}^{N-1} \frac{A_i}{\delta_i'} |[v]_i| \qquad (6.3.2)$$

has been tried to take into account the variations of the Atwood number and of the thickness due to each wave, but the constant χ turns out to have the same value, and only slightly less scatter.

As for the single scale interfaces, no power law behavior, after the linear one, can be deduced from the existing data. Table 6.3.1 presents a summary of the thickness growth rates from the present experiments and those of Brouillette (1989).

Table 6.3.1 Thickness Growth Rates. Close End Wall Configuration.

τ (s)	M_i	Present		Brouillette (1989)	
		$\frac{d\delta}{dt}$ (m/s)	χ	$\frac{d\delta}{dt}$ (m/s)	χ
1.2	1.32	1.68	0.06	NA	NA
1.2	1.52	1.86	0.06	NA	NA
8.0	1.32	1.03	0.06	2.4	0.17
8.0	1.52	1.86	0.06	4.4	0.17

6.3.2 Schlieren Visualization

As for the single scale case, experiments have been performed using the schlieren visualization technique on both air/xenon and air/SF_6 multiscale interfaces. The purpose is again to make sure that air/xenon and air/SF_6 exhibit the same properties when imaged with the same method.

Figure 6.3.15 shows schlieren photographs of an air/SF_6 and an air/xenon interfaces imaged at $t = 3.14$ ms and $t = 6.20$ ms, respectively. In both cases the wall vortices and the 'humps' they induce on the sides of the interface are clearly evident. In the air/SF_6 picture, the gray region below the interface represents the wall vortex on the front window of the test section. A similar region, although less clear, is visible in the air/xenon photograph.

As time increases the wall vortices and the perturbations they induce grow larger; Fig. 6.3.16 shows the photos of the two interfaces at $t = 4.19$ ms and $t = 9.37$ ms, respectively. The central portion of the interface stays essentially flat, and it's only its thickness that increases. The wall vortices actually induce larger 'humps' on the air/SF_6 interface than they do on the air/xenon. The distinction between the real interface and the wall vortex on the front window becomes more difficult to make. Throughout the process, an air/SF_6 interface at time t looks closest to an air/xenon interface at time about 2 t, as opposed to a time of about 1.6 t observed for the single scale interfaces.

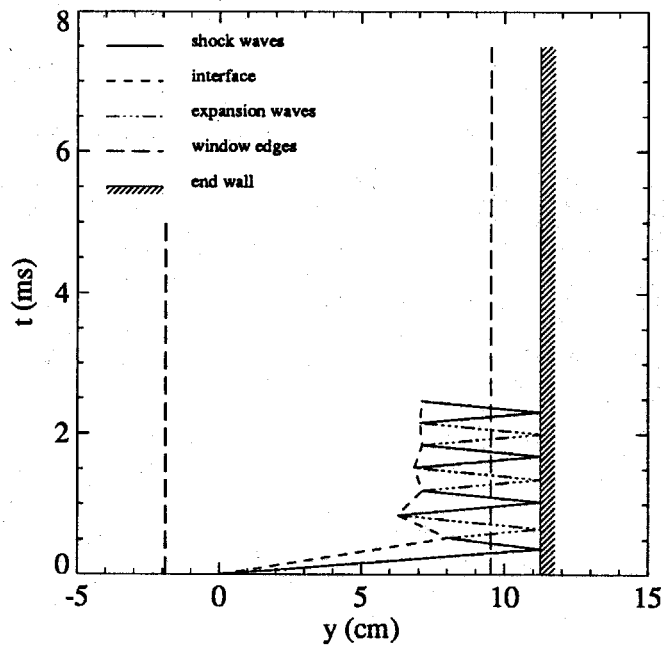

Fig.6.1.1 $y-t$ Diagram for Air/Xe Interface, M_i =1.52, Close End Wall Configuration.

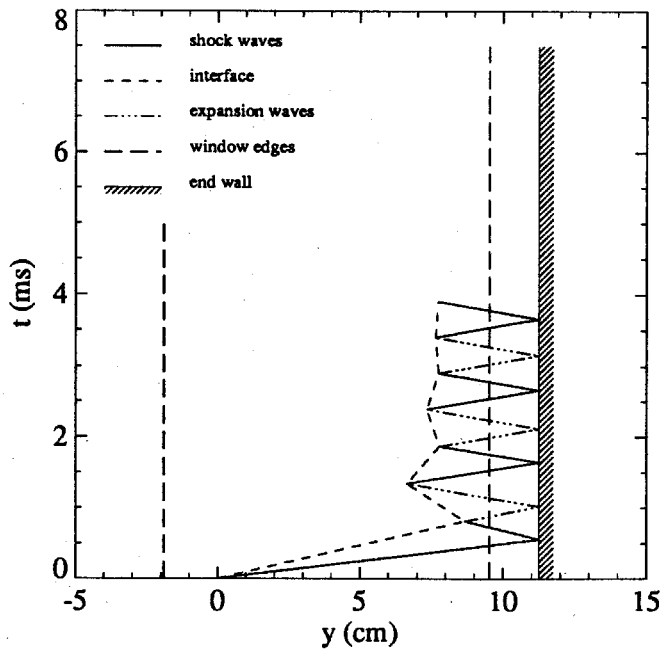

Fig.6.1.2 $y-t$ Diagram for Air/SF_6 Interface, M_i =1.32, Close End Wall Configuration.

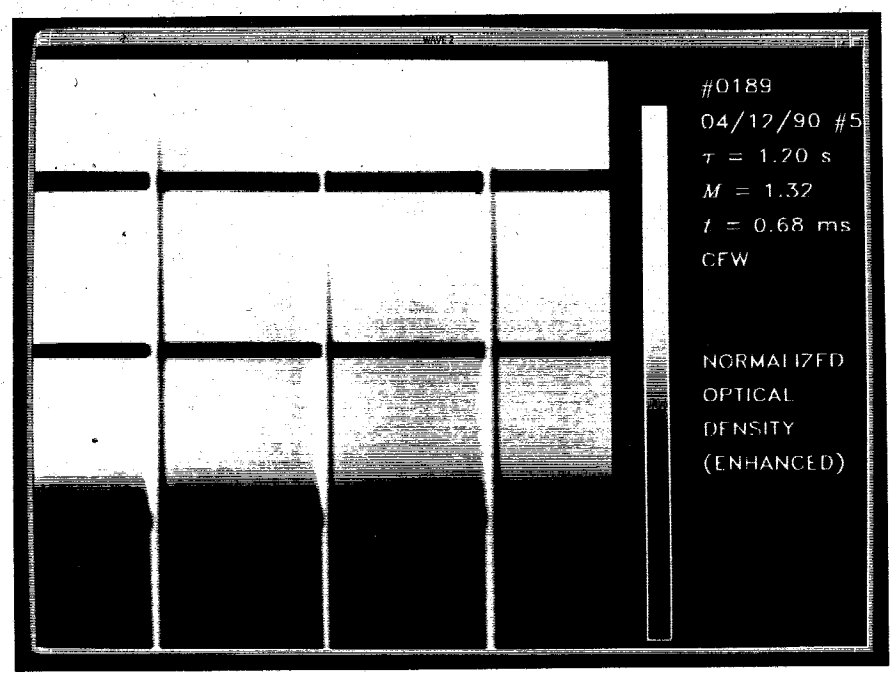

Fig.6.2.1 Air/Xenon. Run #0189. CEW. $\tau = 1.2$ s; $M_i = 1.32$; $t = 0.68$ ms. Optical Density of the Radiograph.

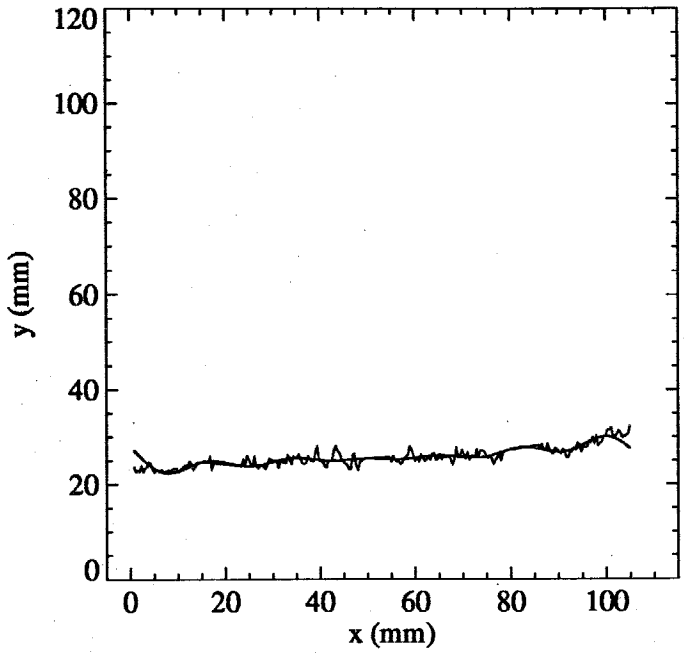

Fig.6.2.2 #0189. CEW. $\tau = 1.2$ s; $M_i = 1.32$; $t = 0.68$ ms. Configuration. Mean Interface Shape.

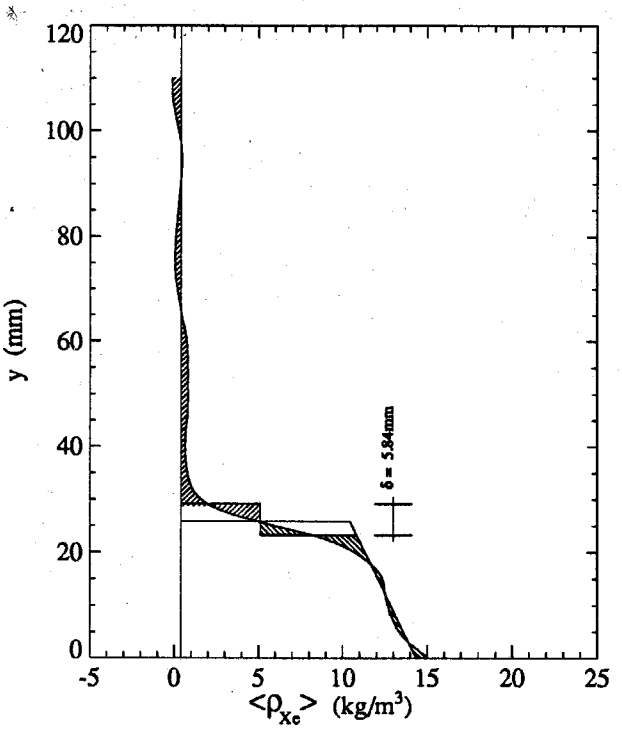

Fig.6.2.3 #0189. CEW. $\tau = 1.2$ s; $M_i = 1.32$; $t = 0.68$ ms. Average Density Profile. $x_l = 0$, $x_r = 105$.

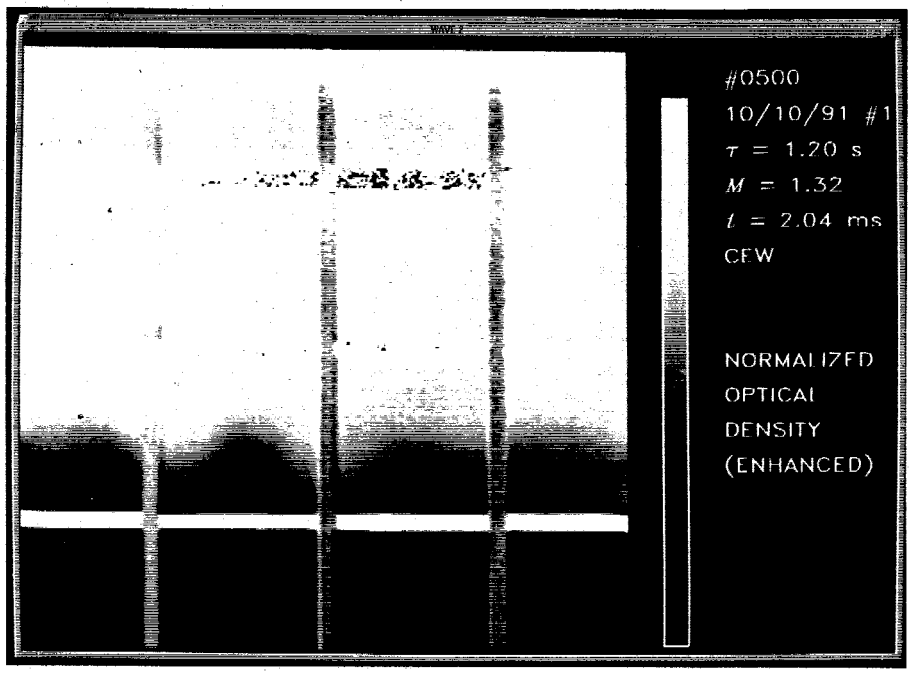

Fig.6.2.4 Air/Xenon. Run #0500. CEW. $\tau = 1.2$ s; $M_i = 1.32$; $t = 2.04$ ms. Optical Density of the Radiograph.

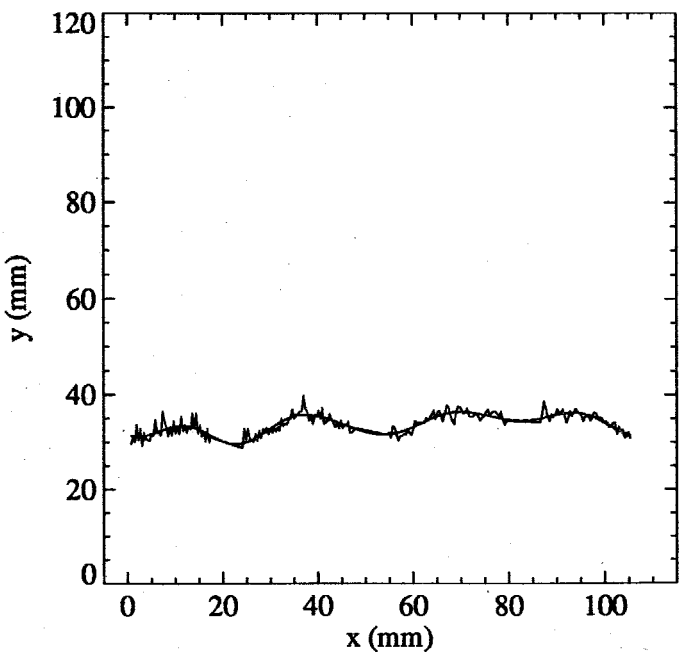

Fig.6.2.5 Run #0500. CEW. $\tau = 1.2$ s; $M_i = 1.32$; $t = 2.04$ ms. Mean Interface Shape.

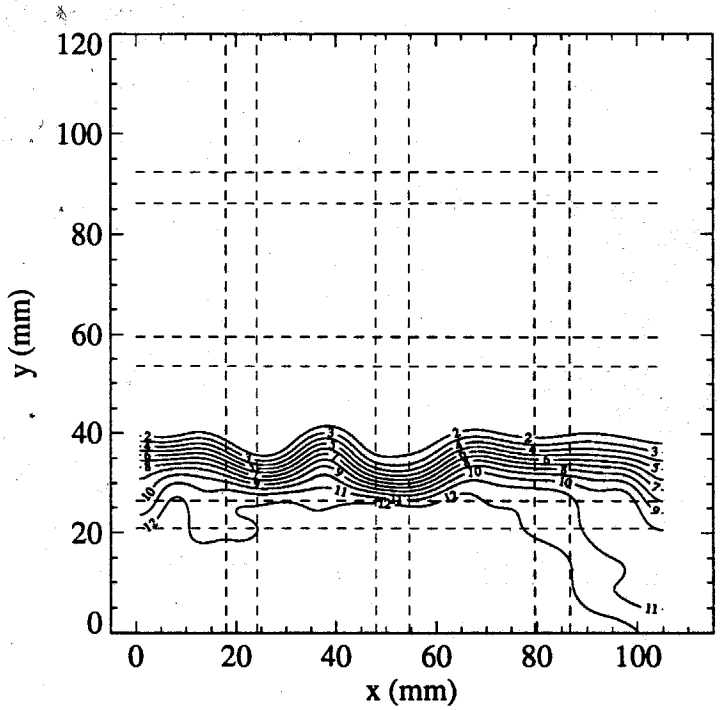

Fig.6.2.6 Run #0500. CEW. τ = 1.2 s; M_i = 1.32; t = 2.04 ms. Density Contours.

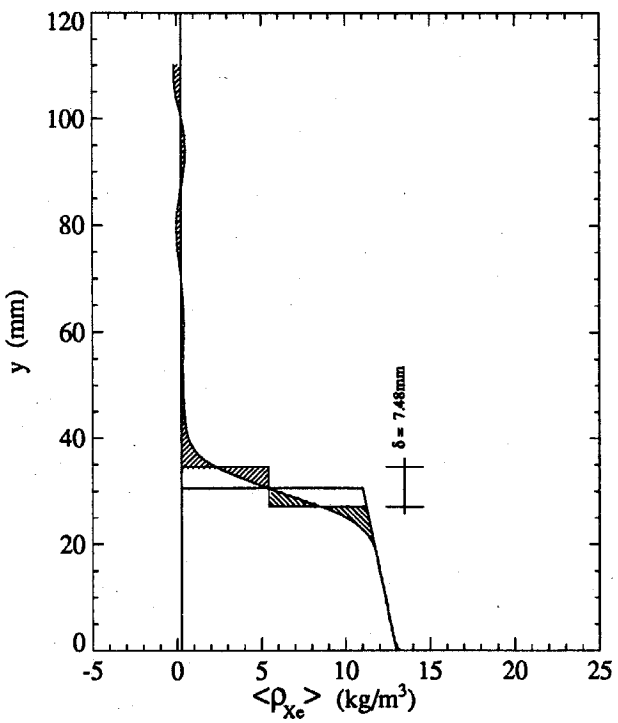

Fig.6.2.7 Run #0500. CEW. τ = 1.2 s; M_i = 1.32; t = 2.04 ms. Average Density Profile. $x_l = 0$, $x_r = 105$.

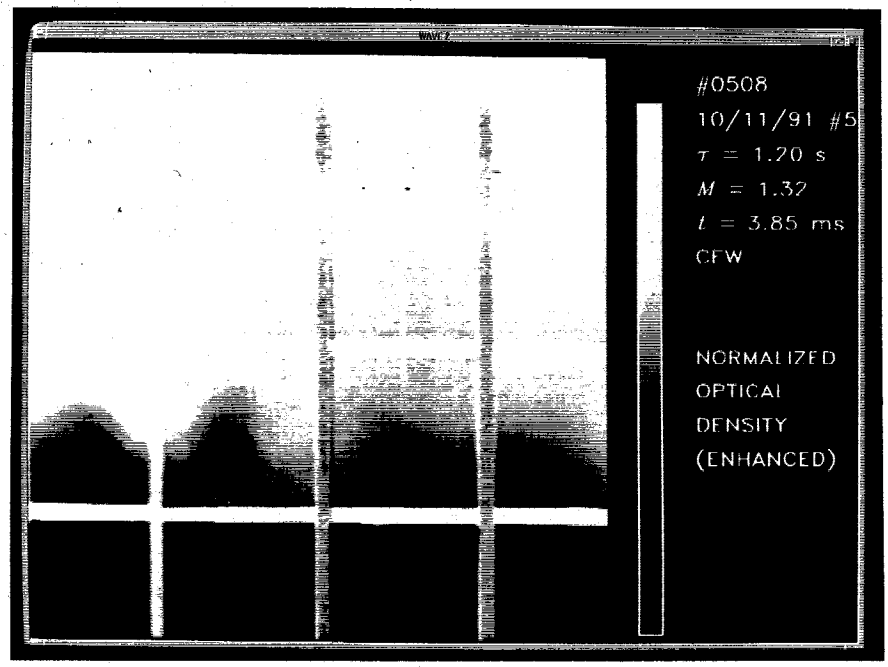

Fig.6.2.8 Air/Xenon. Run #0508. CEW. $\tau = 1.2$ s; $M_i = 1.32$; $t = 3.85$ ms. Optical Density of the Radiograph.

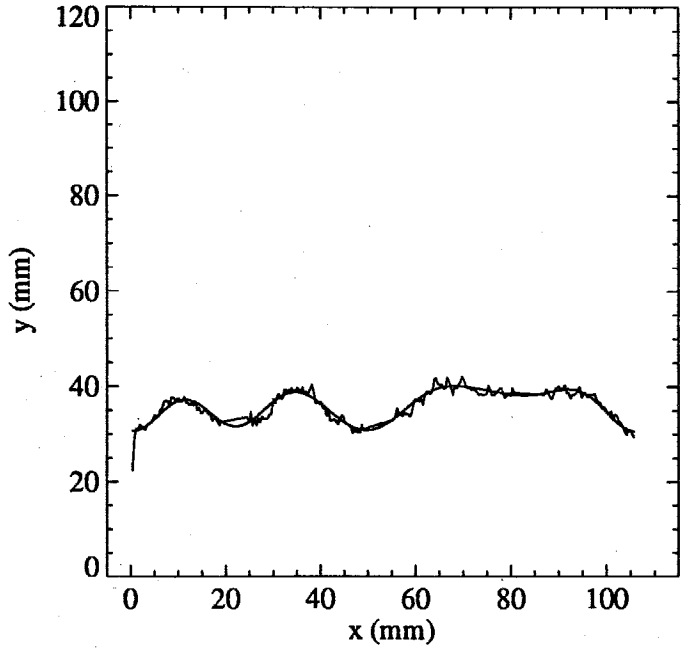

Fig.6.2.9 Run #0508. CEW. $\tau = 1.2$ s; $M_i = 1.32$; $t = 3.85$ ms. Mean Interface Shape.

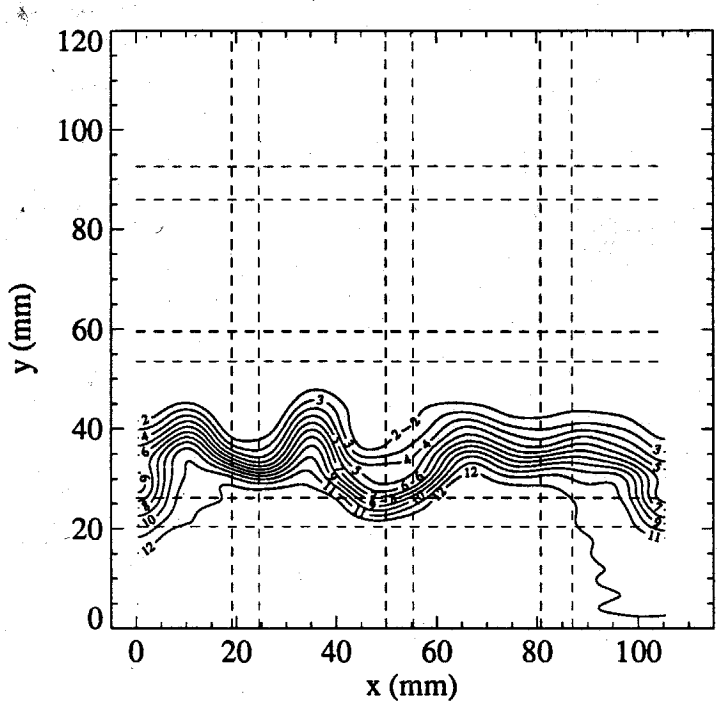

Fig.6.2.10 Run #0508. CEW. τ = 1.2 s; M_i = 1.32; t = 3.85 ms. Density Contours.

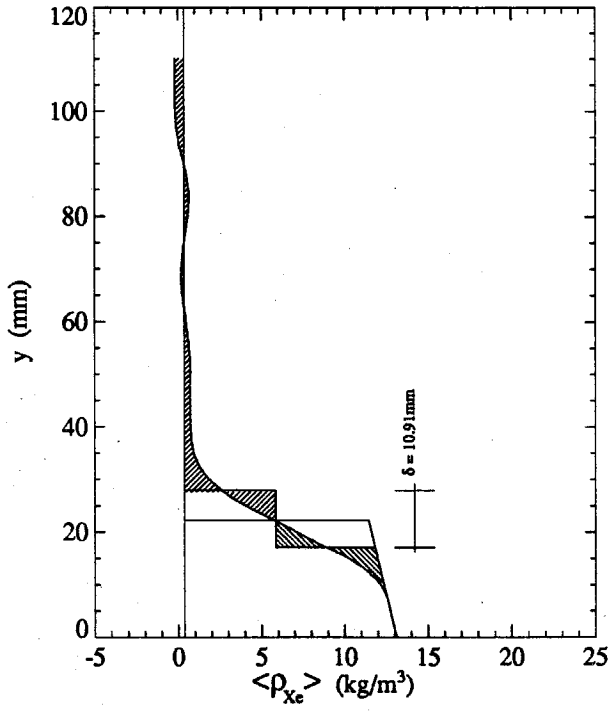

Fig.6.2.11 Run #0508. CEW. τ = 1.2 s; M_i = 1.32; t = 3.85 ms. Average Density Profile. x_l = 10, x_r = 95.

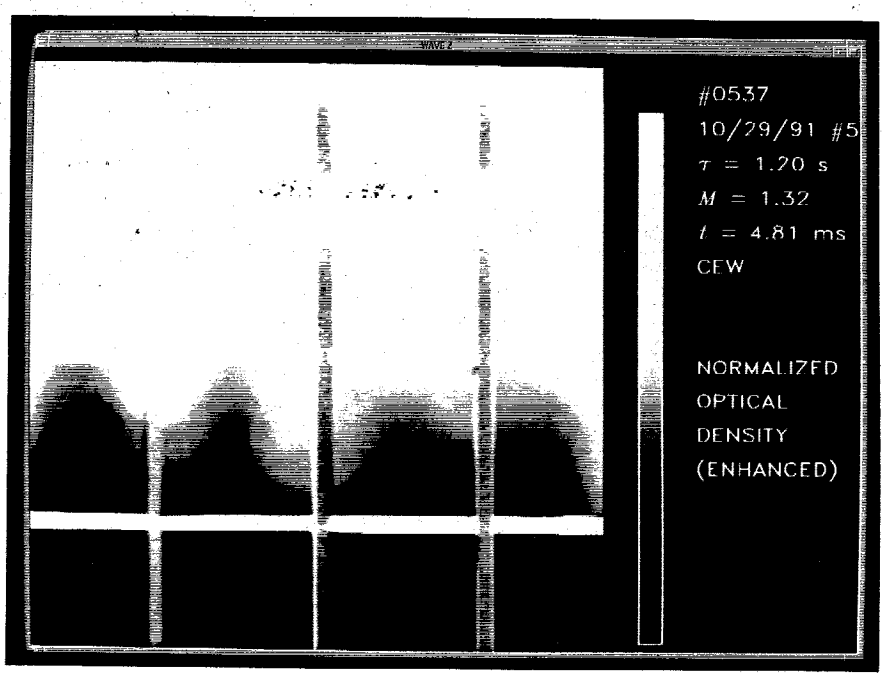

Fig.6.2.12 Air/Xenon. Run #0537. CEW. $\tau = 1.2$ s; $M_i = 1.32$; $t = 4.81$ ms. Optical Density of the Radiograph.

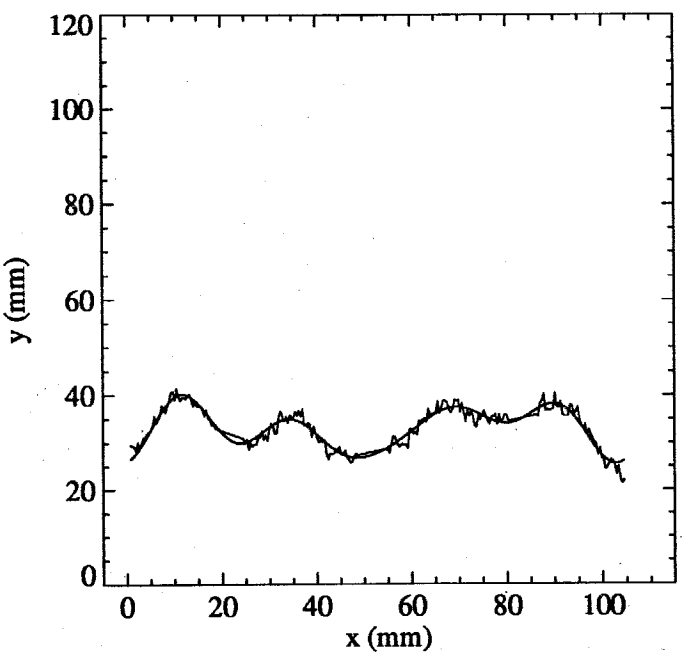

Fig.6.2.13 Run #0537. CEW. $\tau = 1.2$ s; $M_i = 1.32$; $t = 4.81$ ms. Mean Interface Shape.

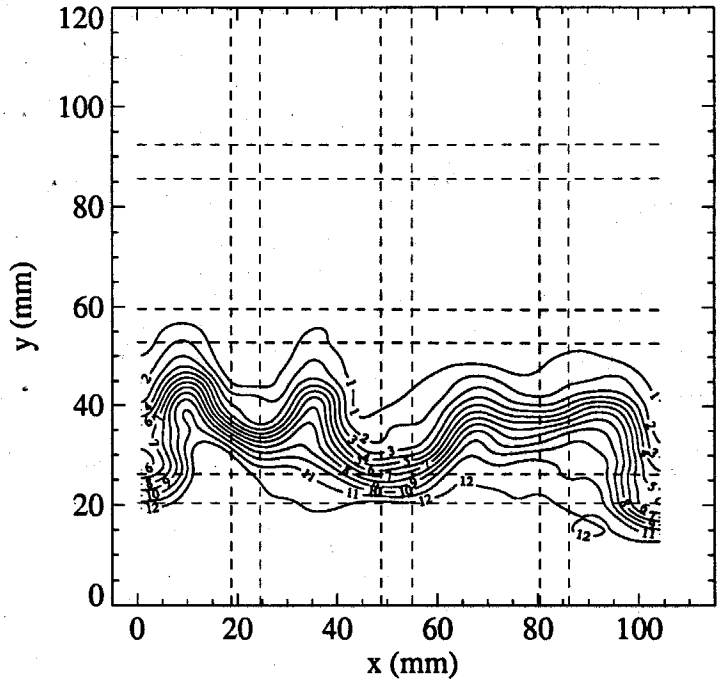

Fig.6.2.14 Run #0537. CEW. τ = 1.2 s; M_i = 1.32; t = 4.81 ms. Density Contours.

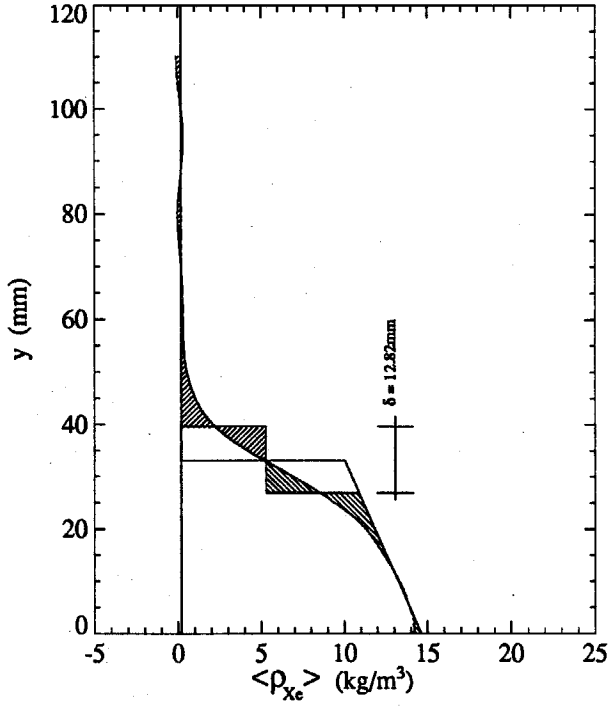

Fig.6.2.15 Run #0537. CEW. τ = 1.2 s; M_i = 1.32; t = 4.81 ms. Average Density Profile. x_l = 10, x_r = 95.

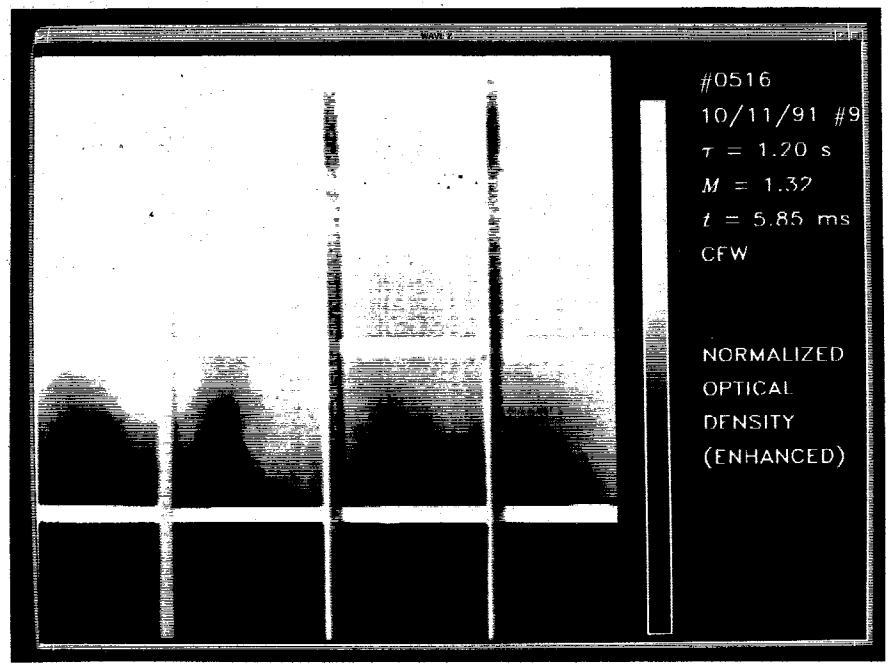

Fig.6.2.16 Air/Xenon. Run #0516. CEW. $\tau = 1.2$ s; $M_i = 1.32$; $t = 5.85$ ms. Optical Density of the Radiograph.

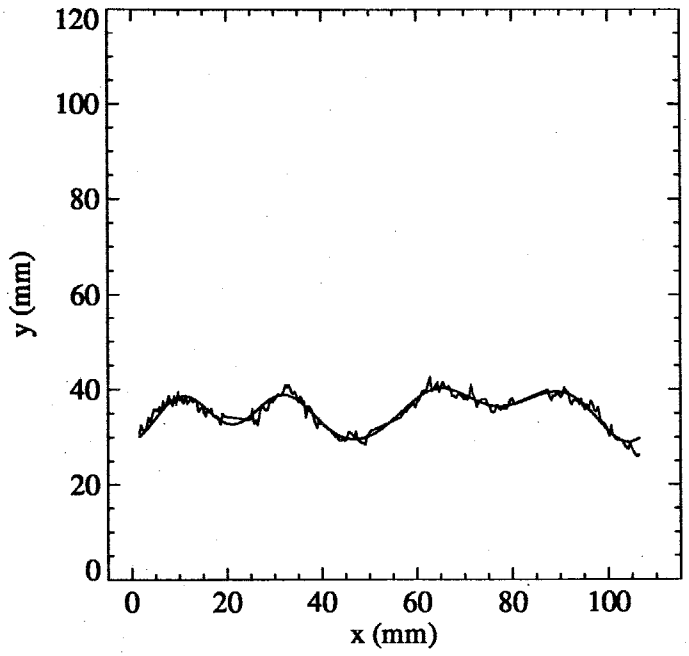

Fig.6.2.17 Run #0516. CEW. $\tau = 1.2$ s; $M_i = 1.32$; $t = 5.85$ ms. Mean Interface Shape.

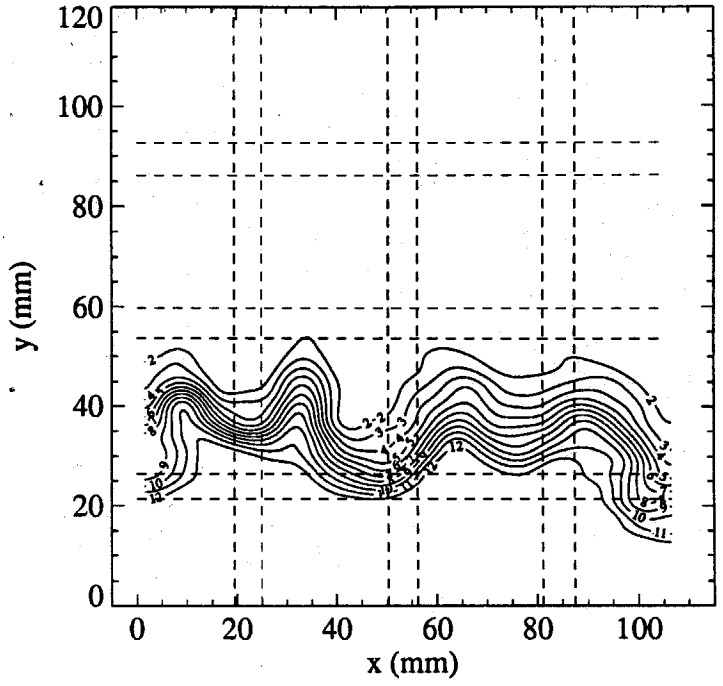

Fig.6.2.18 Run #0516. CEW. τ = 1.2 s; M_i = 1.32; t = 5.85 ms. Density Contours.

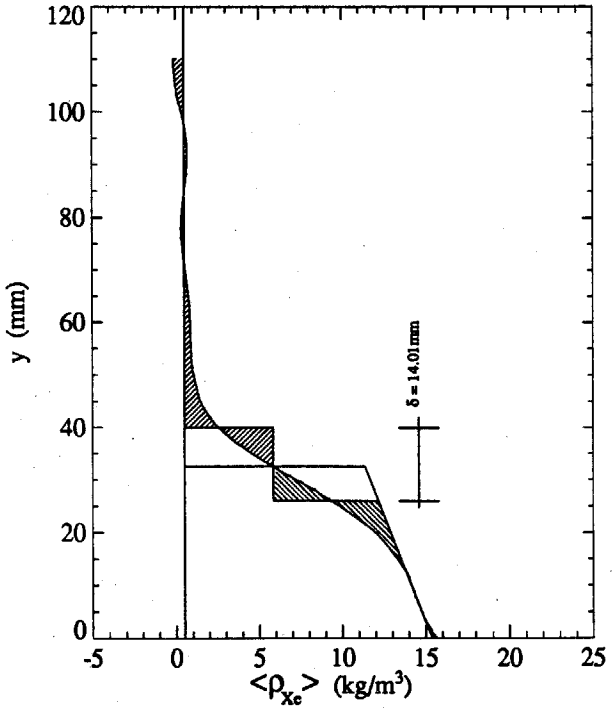

Fig.6.2.19 Run #0516. CEW. τ = 1.2 s; M_i = 1.32; t = 5.85 ms. Average Density Profile. x_l = 15, x_r = 90.

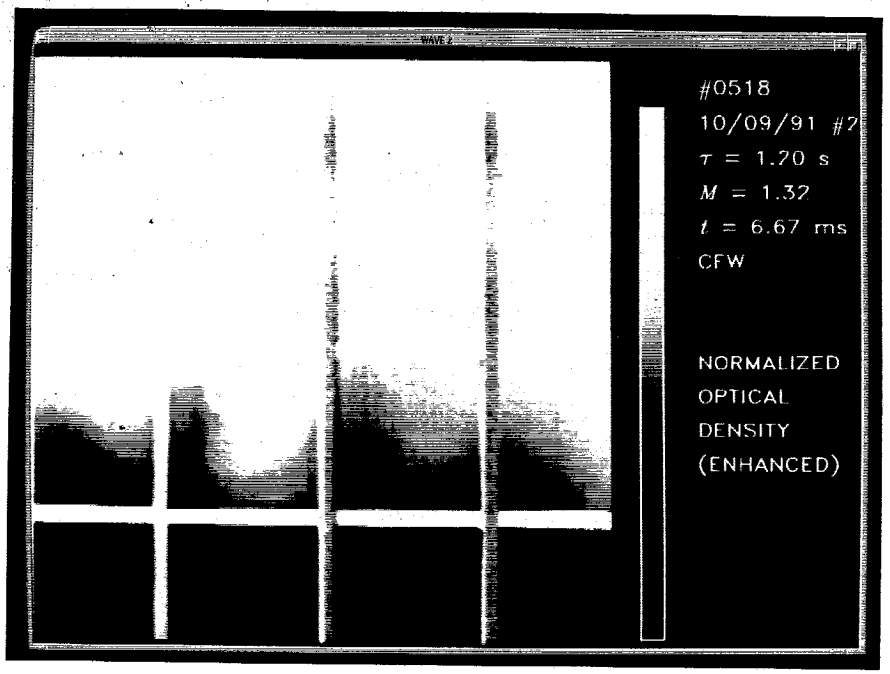

Fig.6.2.20 Air/Xenon. Run #0518. CEW. $\tau = 1.2$ s; $M_i = 1.32$; $t = 6.67$ ms. Optical Density of the Radiograph.

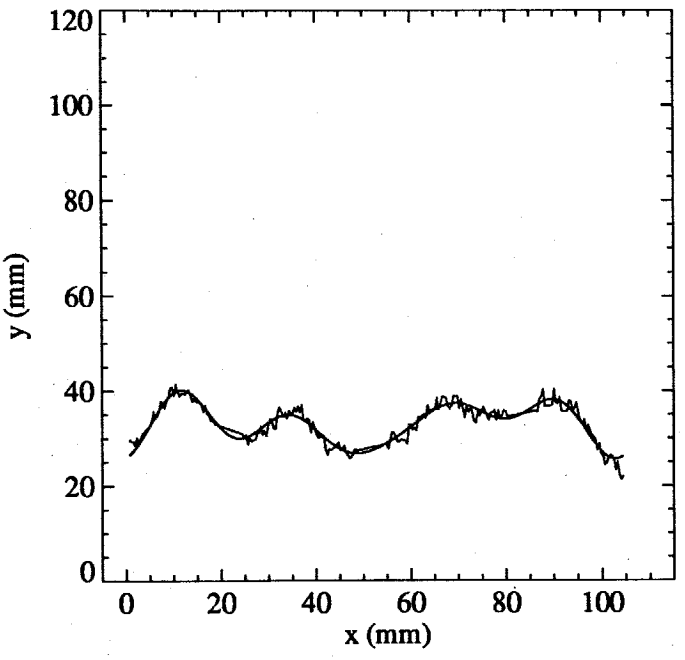

Fig.6.2.21 Run #0518. CEW. $\tau = 1.2$ s; $M_i = 1.32$; $t = 6.67$ ms. Mean Interface Shape.

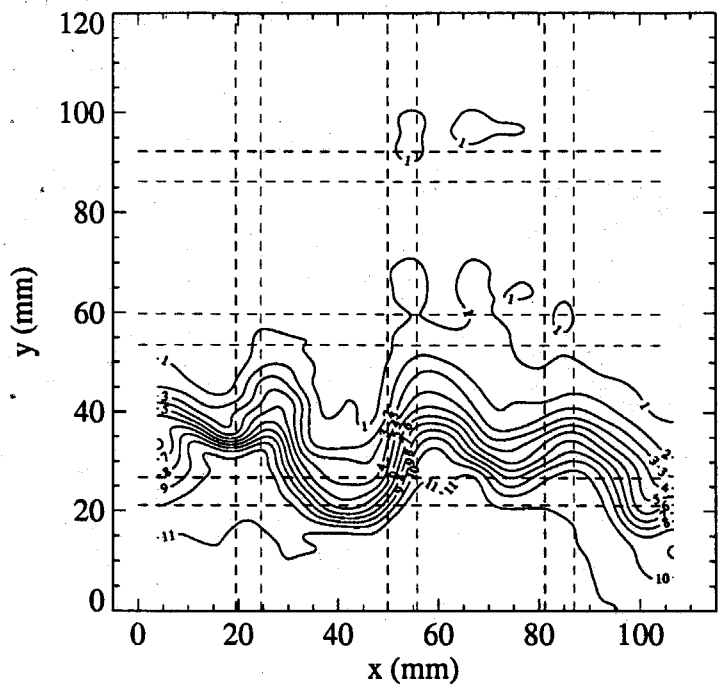

Fig.6.2.22 Run #0518. CEW. τ = 1.2 s; M_i = 1.32; t = 6.67 ms. Density Contours.

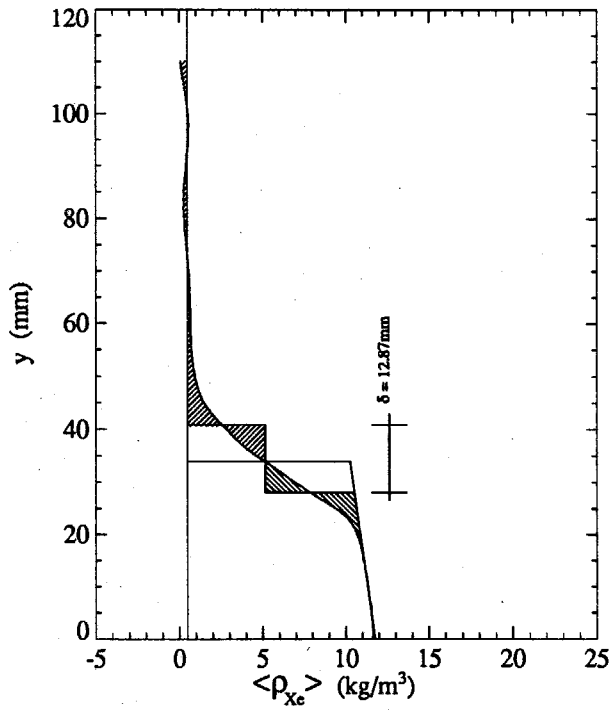

Fig.6.2.23 Run #0518. CEW. τ = 1.2 s; M_i = 1.32; t = 6.67 ms. Average Density Profile. x_l = 15, x_r = 90.

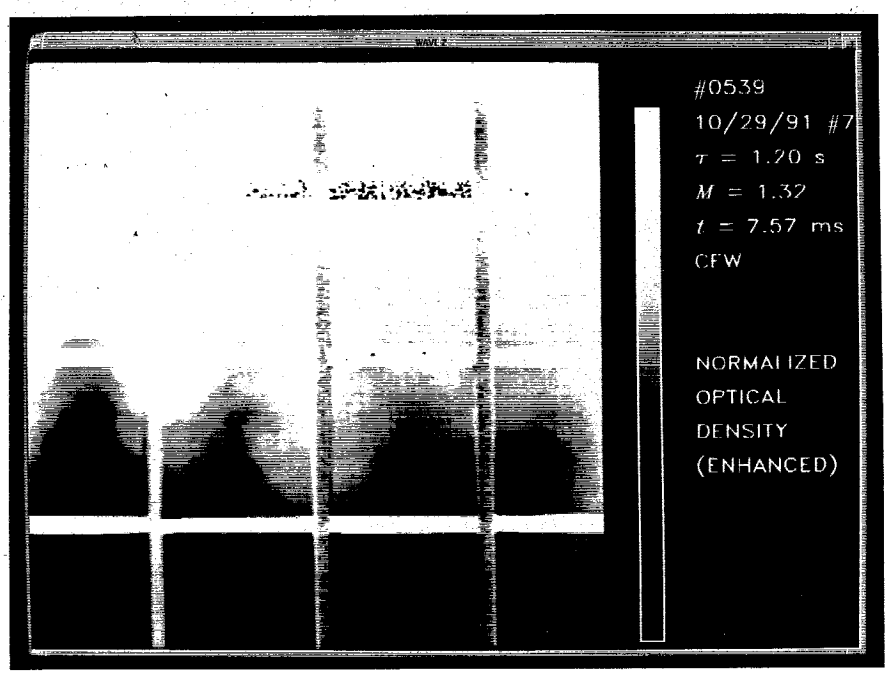

Fig.6.2.24 Air/Xenon. Run #0539. CEW. $\tau = 1.2$ s; $M_i = 1.32$; $t = 7.57$ ms. Optical Density of the Radiograph.

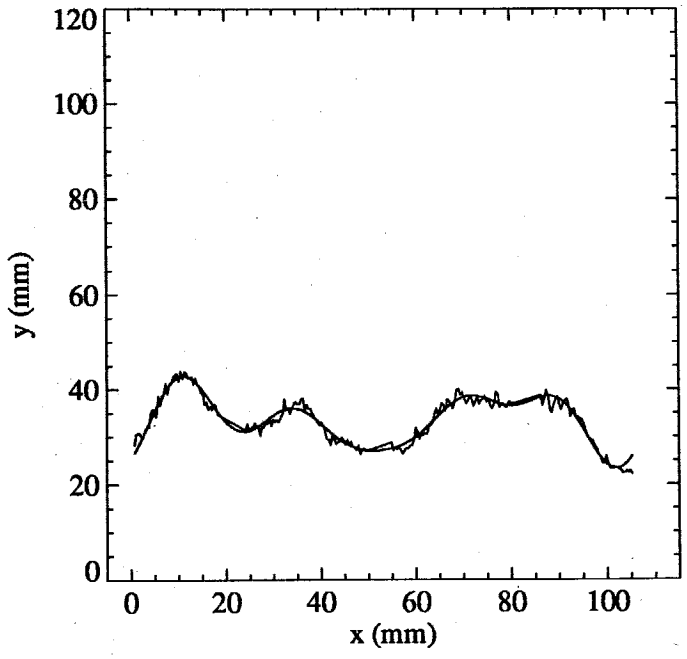

Fig.6.2.25 Run #0539. CEW. $\tau = 1.2$ s; $M_i = 1.32$; $t = 7.57$ ms. Mean Interface Shape.

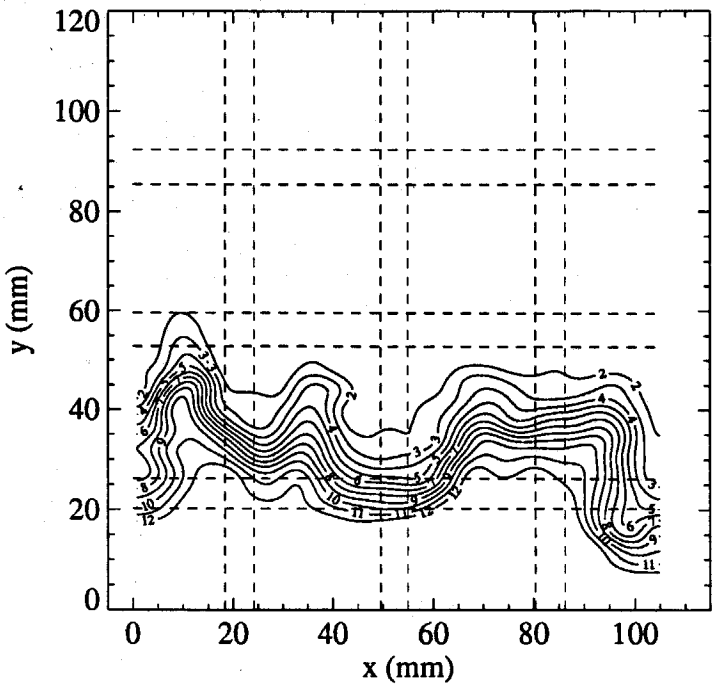

Fig.6.2.26 Run #0539. CEW. τ = 1.2 s; M_i = 1.32; t = 7.57 ms. Density Contours.

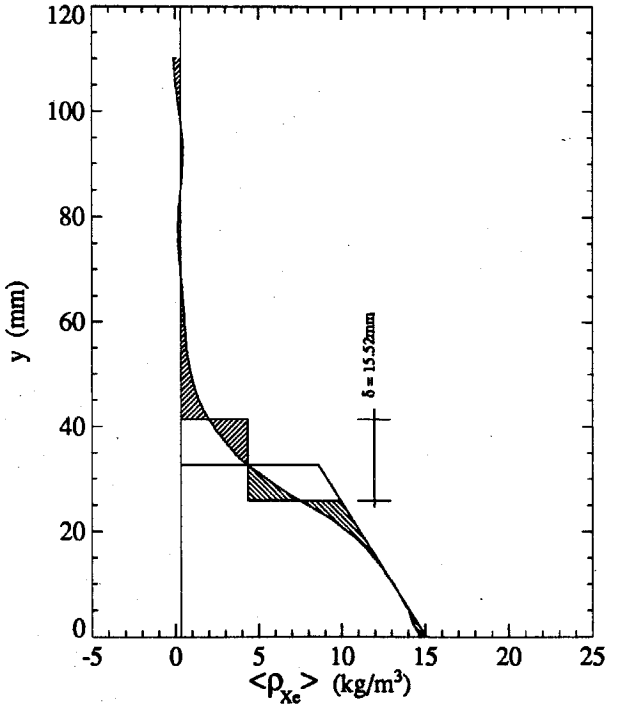

Fig.6.2.27 Run #0539. CEW. τ = 1.2 s; M_i = 1.32; t = 7.57 ms. Average Density Profile. x_l = 15, x_r = 90.

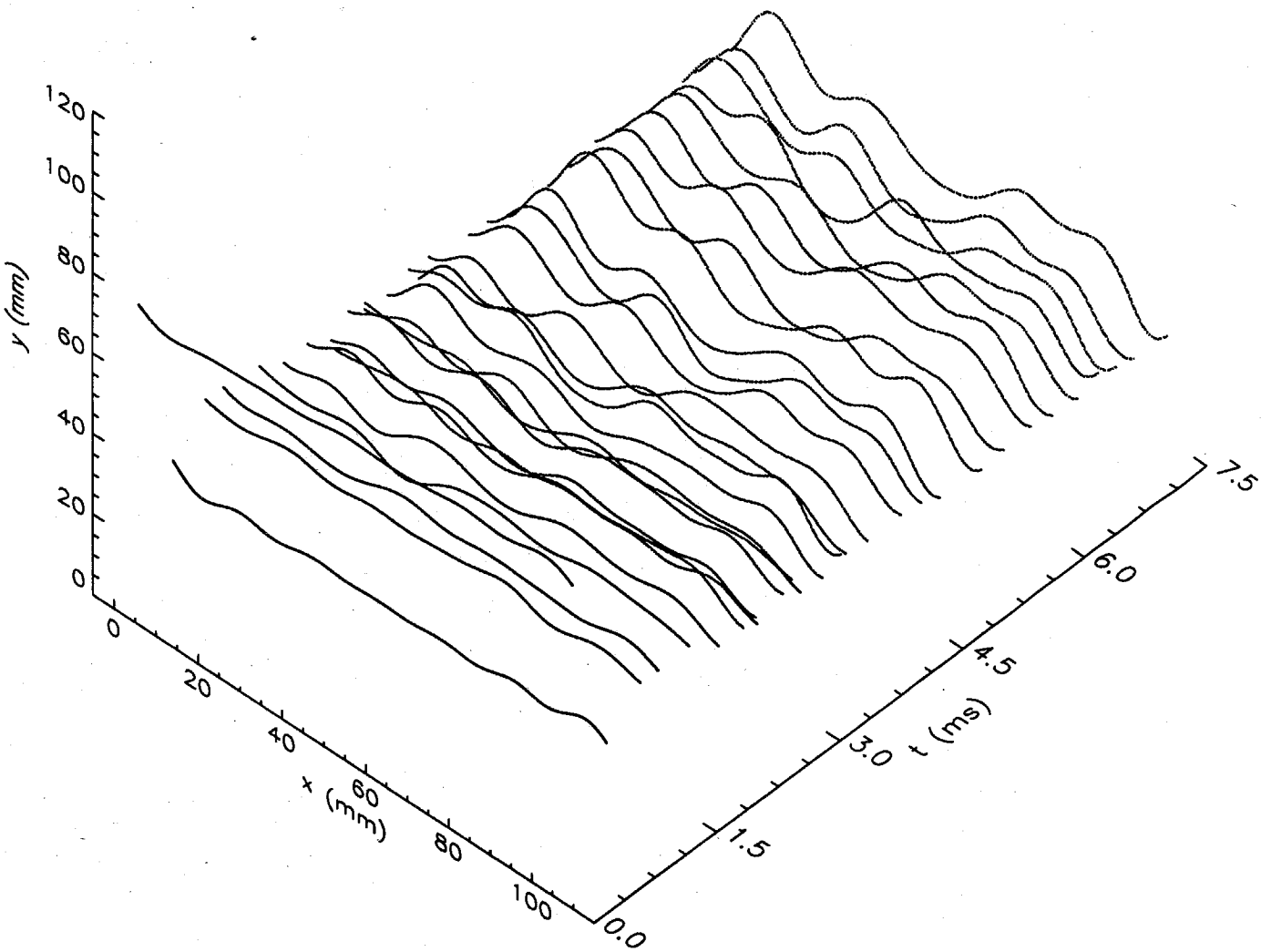

Fig.6.2.28 $M_i = 1.32$; $\tau = 1.2$ s Close End Wall Configuration. Mean Interface Shape at Various Times.

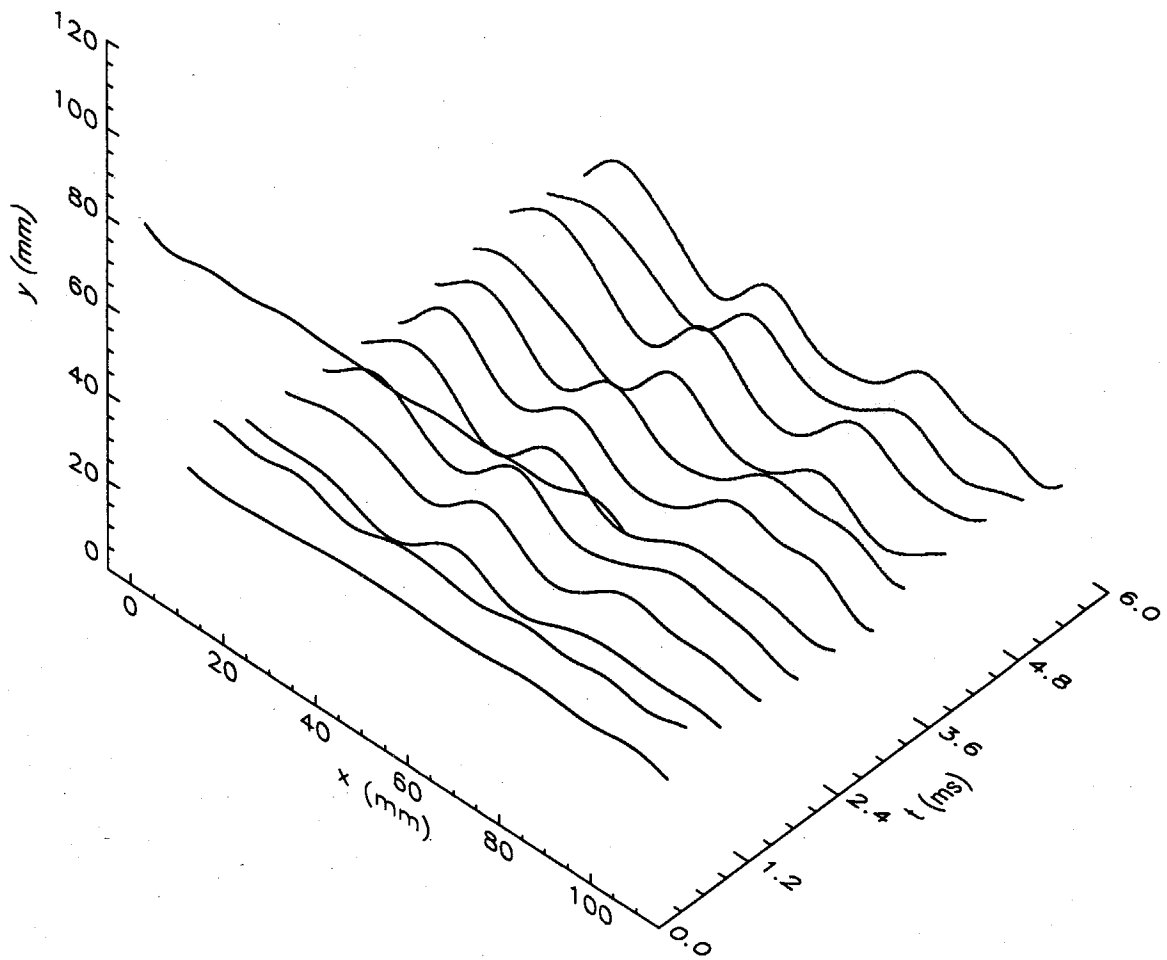

Fig.6.2.29 $M_i = 1.52$; $\tau = 1.2$ s Close End Wall Configuration. Mean Interface Shape at Various Times.

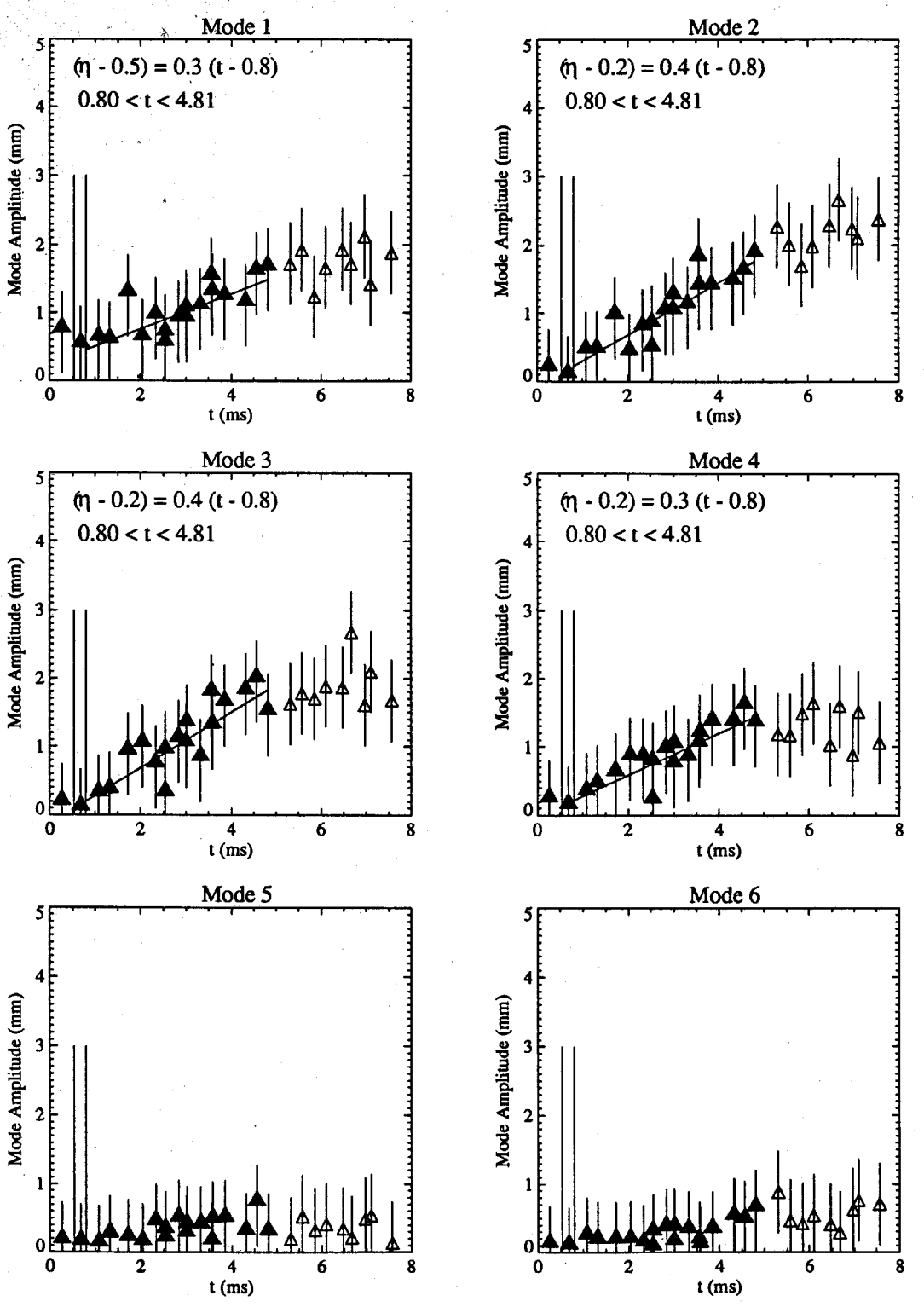

Fig.6.2.30 $M_i = 1.32$; $\tau = 1.2$ s Close End Wall Configuration. Amplitude of the First Six Modes *vs.* Time.

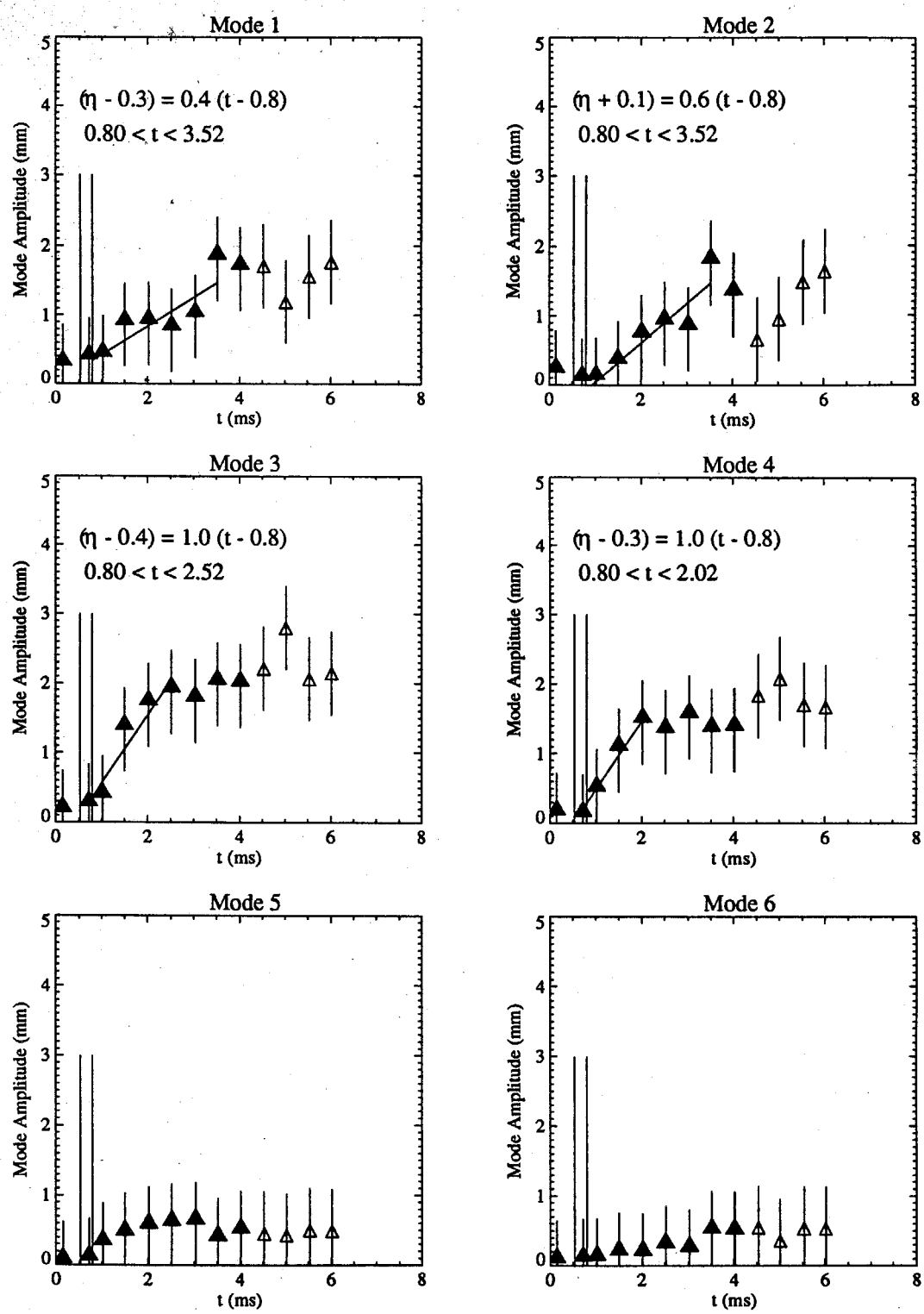

Fig.6.2.31 $M_i = 1.52$; $\tau = 1.2$ s Close End Wall Configuration. Amplitude of the First Six Modes *vs.* Time.

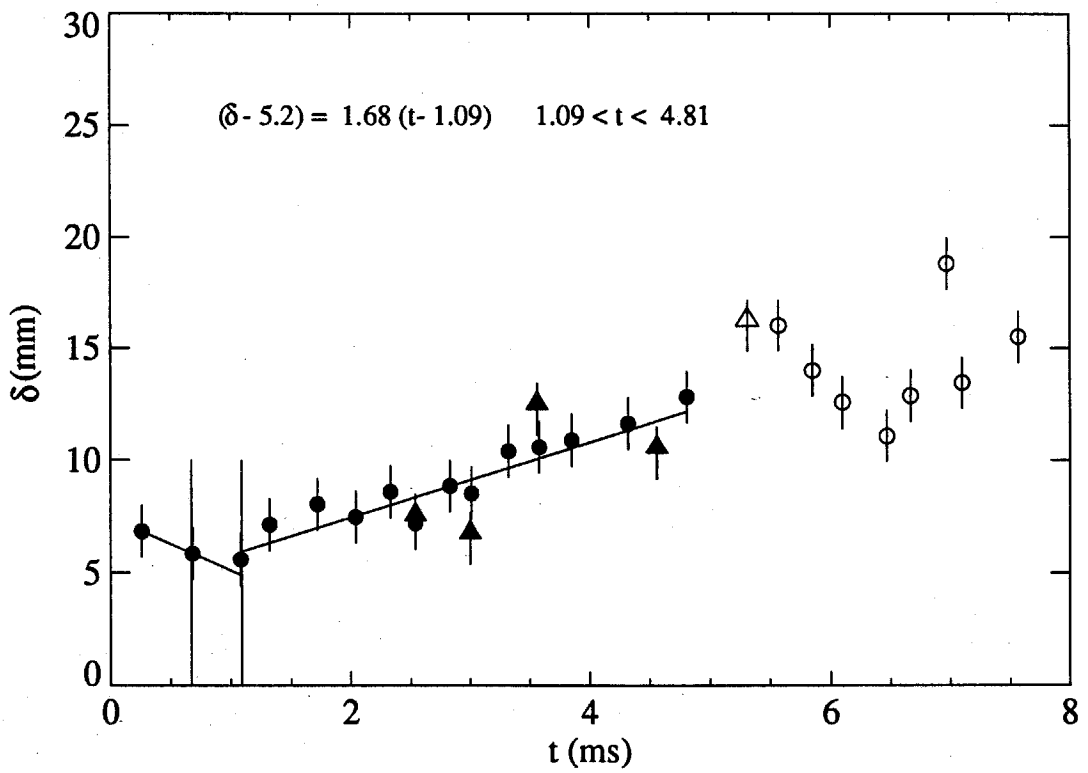

Fig.6.2.32 $M_i = 1.32$; $\tau = 1.2$ s. Close End Wall Configuration. Interface Thickness *vs.* time.

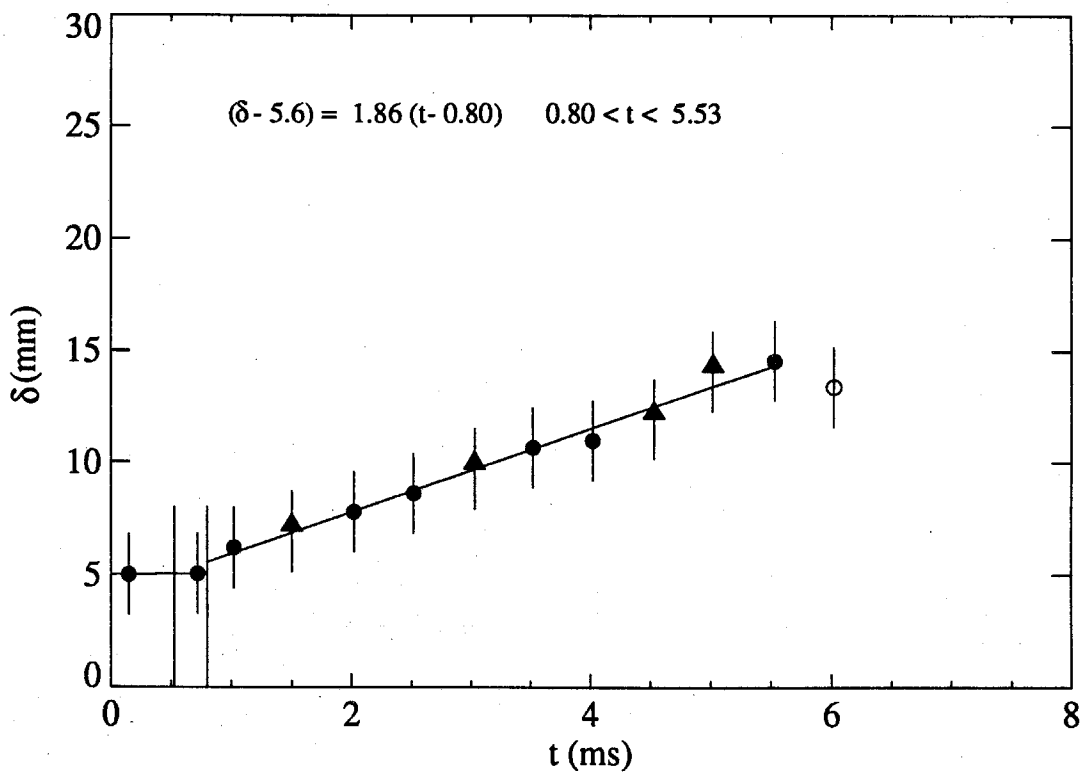

Fig.6.2.33 $M_i = 1.52$; $\tau = 1.2$ s. Close End Wall Configuration. Interface Thickness *vs.* time.

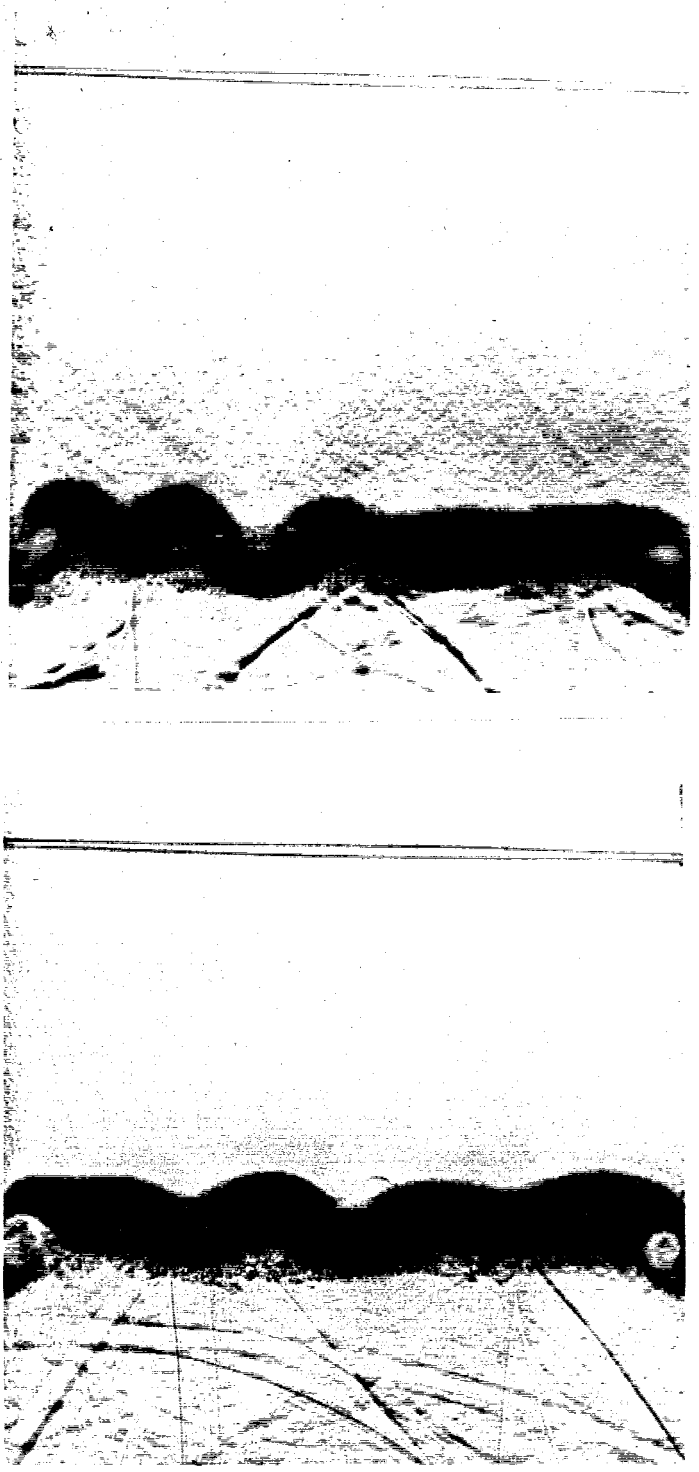

Fig.6.2.34 (a): Air/SF_6. CEW. $\tau = 1.2$ s; $M_i = 1.32$; $t = 1.62$ ms. (b): Air/Xenon. CEW. $\tau = 1.2$ s; $M_i = 1.32$; $t = 1.62$ ms. Schlieren Photographs.

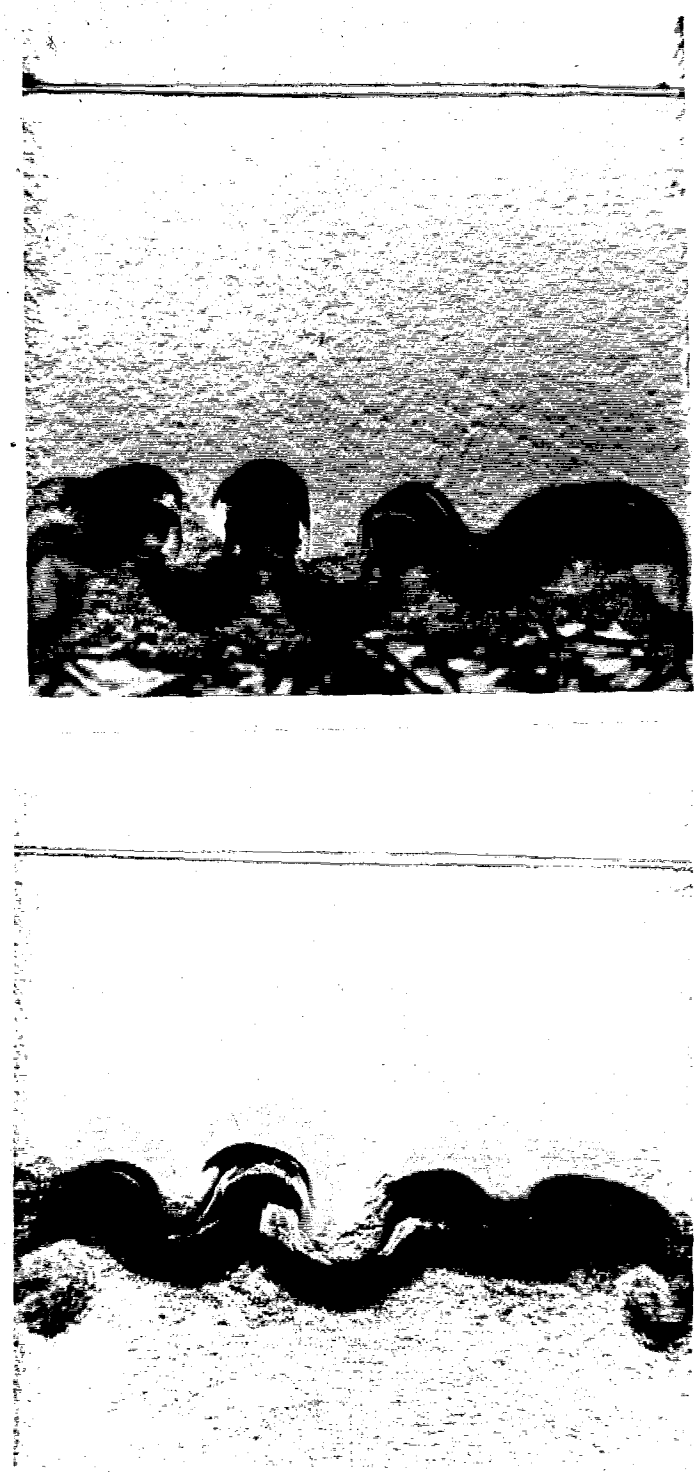

Fig.6.2.35 (a): Air/SF_6. CEW. $\tau = 1.2$ s; $M_i = 1.32$; $t = 2.11$ ms. (b): Air/Xenon. CEW. $\tau = 1.2$ s; $M_i = 1.32$; $t = 3.70$ ms. Schlieren Photographs.

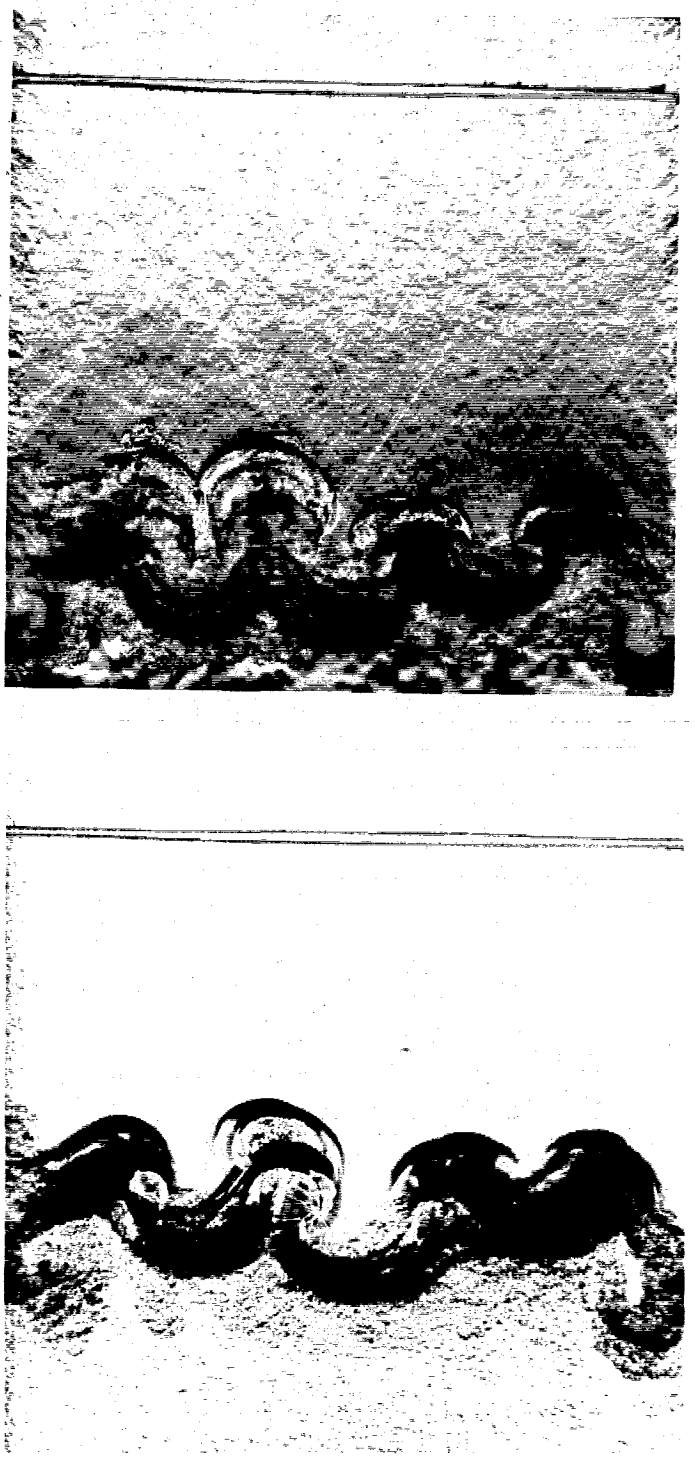

Fig.6.2.36 (a): Air/SF_6. CEW. $\tau = 1.2$ s; $M_i = 1.32$; $t = 3.12$ ms. (b): Air/Xenon. CEW. $\tau = 1.2$ s; $M_i = 1.32$; $t = 5.19$ ms. Schlieren Photographs.

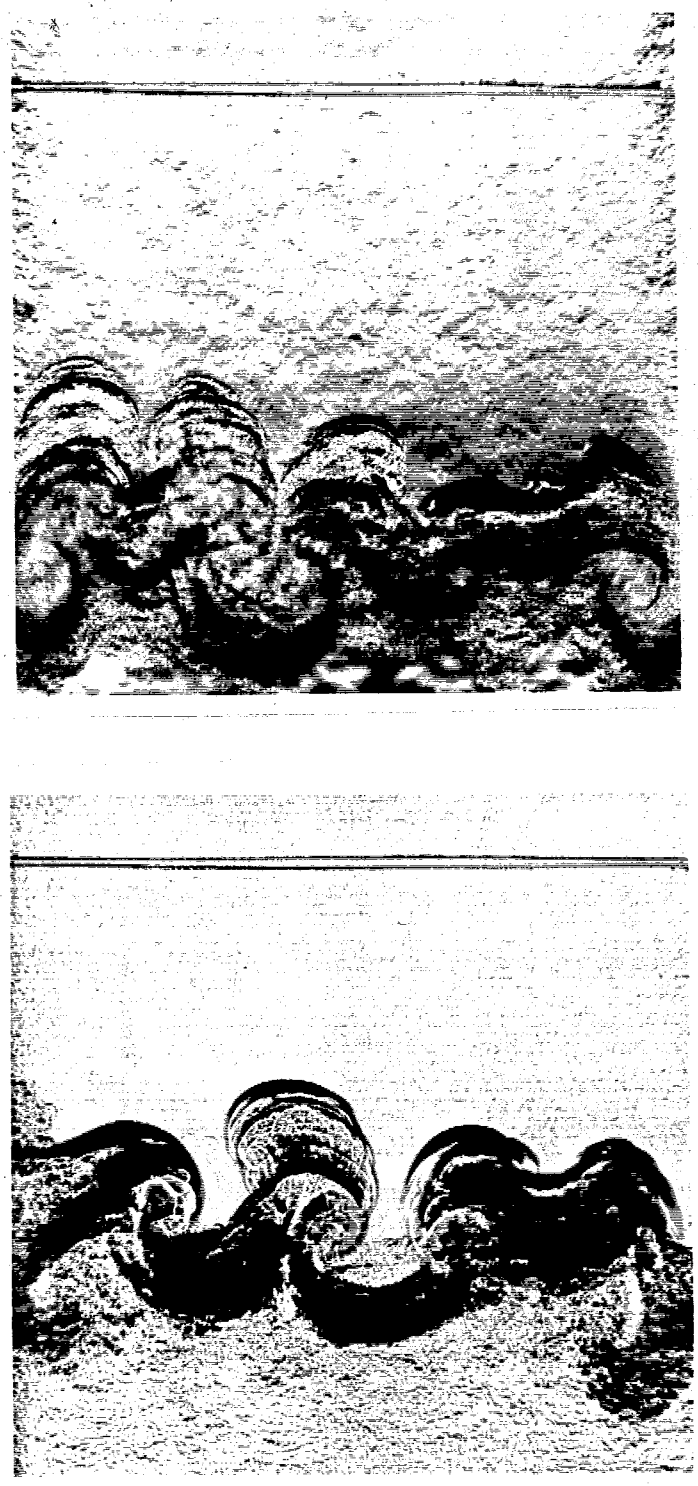

Fig.6.2.37 (a): Air/SF_6. CEW. $\tau = 1.2$ s; $M_i = 1.32$; $t = 4.68$ ms. (b): Air/Xenon. CEW. $\tau = 1.2$ s; $M_i = 1.32$; $t = 7.21$ ms. Schlieren Photographs.

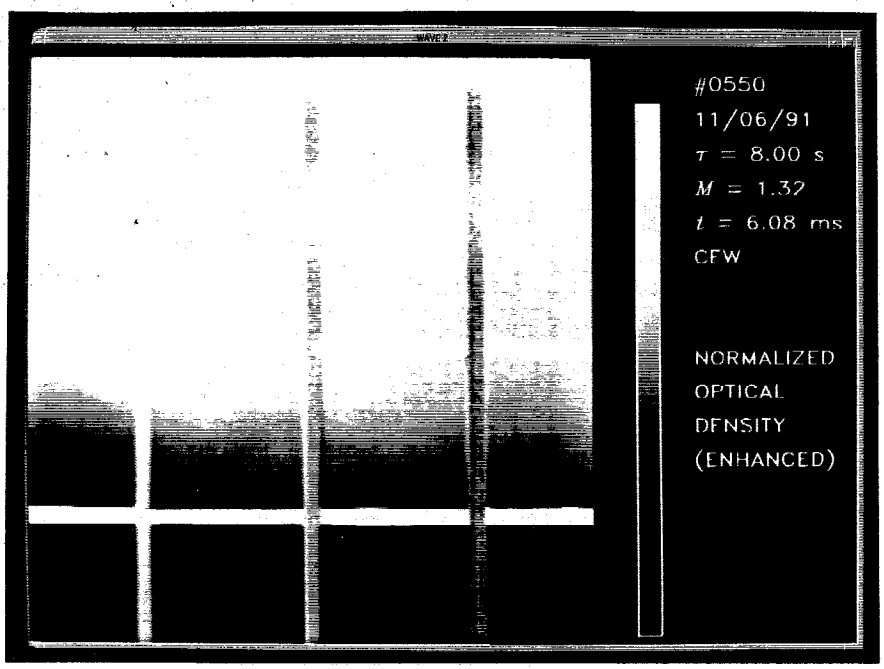

Fig.6.3.1 Air/Xenon. Run #0550. CEW. $\tau = 8.0$ s; $M_i = 1.32$; $t = 6.08$ ms. Optical Density of the Radiograph.

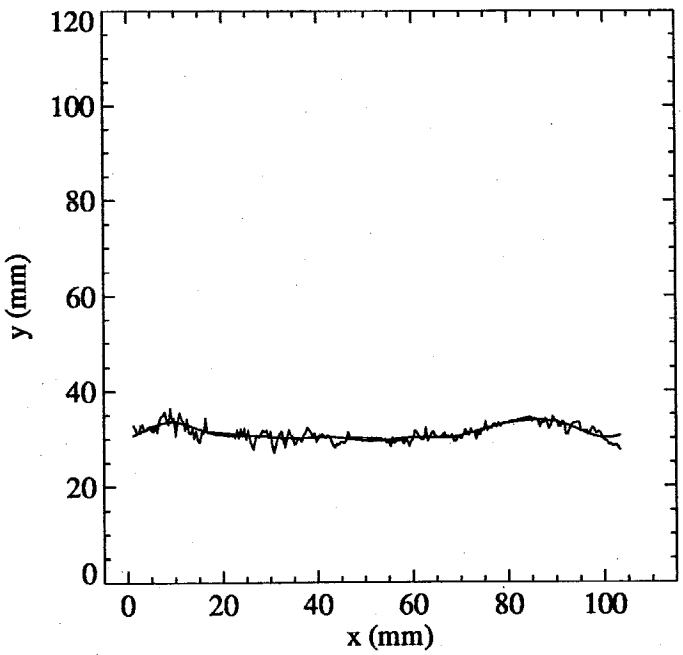

Fig.6.3.2 Run #0550. CEW. $\tau = 8.0$ s; $M_i = 1.32$; $t = 6.08$ ms. Mean Interface Shape.

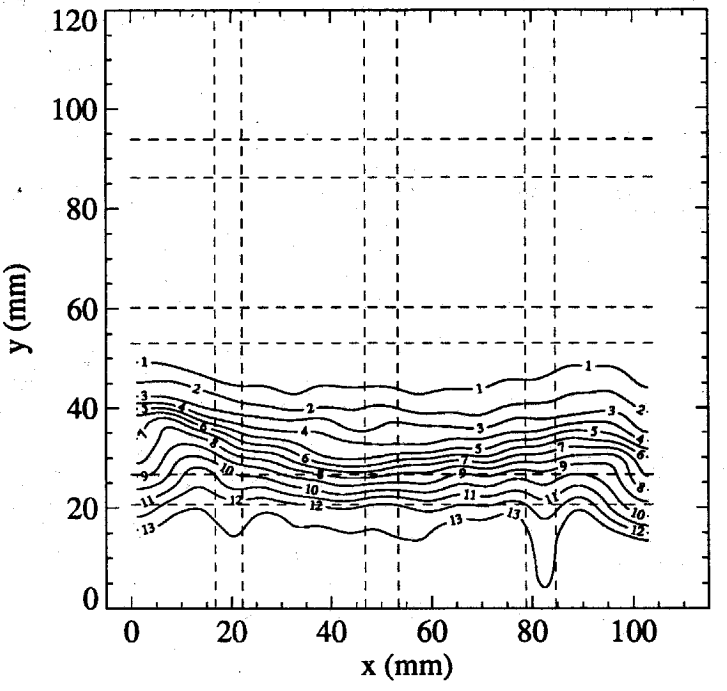

Fig.6.3.3 Run #0550. CEW. τ = 8.0 s; M_i = 1.32; t = 6.08 ms. Density Contours.

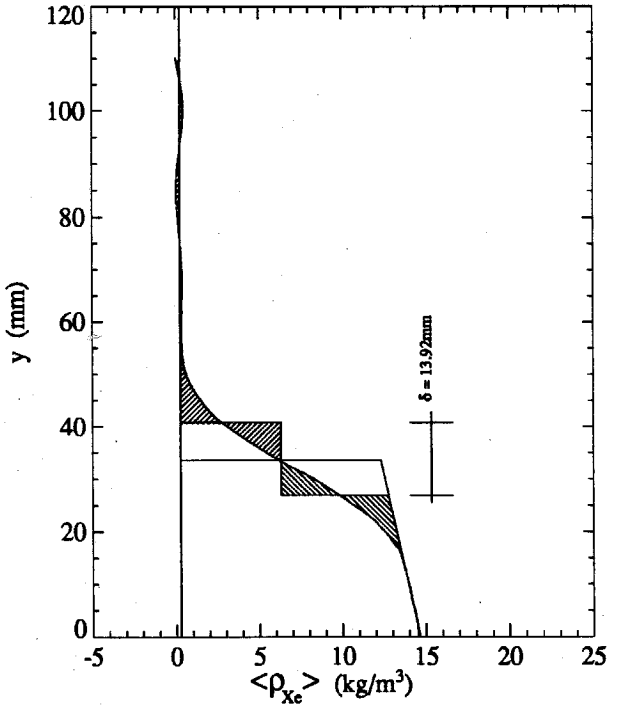

Fig.6.3.4 Run #0550. CEW. τ = 8.0 s; M_i = 1.32; t = 6.08 ms. Average Density Profile. $x_l = 0$, $x_r = 105$.

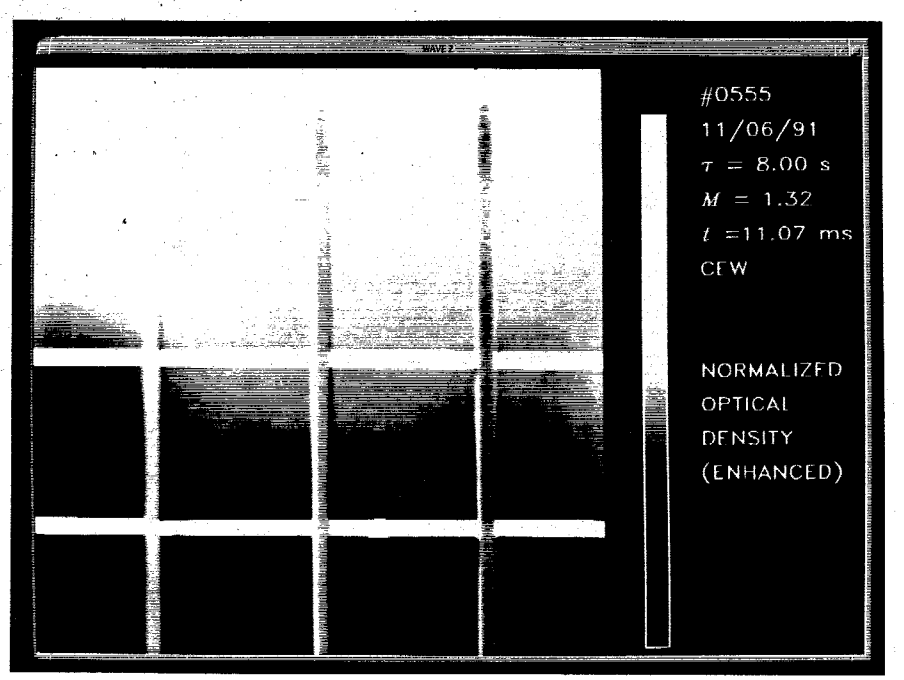

Fig.6.3.5 Air/Xenon. Run #0555. CEW. $\tau = 8.0$ s; $M_i = 1.32$; $t = 11.07$ ms. Optical Density of the Radiograph.

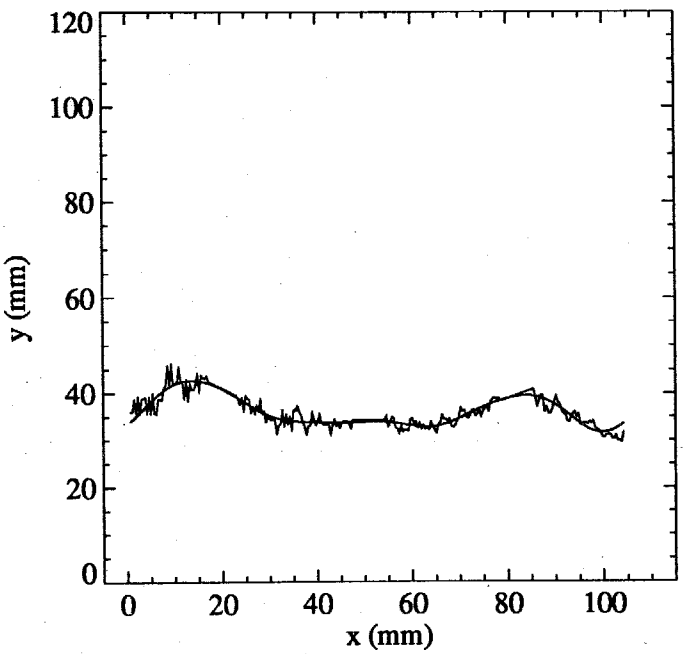

Fig.6.3.6 Run #0555. CEW. $\tau = 8.0$ s; $M_i = 1.32$; $t = 11.07$ ms. Mean Interface Shape.

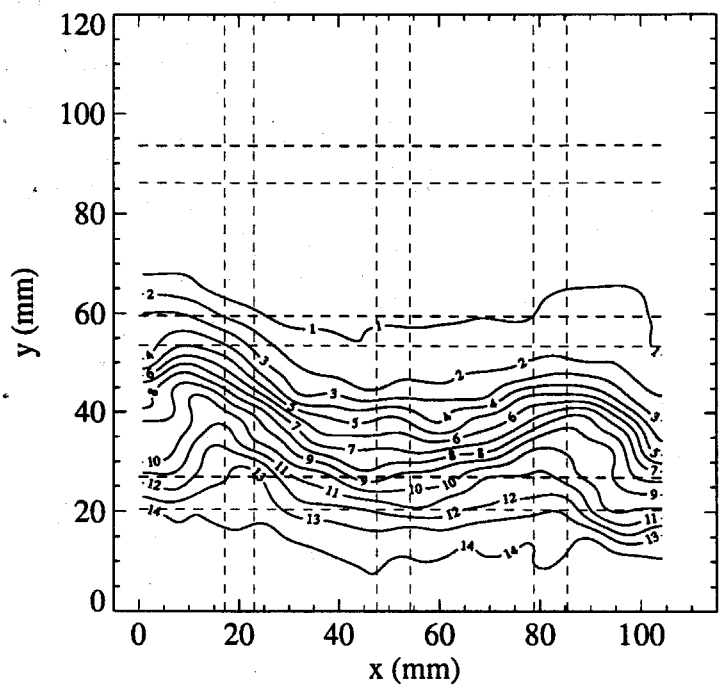

Fig.6.3.7 Run #0555. CEW. τ = 8.0 s; M_i = 1.32; t = 11.07 ms. Density Contours.

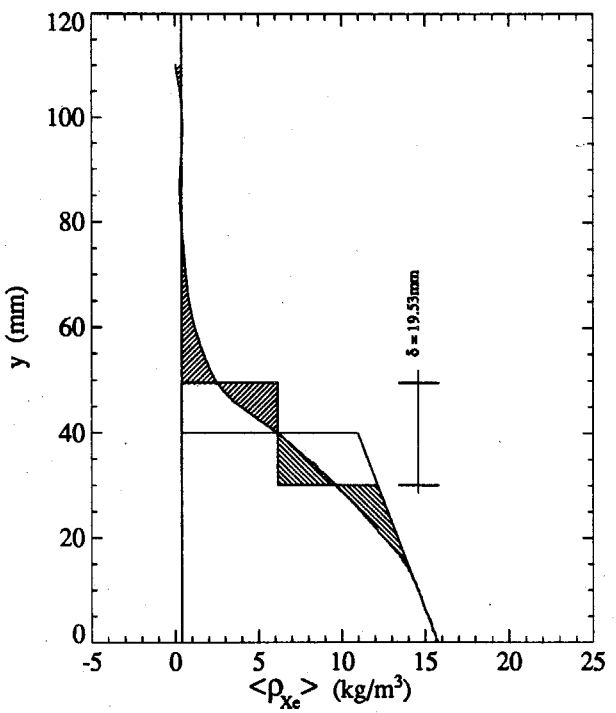

Fig.6.3.8 Run #0555. CEW. τ = 8.0 s; M_i = 1.32; t = 11.07 ms. Average Density Profile. x_l = 0, x_r = 105.

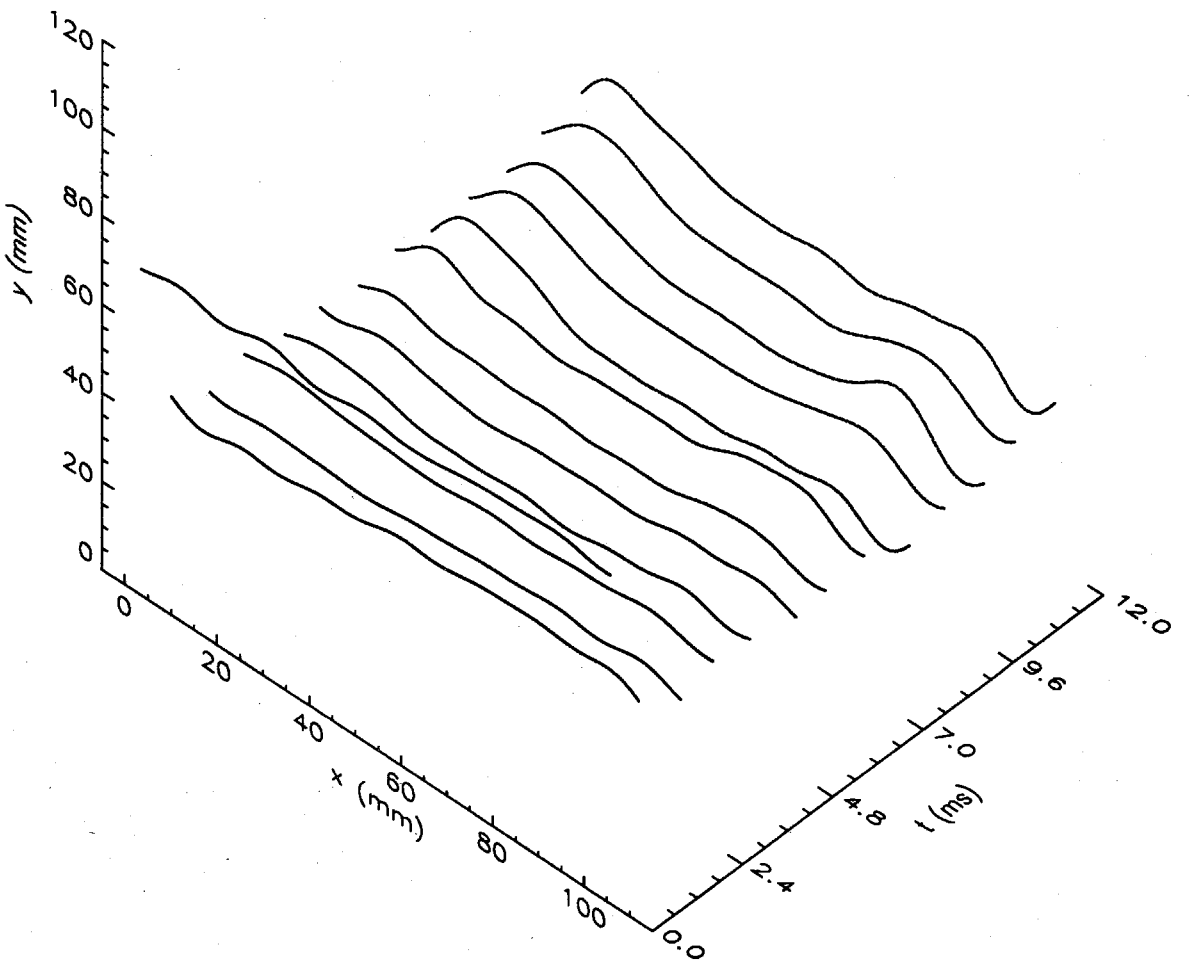

Fig.6.3.9 $M_i = 1.32$; $\tau = 8.0$ s Close End Wall Configuration. Mean Interface Shape at Various Times.

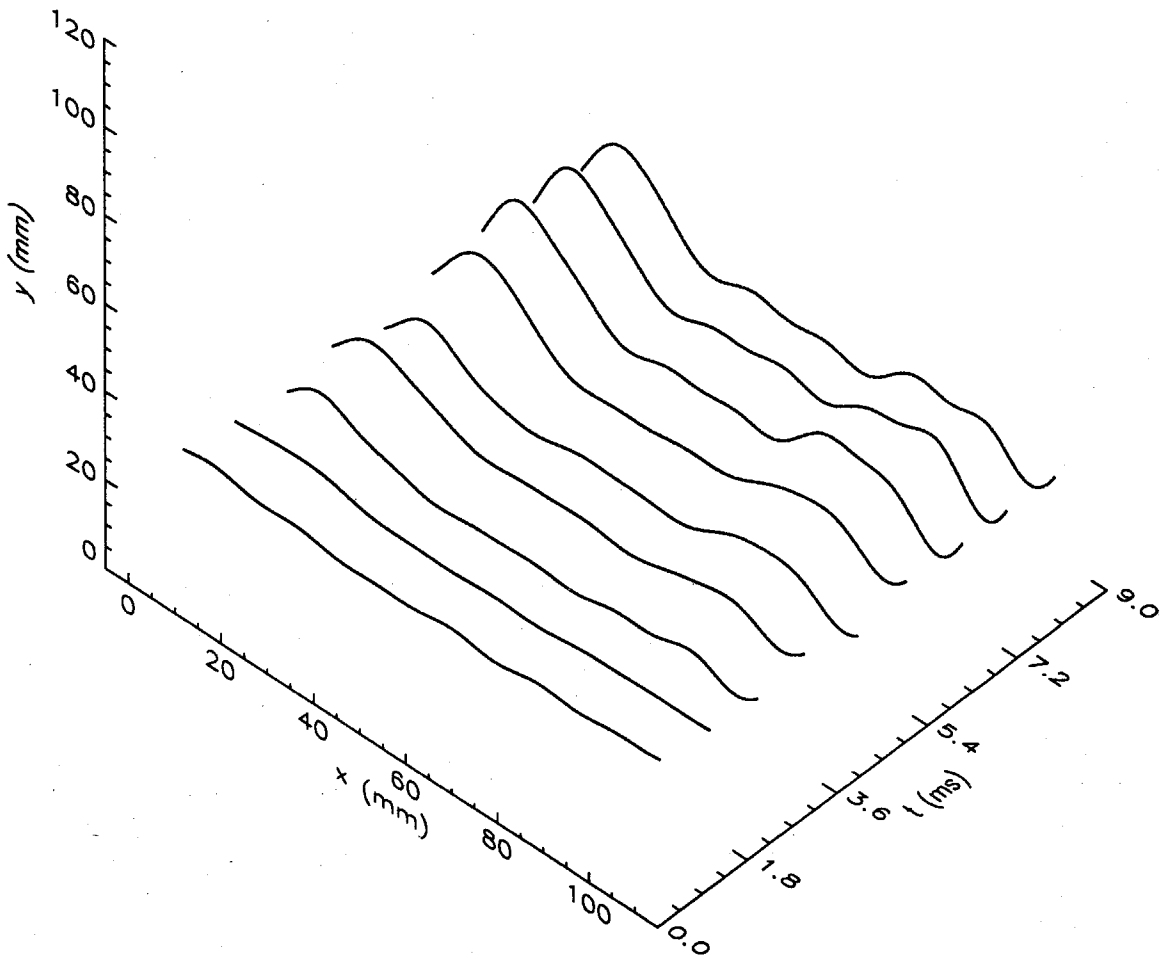

Fig.6.3.10 $M_i = 1.52$; $\tau = 8.0$ s Close End Wall Configuration. Mean Interface Shape at Various Times.

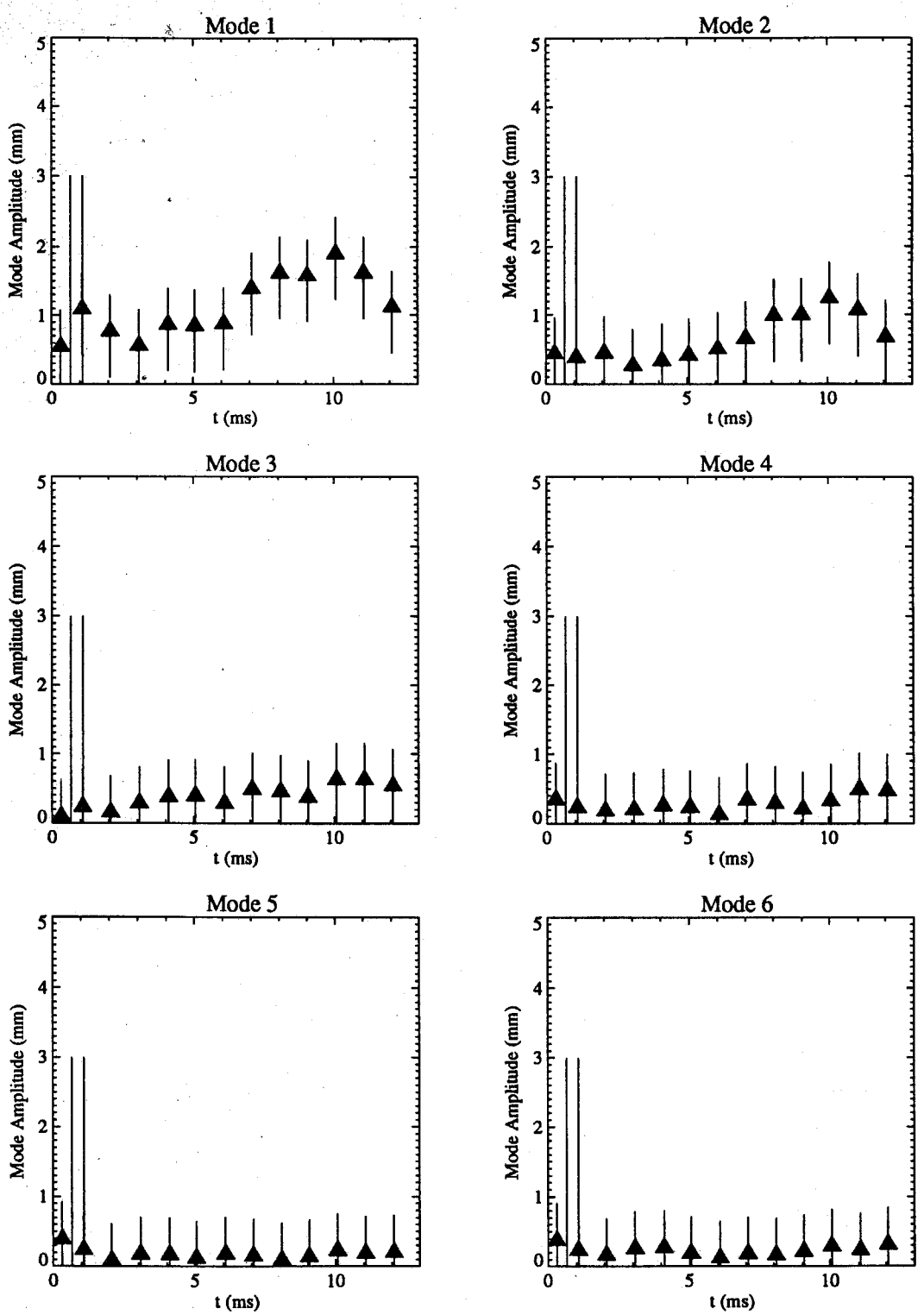

Fig.6.3.11 $M_i = 1.32$; $\tau = 8.0$ s Close End Wall Configuration. Amplitude of the First Six Modes *vs.* Time.

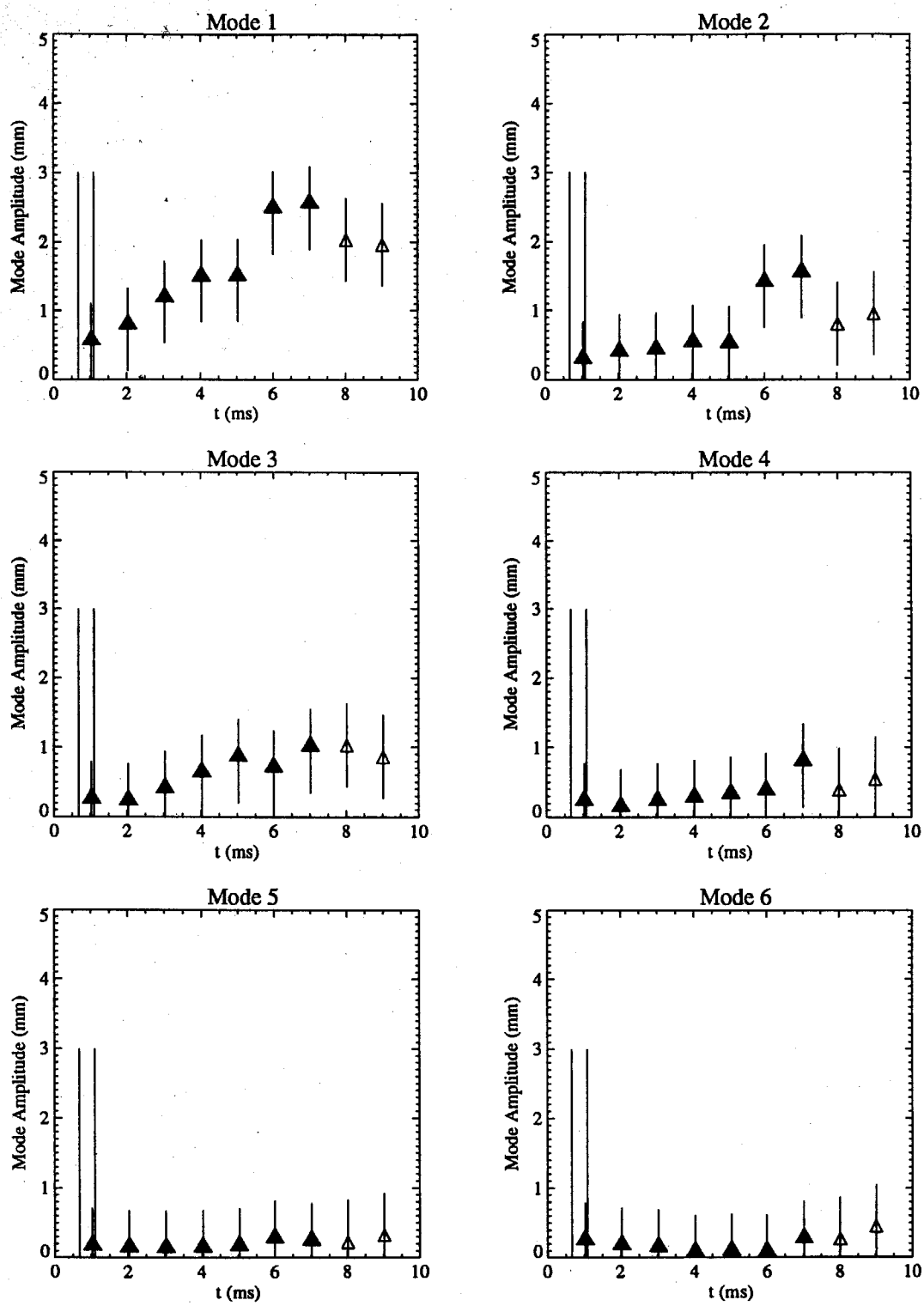

Fig.6.3.12 $M_i = 1.52$; $\tau = 8.0$ s Close End Wall Configuration. Amplitude of the First Six Modes *vs.* Time.

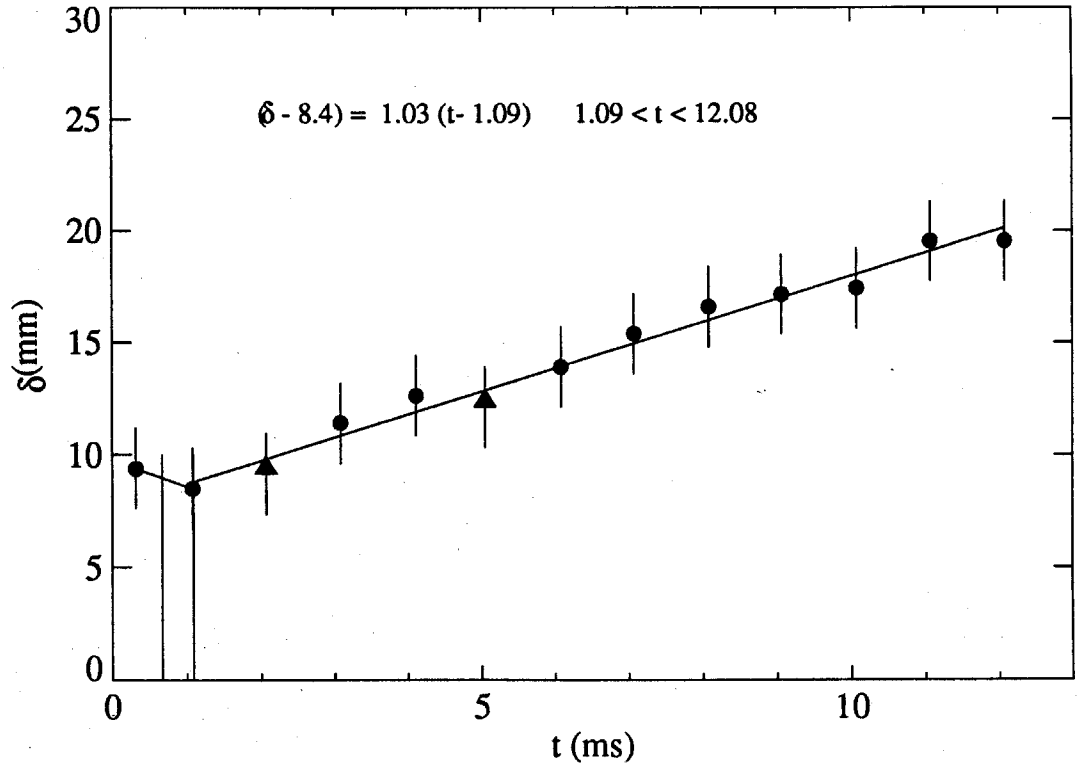

Fig.6.3.13 $M_i = 1.32$; $\tau = 8.0$ s. Close End Wall Configuration. Interface Thickness *vs.* time.

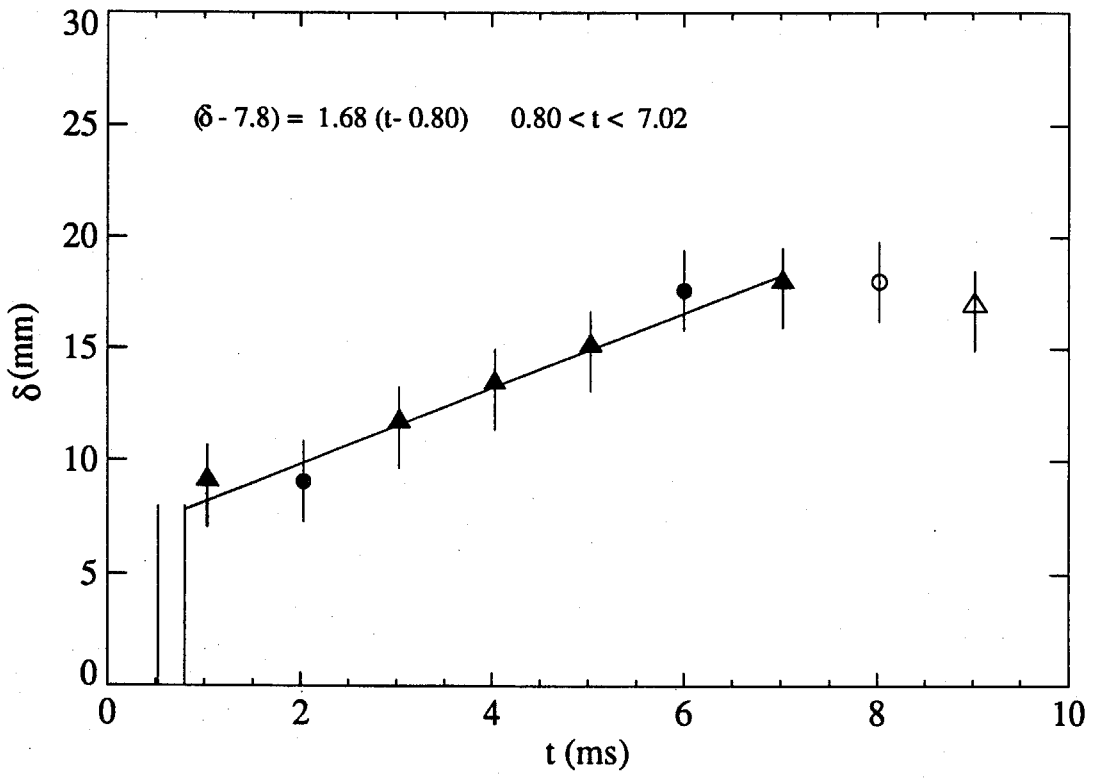

Fig.6.3.14 $M_i = 1.52$; $\tau = 8.0$ s. Close End Wall Configuration. Interface Thickness *vs.* time.

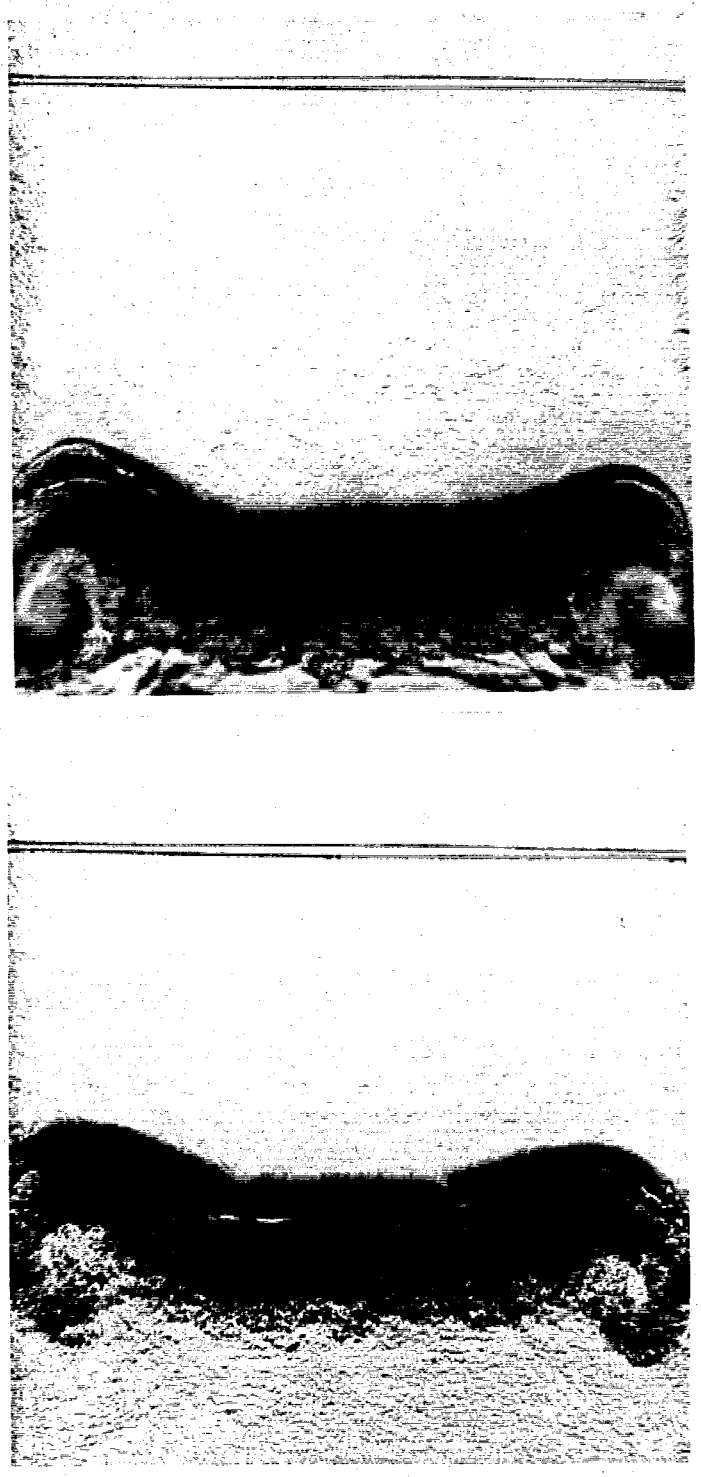

Fig.6.3.15 (a): Air/SF_6. CEW. τ = 8.0 s; M_i = 1.32; t = 3.14 ms. (b): Air/Xenon. CEW. τ = 8.0 s; M_i = 1.32; t = 6.20 ms. Schlieren Photographs.

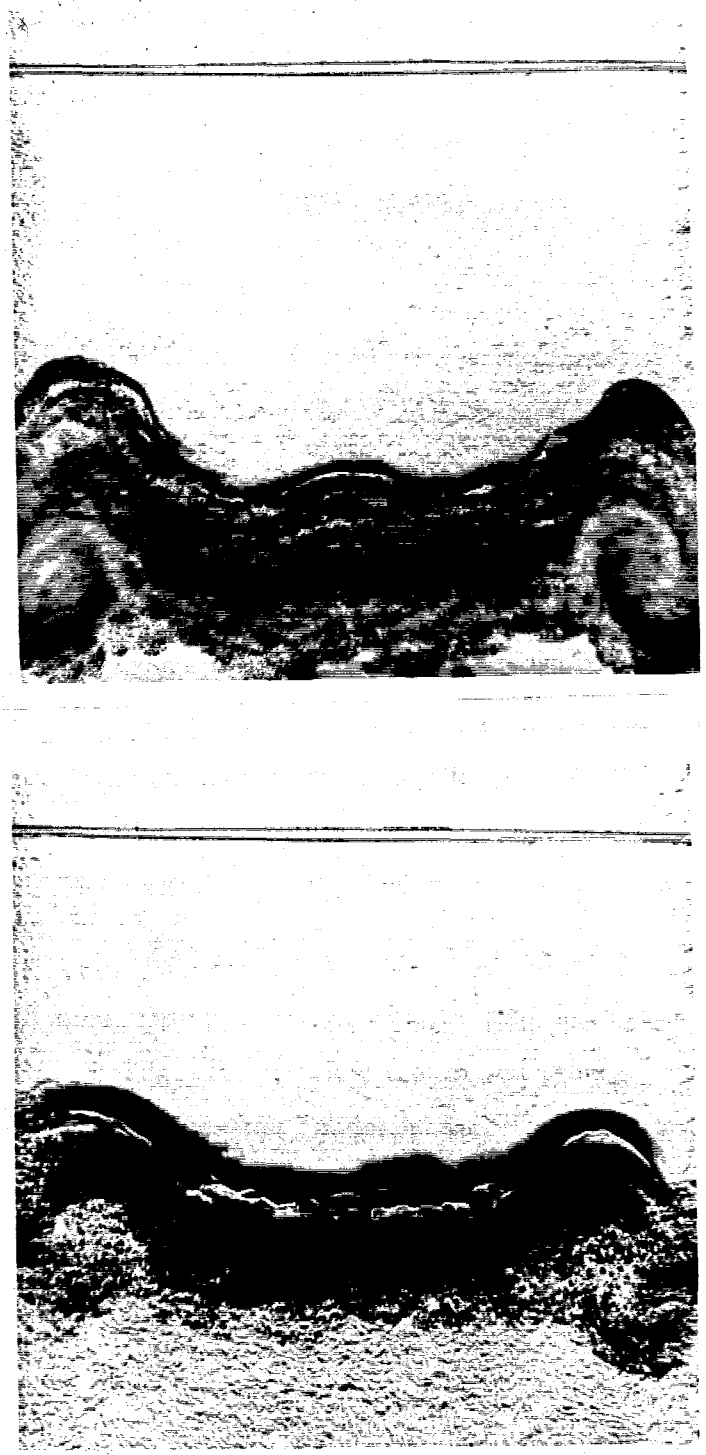

Fig.6.3.16 (a): Air/SF_6. CEW. τ = 8.0 s; M_i = 1.32; t = 4.19 ms. (b): Air/Xenon. CEW. τ = 8.0 s; M_i = 1.32; t = 9.34 ms. Schlieren Photographs.

CHAPTER 7

CONCLUSIONS

X-ray imaging has been successfully applied to the visualization of gas flow in a shock tube. A new densitometry technique, based on a specially developed calibration procedure, has been demonstrated, and applied to the study of shock-accelerated, unstable gas interfaces. All the interfaces observed in the present work were initially continuous, with finite density gradient across them; they were prepared by the use of a special plate retraction mechanism which had been specially designed and fabricated for this purpose, in the course of a previous investigation: This has allowed for two types of interface, single scale and multiscale, to be observed. The gases at the interface were always air and xenon, chosen for its unique X-ray absorption properties. Two different arrangements of the initial position of the interface were adopted to monitor the interface at long time delays after interaction with only one or two waves, or at short delays after several wave reverberations. Shock waves of two different Mach numbers were used in this latter configuration.

Information about the interface was deduced from the density data by means of integral definitions, yielding mean interface shapes and interface thicknesses; the interface shapes were decomposed into their Fourier modes, this being the first such treatment of experimental data for gaseous interfaces.

For the quasi sinusoidal interfaces, essentially no amplitude growth was observed after interaction with the incident wave (except for Mode 1). The modal amplitude growth rates measured upon interaction with the reflected shock were larger than those predicted by the theory, but the presence of the wall vortices made only one post-shock data point reliable to deduce the growth rates. These might therefore be largely overestimated. Most of the modal growth rates measured in the multiple shock configuration were smaller than theoretically predicted. Other than for the larger effect of the wall vortices, the fact that the amplitudes grow slower after a series of reverberations than after only two interactions remains unexplained. The measured growth rates were smaller than those found in the past

by schlieren visualization. This was due to the different details in the images generated with the two techniques and to the different procedures used to measure the amplitudes.

Measurements of the thickness of a single scale interface were a new contribution, as were the definition adopted for it and its implementation. The interface thickness showed virtually no growth after interaction with the incident shock, indicating that molecular diffusion makes the interface very smooth at the time of its preparation, and that the thickness growth after the reshock is mostly due to the random acoustic disturbances generated by the interaction of the reshock with the boundary layer. In the far end wall configuration, the measurements of the thickness growth rates of multiscale interfaces were larger than previously reported (but the presence of the wall vortices actually caused both the thickness values and the growth rate to be overestimated). The measurements in the multiple reverberation case yielded smaller growth rates than previously reported. The growth rate measured in the close end wall configurations was 4 times smaller than that measured in the far end wall configuration. In this case the effect of the wall vortices was smaller than in the far end wall case, and the X-ray densitometry technique produced, as expected, smaller thickness values than schlieren imaging had in the past. In both the far and close end wall configurations, and for both accelerating Mach numbers, the thickness growth rate of single scale interfaces was larger than that of the multiscale interfaces.

The formation and the growth of wall effects has been observed, to a larger extent than in previous experiments; a first correction of the data to take the wall effects into account has been proposed. But it is evident that further work is needed with different experimental techniques to eliminate the adverse effects of the wall vortices, or at least to precisely quantify them.

REFERENCES

Abd-El-Fatah, A.M. & Henderson, L.F. 1978a Shock Waves at a Fast-Slow Gas Interface, *JFM* **86**, 15.

Abd-El-Fatah, A.M. & Henderson, L.F. 1978b Shock Waves at a Slow-Fast Gas Interface, *JFM* **89**, 79.

Aleshin, A.N., Gamalii, E.G., Lazareva, E.V., Lebo, I.G., & Rozanov, V.B. 1988 Nonlinear and Transitional Stages in the onset of the Richtmyer-Meshkov Instability, *Sov. Tech. Phys. Lett.* **14**, 466.

Andronov, V.A., Bakhrakh S.M., Meshkov, E.E., Mokhov, V.N., Nikiforov, V.V., Pevnitskii, A.V. & Tolshmyakov, A.I. 1976 Turbulent Mixing at Contact Surface Accelerated by Shock Waves, *Sov. Phys. JETP* 44, 424.

Barenblatt, G.I. 1983 Self-Similar Turbulence Propagation from an Instantaneous Plane Source, In: *Non-Linear Dynamics and Turbulence*, edited by G.I. Barenblatt, G. Ioos and D.D. Joseph, Pitman, Boston, 48.

Belenkii, S.Z. & Fradkin, E.S. 1967 Theory of Turbulent Intermixing, Proceedings P.N. Lebedev Phys. Inst. **29**, 197.

Benjamin, R.F. & Fritz, J.N. 1987 Shock Loading a Rippled Interface Between Liquids of Different Densities, *Phys. Fluids* **30**, 331.

Brouillette, M. 1989 On The Interaction of Shock Waves With Contact Surfaces Between Gases of Different Densities, Ph.D. Thesis, California Institute of Technology

Brouillette ,M. & Sturtevant, B. 1989 Growth Induced by Multiple Shock Waves Normally Incident on Plane Gaseous Interfaces, *Physica D* **37**, 247

Catherasoo, C.J. & Sturtevant, B. 1983 Shock Dynamics in Non-Uniform Media, *JFM* **127**, 539

Canuto, V.M., Goldman, I., & Chasnov, J. 1987 A Model For Fully Developed Turbulence, *Phis. Fluids* **30**, 3391.

Chandrasekhar, S. 1961 *Hydrodynamic and Hydromagnetic Stability*, Oxford University Press, Oxford, 433.

Duff, R.E., Harlow, F.H. & Hirt, C.W. 1962 Effects of Diffusion on Interface Instability Betwen Gases, *Phys. Fluids* **5**, 417.

Gamalii, E.G., Zaitsev, S.G., Lebo, I.G., Rozanov, V.B., Titov, S.N., Cheborateva, E.I. 1989 Interaction of a Shock Wave with the Contact Region of Gases of Different Density, *High Temperature* **26**, 751.

Haan, S.W. 1989 Onset of Nonlinear Saturation for Rayleigh-Taylor Growth in the Presence of a Full Spectrum of Modes, *Phys. Rev. A* **39**, 5812.

Haan, S.W. 1991 Weakly Nonlinear Hydrodynamic Instabilities in Inertial Fusion, *Phys. Fluids B* **3**, 2349

Jacobs, J.B. & Catton, I. Three Dimensional Rayleigh-Taylor Instability Part 1. Weakly Nonlinear Theory, *JFM 187*, 329.

Kaye, G.W.C., & Laby, T.H. 1971 *Tables of Physical Properties & Chemical Constants*, Longman, London, 88.

Landau, L.D. & Lifshitz, E.M. 1959 *Fluid Mechanics*, Pergamon Press, New York, 477.

Lelevier, R., Lasher, G.J., & Bjorklund, F. 1955 Effect of a Density Gradient on Taylor Instability, Report UCRL-4459, University of California Radiation Laboratory.

Leith, C.E. 1985 Acceleration-Induced Turbulent Mixing: Model One, Unpublished Report, Lawrence Livermore National Laboratory.

Lewis, D.J. 1950 The Instability of Liquid Surfaces when Accelerated in a Direction Perpendicular to their Planes. II, *Proc. Roy. Soc. A* **202**, 81.

Lord Rayleigh 1900 Investigation of the Character of the Equilibrium of an Incompressible Heavy Fluid of Variable Density, In: *Scientific Papers*, Vol. 2, Dover, New York, 200.

Markstein, G.H. 1957 Flow Disturbances Induced Near a Slightly Wavy Contact Surface, or Flame Front, Traversed by a Shock Wave, *J. Aero. Sciences* **24**, 238.

Meshkov, E.E. 1969 Instability of the Interface of Two Gases Accelerated by a Shock-Wave, *Sov. Fluid Dynamics* **4**, 101.

Mikaelian, K.O. 1982 Rayleigh-Taylor Instabilities in Stratified Fluids, *Phys. Rev. A* **26**, 2140.

Mikaelian, K.O. 1985 Richtmyer-Meshkov Instabilities in Stratified Fluids, *Phys. Rev. A* **31**, 410

Mikaelian, K.O. 1986 Approximate Treatment of density Gradients in Rayleigh-Taylor Instabilities *Phys. Rev. A* **33**, 1216.

Mikaelian, K.O. 1988 Simulation of the Richtmyer-Meshkov Instability and Turbulent Mixing in Shock-Tube Experiments, Unpublished Report, UCID-21328, Lawrence Livermore National Laboratory. Mikaelian, K.O. 1989a Explicit Growth Rates for the Rayleigh-Taylor Instability in Exponential Density Profiles, *Phys. Rev. A* **40**, 4801.

Mikaelian, K.O. 1989b Turbulent Mixing Generated by Rayleigh-Taylor and Richtmyer-Meshkov Instabilities, *Physica D* **36**, 343.

Mikaelian, K.O. 1990a Turbulent Energy at Accelerating and Shocked Interfaces, *Phys. Fluids A* **2**, 592.

Mikaelian, K.O. 1990b Rayleigh-Taylor and Richtmyer Meshkov Instabilities in Multilayer Fluids with Surface Tension, *Phys. Rev. A* **42**, 7211.

Mikaelian, K.O. 1991a Kinetic Energy of Rayleigh-Taylor and Richtmyer-Meshkov Instabilities, *Phys. Fluids A* **3**, 2625

Mikaelian, K.O. 1991b Density Gradient Stabilization of the Richtmyer-Meshkov Instability, *Phys. Fluids A* **3**, 2638

Mirels, H. 1955 Laminar Boundary Layer Behind Shock Advancing into Stationary Fluid, NACA TN-3401.

Mirels, H. 1964 Shock Tube Test Time Limitation Due to Turbulent-Wall Boundary Layer, *AIAA. J.* **2**, 84.

Pham, T. Numerical Studies of Incompressible Richtmyer-Meshkov Instability in a Stratified Fluid, Ph.D. Thesis, California Institute of Technology

Read, K.I. 1984 Experimental Investigation of Turbulent Mixing by Rayleigh-Taylor Instability, *Phisica D* **12**, 45.

Read, K.I. & Youngs, D.L. 1983 Experimental Investigation of Turbulent Mixing by Rayleigh-Taylor Instability, AWRE Report 0-11/83.

Remington B.A., Haan S.W., Gleddining S.G., Kilkenny J.D., Munro D.H. & Wallace R.J. 1991, *Phys. Rev. Lett.* **67**, 3259.

Richtmyer, R.D. 1960 Taylor Instability in Shock Acceleration of Compressible Fluids, *Comm. Pure Appl. Math.* **8**, 297.

Roshko, A. & Baganoff, D. 1961 A Novel Device for Bursting Shock-Tube Diaphragms, *Phys. Fluids* **4**, 1445.

Saffman, P.G. & Meiron, D.I. 1989 Kinetic Energy Generated by the Incompressible Richtmyer-Meshkov Instability in a Continuously Stratified Fluid, *Phys. Fluids A* **1**, 1767.

Schwendeman, D.W. 1988 Numerical Shock Propagation in Non-Uniform Media, *JFM* **188**, 383.

Smith, J.A., Coles, D., Roshko, A. & Prasad, A.J. 1967 A Description of the GALCIT 6" Shock Tube, GALCIT Report FM-67-1.

Sturtevant, B. 1988 Rayleigh-Taylor Instability in Compressible Fluids, In: *Shock Tubes and Waves*, edited by H. Grönig, VCH, Wendheim, Federal Republic of Germany, 89.

Takabe, H., Yamanaka, M., Mima, K., Yamanaka, C., Azechi, H., Miyanaga,N., Nakatsuka, M., Jitsuno, T., Norimatsu, T., Takagi, M., Nishimura, H., Nakai, M., Yabe, T., Sasaki, T., Yoshida, K., Nishihara, K., Kato, Y., Izawa, Y., Yamanaka, T., & Nakai, S. 1988 *Phys. Fluids* **31**, 2884.

Taylor, G.I. 1950 The Instability of Liquid Surfaces when Accelerated in a Direction Perpendicular to their Planes. I, *Proc. Roy. Soc. A* **201**, 192.

Youngs, D.L. 1984 Numerical Simulation of Turbulent Mixing by Rayleigh-Taylor Instability, *Physica D* **12**, 32.

Youngs, D.L. 1989 Modeling Turbulent Mixing by Rayleigh-Taylor Instability, *Physica D* **37**, 270.

Zaitsev, S.G., Lazareva, E.V., Chernukha, V.V. & Belayev, V.M. 1985 Experimental Investigation of the Hydrodynamic Instability of an Interface Between Media of Different Density in an Acceleration Field, *High Temperature* **23**, 435.